ESTIMATION OF TIME DEPENDENT PROPERTIES FROM SURFACE PRESSURE IN OPEN CAVITIES

FINAL REPORT
AFOSR GRANT FA9550-06-1-0278

By

Lawrence Ukeiley, Louis Cattafesta, Terry Song and George Shumway

Department of Mechanical and Aerospace Engineering
University of Florida

AFRL-SR-AR-TR-09-0156

REPORT DOCUMENTATION PAGE

PLEASE DO NOT RETURN YOUR FORM TO THE ABOVE ORGANIZATION.

1. REPORT DATE *(DD-MM-YYYY)*	2. REPORT TYPE	3. DATES COVERED *(From - To)*
28-02-2008	FINAL	01-04-2006 to 30-11-2008

4. TITLE AND SUBTITLE
ESTIMATION OF TIME DEPENDENT PROPERTIES FROM SURFACE PRESSURE IN OPEN CAVITIES

5a. CONTRACT NUMBER
FA9550-06-1-0278

5b. GRANT NUMBER

5c. PROGRAM ELEMENT NUMBER

6. AUTHOR(S)
Lawrence Ukeiley, Louis Cattafesta, Terry Song and George Shumway

5d. PROJECT NUMBER

5e. TASK NUMBER

5f. WORK UNIT NUMBER

7. PERFORMING ORGANIZATION NAME(S) AND ADDRESS(ES)
University of Florida
Office of Engineering Research
339 Weil Hall /PO BOX 116550
Gainesville, FL 32611-6550

8. PERFORMING ORGANIZATION REPORT NUMBER

9. SPONSORING/MONITORING AGENCY NAME(S) AND ADDRESS(ES)
Air Force Office of Scientific Research
875 North Randolph Street, Suite 326
Arlington VA 22203-1768
Dr John Schmisseur/NA

10. SPONSOR/MONITOR'S ACRONYM(S)
AFOSR

11. SPONSOR/MONITOR'S REPORT NUMBER(S)

12. DISTRIBUTION/AVAILABILITY STATEMENT
Distribution A: Approved for Public Release

13. SUPPLEMENTARY NOTES

14. ABSTRACT

The intense fluctuating pressures observed in open cavities are extremely detrimental hence the ability to control the flow to minimize them is an important challenge. Many open loop methodologies have proven effective at this for single operating conditions however they often are detrimental at off design conditions. Closed loop flow control is applicable over a range of flow conditions and is the thrust of many current and past studies. However in order to advance its effectiveness there is a need for a better understanding of the flow physics and the effect that control has on it. This study represents a step in the direction of developing the tools that will allow for a better understanding of this flow physics along with an improvement adaptive control methodologies. One aspect presented in this study involves the application of an estimation methodology to obtain the time dependent flow properties in high speed applications and then calculate the relevant flow properties associated with generation of the pressure fluctuations. In conjunction with gaining insight into the flow physics we have also developed improved actuators and an adaptive flow control methodologies which demonstrate reductions in the broad band and tonal components of the fluctuating surface pressures.

15. SUBJECT TERMS
Cavity Flow, Flow Control

16. SECURITY CLASSIFICATION OF:			17. LIMITATION OF ABSTRACT	18. NUMBER OF PAGES	19a. NAME OF RESPONSIBLE PERSON
a. REPORT	b. ABSTRACT	c. THIS PAGE			19b. TELEPHONE NUMBER *(Include area code)*
			UU	89	

Abstract

The intense fluctuating pressures observed in open cavities are extremely detrimental hence the ability to control the flow to minimize them is an important challenge. Many open loop methodologies have proven effective at this for single operating conditions however they often are detrimental at off design conditions. Closed loop flow control is applicable over a range of flow conditions and is the thrust of many current and past studies. However in order to advance its effectiveness there is a need for a better understanding of the flow physics and the effect that control has on it. This study represents a step in the direction of developing the tools that will allow for a better understanding of this flow physics along with an improvement adaptive control methodologies. One aspect presented in this study involves the application of an estimation methodology to obtain the time dependent flow properties in high speed applications and then calculate the relevant flow properties associated with generation of the pressure fluctuations. In conjunction with gaining insight into the flow physics we have also developed improved actuators and an adaptive flow control methodologies which demonstrate reductions in the broad band and tonal components of the fluctuating surface pressures. In addition we present a study which was conducted using successful open loop control to demonstrate our ability to determine the effects of the control on the underlying flow physics.

1 Introduction

The primary goal of this research is to develop a better fundamental understanding of the sources generating the large surface pressure fluctuations in cavity flows so that more efficient physics based control can be used in the future. This first chapter introduces the flow physics of cavity flows by way of a brief discussion then we will discuss some of the previous applications of control to cavity flows. This is followed by a brief statement of the objectives of the study which is in turn followed by section discussing the layout of the rest of this document.

1.1 Motivation

From the limited review that will be presented below, it is apparent that while progress has been made towards effective active suppression concepts, we do not yet understand the key physical mechanisms that need to be leveraged in the design of an effective control system without iteration. The current effort is our initial effort to develop adaptive control concepts and the tools which will allow us to investigate their effects on the flow physics. Through this and follow on efforts we hope to provide a methodology that will us to develop better control methods along with having a better understanding of the flow physics effected by the control.

1.2 Background

In this section we will review the basic physics of flow over an open cavity along with a detailed review of many studies which have used flow control (open and closed loop) in an attempt to reduce fluctuating surface pressure. This review is important as it provides the back drop of what has been previously accomplished and set the stage for the work presented here and follow on efforts to understand the effects of control on the flow.

1.2.1 Cavity Flow Physics

Flow over an open cavity has important characteristics that are representative of those in many industrial configurations as well as exhibiting important fundamental phenomena. Under certain geometrical configurations the flow is known to be dominated by a large amplitude self-sustained oscillations that originate from a complex aeroacoustic feedback process. This process is dominated by the growth and convection of instabilities in the shear layer at the cavities opening and how this shear layer interacts with the cavities rear wall. The oscillations of the shear layer and the impact of the free stream flow on the aft wall of the cavity serve as a source which fulfill the self-sustained oscillations and result in large pressure fluctuations throughout the cavity. These large pressure fluctuations are undesirable in most applications and the need for a better understanding of this process so that a means to alter it can be developed is still a topic of many ongoing studies even after over a half century of research on resonating cavity flows.

Flow over open cavities has been studied over the past several decades from several different perspectives. The original studies which slanted towards aircraft applications are generally attributed to Roshko (1955) and Krishnamutry (1955). The more than 50 years of studies of flows over open cavities which have followed have led to many advances in the understanding of the important flow features of cavity flows and the governing parameters which dictate its behavior. The early studies revealed an unsteady momentum flux into and out of the cavity, which results in a "breathing" or "pumping" action. This pumping action causes the stagnation streamline of the shear layer to fluctuate up and down the aft wall of the cavity, which has been widely thought to be responsible for sound production in the cavity. The study of Rossiter (1964) is regarded as one of the significant benchmark cavity flow studies and resulted in a semi-empirical relationship that, with slight modification, predicts the frequencies of the resonant modes in open cavities. Rockwell and Naudascher (1978) provided an excellent review of the work conducted on cavity flows through the late 1970's. One of the more comprehensive studies was that of

Heller and Bliss (1975), which was an analytical and experimental program that examined cavities exposed to both subsonic and supersonic free stream flows. In their study they postulated mechanisms of how the shear layer and free stream flow interact with the aft wall of the cavity and also evaluated several concepts for suppressing the discrete tones, such as slanting the aft wall. A water table was used to visualize the aforementioned interactions, and the authors claimed that the important mechanism is not necessarily the interaction of the shear layer with the aft wall but instead the free stream flow impinging on the aft wall when the shear layer enters the cavity. More recently, schlieren images of a cavity in transonic flow by

Heller and Delfs (1996) have largely substantiated the earlier proposed mechanisms. In addition, there have been many studies that have concentrated on collecting databases for characterizing parametric effects, such as Tracy and Plentovich (1997) and Dix and Bauer (2000). From a review of the previously mentioned studies and many others, too numerous to list here, one can make several observations. The first is that the features of cavity flow are largely determined by the coupling of the shear-layer instabilities with the acoustic properties of the cavity and it is the interplay between the shear-layer instabilities and the cavity acoustics that cause each to excite, modify, and amplify the characteristics of the other.

Secondly, the impingement of high speed flow on the aft cavity wall results in a pressure fluctuation on the cavity boundary that causes the downstream reattachment region to act as an acoustic source.

This pressure source is part of a feedback loop between itself and the shear-layer via its interaction with the the shear-layer. While shear-layer instabilities and wall pressure fluctuations exist for all flow conditions over a cavity of sufficient size, their existence does not guarantee this resonant condition.

The existence of this resonant condition is governed by many quantities, such as the length-to-depth ratio (L/D), cavity volume, ratio of boundary layer thickness to cavity length (δ/L), Mach number of the free stream flow, ratio of shear-layer convection velocity to free stream velocity (κ), temperature ratio between the cavity and the free stream, and the state of the incoming boundary layer.

With the advent of more advanced tools for studying fluid dynamics (PIV and time dependent simulations) there have been several recent studies which have looked at specifics of

the flow field for a wide variety conditions. In the existing literature studies which involve quantitative flow measurement appear to be for cavities in incompressible flows (e.g. Grace et al, 2004, Ashcroft & Zhang, 2005, Ukeiley et al, 2005 and Kang et al, 2008) or supersonic flows (such as Zhuang, et al, 2006 and Unalamis et al, 2001) leaving the gap for the data in this manuscript to fill in. These studies have reinforced the importance of the incoming boundary layer and have allowed for studying the vortical structures. For example Grace et al. (2004) studied the effects of turbulent and laminar boundary layers on the flow features of an length to depth ratio 4 cavity in an incompressible flow. They found many of the flow properties to be altered by the state of the boundary layer and asserted that the in order to predict whether or not resonance might occur or match numerical data it is crucial to match the conditions of the upstream boundary layer. The lower speed such as Kang et al. (2008) and Aschcroft and Zhang (2005) along with the limited transonic studies such as Hirahara et al. (2007) which have acquired velocity measurements have been able to clarify some of the properties of the shear layer and its interaction with aft-wall as was originally proposed in Rockwell and Knisley (1979). Additionally these studies have showed linear growth of the shear layer width and hence the turbulent length scales in the shear layer along with some descriptions of the randomly sampled instantaneous velocity and vorticity fields demonstrating the large scale structures in the flow. Murray and Ukeiley (2003) developed a novel technique for estimating the time dependence of the large scale structure and applied it to the data being presented in this work in Murray and Ukeiley (2007). There it was shown how the propagation of the large scale structures in the shear layer is accompanied by a minima in the surface pressure and the idea of the number of turbulent structures across the cavities opening being associated with which Rossiter mode is dominant was validated.

1.2.2 Control of Cavity Flows

Techniques to suppress cavity oscillations can be classified in several ways. In this paper, we choose the classification detailed in of Cattafesta et al (2008) to be consistent with terminology used in active noise and vibration control. Active control provides *external* energy (e.g., mechanical or electrical) input to an adjustable actuator to control the flow, while passive control techniques do not. Passive control of cavity oscillations has been successfully implemented via geometric modifications using, for example, fixed fences, spoilers, ramps, (Heller & Bliss, 1975 and Shaw, 1979) and a passive bleed system (Chokani and Kim, 1991). Note that some control devices considered passive by this classification extract energy from the flow itself and have been called '*active*' by other researchers. Pertinent examples include unpowered or passive resonance tubes (Stanek et al, 2000) and cylinders or rods placed in the boundary layer near the leading edge of the cavity (Mcgrath & Shaw, 1996 and Ukeiley et al, 2004). These devices, described further in Section 3, are sometimes referred to as active because they provide an oscillatory input to the flow, but their effect on the flow cannot be adjusted without either changing the flow conditions or changing the device itself.

Active control is further divided into open- and closed-loop approaches. By its very definition, closed-loop control implies a feedback loop, in which some flow quantity is directly sensed or estimated and fed back to modify the control signal (Distefano et al, 1990). Open loop corresponds to the case when there is no feedback loop.

A further non-standard but useful classification of closed-loop flow control is that of quasi-static vs. dynamic feedback control. The quasi-static case corresponds to slow tuning of an open-loop control approach and occurs when the time scales of feedback are large compared to the time scales of the plant (i.e., flow). This approach is particularly relevant in nonlinear fluid dynamic systems, where the fundamental notion of frequency preservation in a linear system does not hold. The quasi-static approach was successfully used by Shaw and Northcraft (1998). The usual dynamic compensation case corresponds to the situation when the above time scales are commensurate. This can be implemented using an analog (see, for example, Williams et al, 2000) or "real-time" digital control systems (Cattafesta et al, 1999). In this context, "real time" refers to the situation in which the control signal is updated at the sampling rate of the data system, and the actuator responds to the flow state changes at the time scales of the dynamics.

1.2.2.1 Open Loop Suppression Techniques

It is impossible to include all prior research; there are numerous other (mostly passive) studies that have not been included here due to size constraints. Some key observations are discussed here.

Sarohia and Massier (1977) studied the efficacy of *steady* mass injection at the base or floor of two different axisymmetric cavity models for both laminar and turbulent boundary layers. While base injection was effective at suppressing cavity tones, large mass flow rates were required B_c of 5-15%. The value of that will be used through out this section involves normalizing the mass flow rate of the actuator normalized by the product of free stream density, free stream velocity and the area of the cavity.

Sarno and Franke (1994) studied static and oscillating fences, and also steady and pulsed injection (at 0° or 45° with respect to the free stream direction) at transonic speeds near the cavity leading edge. Blowing coefficients B_c of up to 7% were used. While the static fences provided the best suppression, the bandwidth of the mechanical fences was limited to < 220 Hz, while the pulsed injection was < 80 Hz. These frequencies were at least an order of magnitude lower than the frequencies of the cavity tones, and thereby constituted a quasi-static or low-frequency forcing. Nonetheless, they represented an important step in the evolution of active control of cavity oscillations, both in terms of approach and also the introduction of scaling laws for such actuators.

Vakili and Gauthier (1994) obtained significant acoustic tone attenuation with steady normal mass injection through variable-density porous plates upstream of the cavity leading edge at Mach 1.8 using $B_c \sim 4\%$. They attributed the attenuation to a thickening of the cavity shear layer and a corresponding alteration of its instability characteristics.

McGrath and Shaw (1996) subsequently studied mechanical oscillations of hinged flaps at frequencies up to 35 Hz over a range of subsonic and supersonic Mach numbers. Similar to the Sarno and Franke experiments, the forcing frequency was an order of magnitude lower than the resonant tone frequency. The static and oscillatory deflections were on the order of the boundary layer thickness δ and were shown to be effective despite their limited bandwidth.

MeGrath and Shaw were the first to study the effeet of a eylinder plaeed in the upstream subsonie boundary layer. Beeause of the well-known shedding eharaeteristies of a eireular eylinder of diameter d, $St = fd/U \approx 0.2$, over a wide Reynolds number range, this deviee was ealled a high-frequeney tone generator (HFTG). The eylinder was eapable of produeing substantial reduetions of both the eavity tones and the broadband. The authors attributed the potential meehanism of the aetuator to the interaetion of the shed vortiees with the shear layer instabilities. As will be diseussed later, however, there are additional possible meehanisms noted by other investigators that influenee the suppression effeetiveness of the eylinder.

At the same time in the mid-1990's, Ahuja and his eolleagues were investigating other novel eontrol strategies. For example, Mendoza and Ahuja (1996) studied the effeet of a steady wall jet on the tone produetion meehanism, using a Coanda surfaee. Although no mass flow measurements were obtained, upstream boundary layer profiles showed an inerease in δ with blowing, thereby leading to the hypothesis that the suppression was due to reduced amplifieation of the shear layer instabilities.

Hsu and Ahuja (1996) studied the effeet of a trailing-edge array of Helmholtz resonators (i.e., eommereial syringes) on eavity noise, and they obtained some suppression at lower Maeh numbers. At intermediate Maeh numbers, the resonators redueed the magnitude of the targeted tone, but new tones appeared at other frequeneies – a phenomenon that has been observed by many researehers. At high Maeh numbers, no suppression was obtained, but the authors believed that the reason was likely due to the diffieulty in setting the small resonator volume aeeurately. This study is noteworthy for its attempt to eontrol eavity oseillations in the vieinity of the aeoustie souree origin near the trailing edge impingement region. Generally, aetuators are plaeed at the leading edge of the eavity to leverage the growth of instabilities in the shear layer.

Cattafesta et al (1997) presented the use of a six-element piezoeleetrie flap array flush mounted at the leading edge of the eavity. The bandwidth of the aetuators was large enough (~300 Hz) to provide foreing at frequeneies eomparable to that of the eavity tones. Open-loop sinusoidal foreing at a suffieient amplitude and appropriate detuned frequeney was eapable of suppressing the eavity tone. Shear layer veloeity measurements indieated that the aetuators seeded the shear layer with a disturbanee that was large enough to prevent the growth of the natural eavity disturbanees. However, the possibility of starving the growth of natural instabilities at high subsonie and supersonie Maeh numbers is questionable, beeause of the large amount of mean flow energy available $\left(\sim M_\infty^2\right)$ for disturbanee amplifieation.

Shaw (1998) eontinued his study of leading-edge HFTGs, low frequeney pulsed fluidie injeetion, and oseillating flaps. While various diameter HFTGs mounted at a fixed height were shown to be effeetive, the suppression improved as the diameter was inereased. However, the relative height of the eylinder in the boundary layer was not reported, whieh is now known to be an important parameter. Shaw also diseussed two potential meehanisms of the HFTG: (1) high frequeney foreing due to shedding and (2) redueed shear layer growth rates due to boundary layer thiekening.

Resealing Shaw's pulsed blowing results show that they are eonsistent with prior results, sinee B_c values of a few pereent were required to suppress the tones. However, no spectra were reported to assess the impaet of blowing on the broadband noise. Interestingly, the tone

amplitude continued to decrease as the pulse frequency of the injector reached its upper limit of 100 Hz. Furthermore, normal injection was shown to be superior to tangential blowing.

The oscillatory flap frequency in Shaw's experiment was varied from 0-100 Hz and provided maximum suppression at 5 Hz. A monotonic improvement (reduction) in unsteady pressure level occurred as the dynamic deflection angle increased to its upper limit, corresponding to a deflection of order δ. However, the increase in δ for a full-scale aircraft led Shaw to conclude that this approach (low frequency, large amplitude, open-loop forcing) was not feasible for a full-scale aircraft.

In 1999, three new approaches were reported. Fabris and Williams (1999) used unsteady bleed (zero-net mass-flux) forcing to produce a broadband actuator capable of producing a complex input disturbance comprised of multiple frequency components. They demonstrated that the shear layer was most receptive to horizontal or tangential forcing via shear layer velocity measurements, in contrast to the results of Shaw (1998).

Lamp and Chokani (1997) used a rotary valve actuator to provide steady and/or oscillatory blowing upstream of the cavity leading edge at a particular pulsing frequency. Their actuator configuration emphasized three-dimensional effects and showed that oscillatory blowing can reduce tone amplitudes provided the forcing frequency is not a harmonic of the cavity resonance.

Raman et al (1999, 2004) used novel miniature fluidic oscillators to suppress cavity oscillations. These devices were capable of producing up to 3 kHz oscillations with mass flow rates of less than 0.12% of the main jet flow and produced significant tonal reductions. However, the mass flow rate and frequency of oscillations are coupled (albeit in a predictable fashion). Whether the steady mass addition or the unsteady oscillations were responsible for the sound suppression could not be determined. This is a key unresolved issue and, as emphasized in Rowley and Williams (2006), independent control of the mean and oscillatory components is required.

Stanek et al (2000, 2002 and 2003) reported on a series of larger-scale experiments conducted in the United Kingdom over the past few years. In the first experiment reported in 2000, they investigated powered resonance tubes, protruding piezoceramic driven wedges, a cylindrical rod, and passive resonance tubes vs. a conventional spoiler. An interesting result was that the powered resonance tubes demonstrated significant tonal and broadband reduction when $B_c \sim 1.6\%$. The result was termed a successful demonstration of high frequency forcing (defined as a frequency that is very large compared to that of the cavity tones).

A follow-on study reported in 2002 investigated powered and unpowered resonance tubes (in which the resonator tubes were blocked to inhibit high frequency excitation), and microjets vs. various other devices. While the powered resonance tubes were redesigned to reduce their mass flow requirements, optimal suppression still required $B_c \sim 0.6\%$. The unpowered resonance tubes consistently provided the best suppression, indicating that the primary suppression mechanism of these devices is not just due to high frequency forcing but is also influenced by the steady blowing component. The results also introduced microjet blowing, and showed that vertical blowing is required for these devices to be successful in this application.

Stanek et al (2003) offered a new explanation for the high-frequency forcing effect. The intrinsic idea was that high frequency forcing alters the instability characteristics such that the

growth of large scale disturbances is inhibited or prevented. They hypothesized that the mechanism was a *decelerated* energy cascade in contrast to the findings of Wiltse and Glezer (1998).

In 2003, Stanek et al. reported various aspects of the cylindrical rod in crossflow. They studied the vertical position of the rod H/δ in the boundary layer, its relative size d/δ, installation issues, and end conditions. They recommended an optimal location as centered at the edge of the boundary layer and an optimal size of $d/\delta = 2/3$. They argued that their results conclusively demonstrate that the suppression is due to high frequency forcing via vortex shedding from the cylinder. Additional arguments have also been provided that discuss the local stabilization of the shear layer via high frequency forcing. While the cylinder clearly affects the mean flow and its stability characteristics, there are other important factors that cannot be ignored, including experimental evidence presented by Ukeiley et al (2004) and the numerical simulations of Arunajatesan et al (2003) which indicate that the cylinder can also lift the shear layer and cause the impingement region to be altered. If the shear layer impingement location is indeed altered, then the source strength is presumably affected.

It is clear that these studies provide insufficient information to sort out these different physical mechanisms. To do so requires confirmation in the form of detailed experiments, analysis, and validated simulations to determine the mean velocity profile and subsequent shear layer instability characteristics for various high frequency devices.

There are a few other studies involving steady and/or pulsed blowing that have provided physical insight or have shown promising results. Bueno et al (2002) used an array of six fast-response (~3 ms) miniature jets mounted upstream of the leading edge to study the effects of normal injection on a Mach 2 cavity flow. They used instantaneous and ensemble-averaged pressure time histories and cross correlations to study the effects of single short and long cyclical pulses (50% duty cycle), the latter with relatively low forcing frequencies (50 or 80 Hz) compared to that of the tones. They compared their pulsed results to steady blowing with B_c = 0.28%, 0.24%, 0.18%, and 0.16% at L/D=5, 6, 8, and 9, respectively, and concluded that continuous mass injection is more effective for suppression than low frequency pulsed blowing.

Ukeiley et al (2003) used an array of eight powered whistles mounted in the forward cavity wall as flow control actuators. These devices essentially produce a high frequency tonal oscillation superimposed on a steady jet. The jet is directed in the downstream direction but has a slight vertical velocity component. The authors studied the novel use of different injection gases (heated air, nitrogen, and helium) with and without the high frequency "whistle" component. The best sound suppression results were obtained using steady helium blowing (no high frequency component) with very low B_c = 0.09%. The suppression mechanism requires further study, but sample Particle Image Velocimetry (PIV) images and cross correlations of pressure-time histories suggest that the injection alters the impingement region and disrupts the acoustic feedback loop. Their results also highlight the need to rigorously study high frequency forcing effects isolated from the mass flow injection from the actuator.

Zhuang et al (2003) investigated the use of a vertically directed microjet array mounted upstream of the cavity leading edge. The microjets had a 400 "m diameter and produced sonic jets that interact with the upstream boundary layer. The authors show how, at Mach 2, the microjets alter the cavity shear layer thickness and the receptivity process, introduce streamwise

vortieity, and alter the shear layer trajectory and the resulting impingement region. Signifieant tonal and broadband suppression levels were achieved with B_c as low as 0.15%, which is significantly lower than the mass injection required in other studies using steady blowing. Higher levels of B_c produeed no significant improvement.

Colleetively, the blowing results described above indieate that manually optimized steady blowing eonfigurations with $B_c \leq 0.2\%$ ean be effeetive suppression deviees. At subsonie speeds the primary meehanisms appear to be an alteration of the shear layer stability charaeteristies, the introduetion of streamwise vortieity, and shear layer impingement location. While these are also important at supersonie speeds, shoek wave/boundary layer interaetions at the upstream cavity edge and the ensuing shear layer trajeetory alteration appear to be additional faetors that should be considered.

It is interesting that when all of the available blowing data is expressed using the blowing coeffieient definition of Vakili and Gauthier (1994) one finds that the evolution of steady blowing teehniques has reduced the effective (not neeessarily optimal) B_c from O(10%) by two orders of magnitude down to O(0.1%).

High frequeney exeitation, whether it is passive or aetive, appears promising for both tonal and broadband suppression. However, the responsible meehanisms require further study. There is ample evidenee that high frequeney foreing alters the mean flow. As a result, the shear layer stability charaeteristies are altered and, in some eases, the trajectory of the shear layer is modified. When the impingement loeation is altered, the strength of the aeoustie souree is redueed and the broadband noise level deereases. To date elosed-loop control produees comparatively little ehange in the mean flow properties and, as sueh, has only been shown to be effeetive for tonal control.

1.2.3 Closed Loop Adaptive Control Approaches

Aetive feedbaek flow eontrol has been applied to the flow-indueed eavity oscillation problems over approximately the past 20 years. The elosed-loop eontrol approaches have advantages of redueed energy consumption (Cattafesta et al. 1997), no additional drag penalty, and robustness to parameter ehanges and modeling uneertainties. In general, elosed-loop flow eontrol measures and feeds back pressure fluctuations at the surface of the cavity walls (or floor) to an actuator at the cavity leading edge to suppress the eavity oseillations in a elosed-loop fashion.

In general, past active control stratcgies have taken one of two approaches for the purpose of reducing cavity resonance. First, they can thicken the boundary layer in order to reduee the growth of the instabilities in the shear layer. Alternatively, they ean be used to break the internal feedback loop of the eavity dynamies. Most closed-loop schemes exploit the latter approaeh. Early closed-loop control applieations used manual tuning of the gain and delay of simple feedbaek loops to suppress resonanee (Gharib et al. 1987; Williams et al. 2000a,b). Mongeau et al. (1998) and Kook et al. (2002) used an aetive spoiler driven at the leading edge and a loop-shaping algorithm to obtain signifieant attenuation with small aetuation effort. Debiasi et al. (2003, 2004) and Samimy et al. (2003) proposed a simple logic-based eontroller for

closed-loop cavity flow control. Low-order model-based controllers with different bandwidths, gains and time delays have also been designed and implemented (Rowley et al. 2002, 2003, Williams et al. 2002, Micheau et al. 2004, Debiasi et al. 2004). Linear optimal controllers (Cattafesta et al. 1997, Cabell et al. 2002, Debiasi et al. 2004, Samimy et al. 2004, Caraballo et al. 2005) have been successfully designed for operation at a single flow condition. These models are all based on reduced-order system models, and most of these controller design methods are based on model forms of the frequency response function, rational discrete/continuous transfer function, or state-space form. However, the coefficients of these model forms are assumed to be constant, and this assumption requires that the system is time invariant or at least a quasi-static system with a fixed Mach number.

Although the physical models of flow-induced cavity oscillations have been explored extensively, they are not convenient for control realization. This is because these models are highly dependent on the accuracy of the estimated internal states of the cavity system. In addition, cavity flow is known to be quite sensitive to slight changes in flow parameters. So a small change in Mach number can deteriorate the performance of a single-point designed controller (Rowley and Williams 2003). Therefore, adaptive control is certainly a reasonable approach to consider for reducing oscillations in the flow past a cavity. Adaptive control methodology combines a general control strategy and system identification (ID) algorithms. This method is thus potentially able to adapt to the changes of the cavity dimension and flow conditions. It updates the controller parameters for optimum performance automatically.

Two distinct loops are typically observed in the controller using this method. The outer loop is a standard feedback control system comprised of the process block and the controller block. The controller operates at a sample rate that is suitable for the discrete process under control. The inner loop consists of a parameter estimator block and a controller design block. An ID algorithm and a specified cost function are then used to design a controller that will minimize the output. The steps for real-time flow control include: (i) Use a broadband system ID input from the actuator(s) and the measured pressure fluctuation output(s) on the walls of the cavity to estimate the system (plant and disturbance) parameters. (ii) Design a controller based on the estimated system parameters. (iii) Control the whole system to minimize the effects of the disturbance, measured noise, and the uncertainties in the plant.

Based on this adaptive control methodology, some adaptive algorithms adjust the controller design parameters to track dynamic changes in the system. However, only a few researchers have demonstrated the on-line adaptive closed-loop control of flow-induced cavity oscillations. Cattafesta et al. (1999 a, b) applied an adaptive disturbance rejection algorithm, which was based upon the ARMARKOV/Toeplitz models (Akers and Bernstein 1997; Venugopal and Bernstein 2000, 2001), to identify and control a cavity flow at Mach 0.74 and achieved 10 dB suppression of a single Rossiter model. Other modes in the cavity spectrum were unaffected. Insufficient actuator bandwidth and authority limited the control performance to a single mode. Williams and Morrow (2001) applied an adaptive filtered-X LMS algorithm to the cavity problem and demonstrated multiple cavity tone suppression at Mach number up to 0.48. However, this was accompanied by simultaneous amplification of other cavity tones. Numerical simulations using the least mean squares (LMS) algorithm were shown by Kestens and Nicoud (1998) to minimize the output of a single error sensor. The reduction was associated with a single Rossiter mode, but only within a small spatial region around the error sensor. Kegerise et al. (2002) implemented adaptive system ID algorithms in an experimental cavity

flow at a single Mach number of 0.275. They also summarized the typical finite-impulse response (FIR) and infinite-impulse response (IIR) based system ID algorithms. They concluded that the FIR filters used to represent the flow-induced cavity process were unsuitable. On the other hand, IIR models were able to model the dynamics of the cavity system. LMS adaptive algorithm was more suitable for real-time control than the recursive-least square (RLS) adaptive algorithm due to its reduced computational complexity. Recently, more advanced controllers, such as direct and indirect synthesis of the neural architectures for both system ID and control (Efe et al. 2005) and the generalized predictive control (GPC) algorithm (Kegerise et al. 2004), have been implemented on the cavity problems.

From a physical point of view, the closed-loop controllers have no effect on the mean velocity profile (Cattafesta et al. 1997). However, they significantly affect streamwise velocity fluctuation profiles. This control effect eliminates the strength of the pressure fluctuations related to flow impingement on the trailing edge of the cavity. Although closed-loop control has provided promising results, the peaking (i.e., generation of new oscillation frequencies), peak splitting (i.e., a controlled peak splits into two sidebands) and mode switching phenomena (i.e., non-linear interaction between two different Rossiter frequencies) often appear in active closed-loop control experiments (Cattafesta et al. 1997, 1999 b; Williams et al. 2000; Rowley et al. 2002 b, 2003; Cabell et al. 2002; Kegerise et al. 2002, 2004a).

Explanations of these phenomena are provided by Rowley et al. (2002b, 2006), Banaszuk et al. (1999), Hong and Bernstein (1998), and Kegerise et al. (2004). Rowley et al. (2002b, 2003) concluded that if the viewpoint of a linear model was correct, a closed-loop controller could not reduce the amplitude of oscillations at all frequencies as a consequence of the Bode integral constraint. Banaszuk et al. (1999) gave explanations of the peak-splitting phenomenon. They claimed that the peak splitting effect was caused by a large delay and a relatively low damping coefficient of the open-loop plant. Cabell et al. (2002) explained these phenomena by the combination of inaccuracies in the identified plant model, high gain controllers, large time delays and uncertainty in system dynamics. In addition, narrow-bandwidth actuators and controllers may also lead to a peak-splitting phenomenon (Rowley et al. 2006).

Hong and Bernstein defined the closed-loop system disturbance amplification (peaking) phenomenon as spillover. They illustrated that the spillover problem was caused by the collocation of disturbance source and control signal or the collocation of the performance and measurement sensors. For this reason, the reduction of broadband pressure oscillations was not possible if the control input was collocated with the disturbance signal at the leading edge of cavity. Therefore, Kegerise et al. (2004) suggested a zero spillover controller which utilized actuators at both the leading and trailing edges of the cavity for closed-loop flow control.

1.3 Objectives

There were several objectives of this study which were;

- Develop methodology that will allow for the study of time dependent features.

- Formulate an approach that can utilize time dependent velocity and density field information to investigate the sources of the large fluctuating pressures observed in cavities.
- Develop a tool that can be used for quantitatively asses the density field that can be used in accordance with the estimation procedure.
- Refine and apply a closed loop flow control strategy to demonstrates the effectiveness
- Conduct studies to examine the differences in the flow structure between natural and effectively controlled flows

1.4 Layout of this Document

In this document we will discuss our accomplishments during the course of this AFOSR grant all of which are pieces that will allow for us to efficiently reduce the surface pressure fluctuations in open cavities in supersonic flows. The remaining parts of the document contain a chapter on each one of these pieces. Chapter 2 presents the methodology and application for the estimation of the time dependent velocity field based on surface pressure. Additionally we will present a method for method of integrating the velocity field with Poisson's equation to calculate the different components of the sources of the fluctuating surface pressure. In Chapter 3 data acquired in both a controlled and uncontrolled Mach 1.5 flow over an open cavity is analyzed with the Proper Orthogonal Decomposition to evaluate similarities in the flow structure. Chapter 4 demonstrates the "state of the art" in adaptive flow control for surface pressure reductions in flow over a cavity along with a zero net mass flux actuator. In Chapter 5 we present the development and application of optical deflectometry which in the future can be used in conjunction with synchronous surface pressure fluctuation measurements for the time dependent flow field estimation procedure.

2 Estimation of Time Dependent Phenomena

2.1 Methodology

Redueed order deseriptions are needed to deseribe eomplex flows, like that over a eavity, so that the underlying physical meehanisms ean be interpreted. Over the past deeade, methodologies for estimating low dimensional deseriptions of a time-resolved flow field using boundary information have proven to be instrumental in fluid dynamies. Some of the more promising methodologies are rooted in large seale turbulent structure deteetion teehniques sueh as Stochastie Estimation (Adrian 1975) and the Proper Orthogonal Decomposition (Lumley 1967).

The Proper Orthogonal Deeomposition (POD) is a mathematieally unbiased technique for decomposing a flow field into an orthonormal basis set whieh is optimal in a mean square sense. This basis set is found from the solution of the following integral eigenvalue problem,

$$\int_{\Omega} R_{ij}\left(\hat{x},\hat{x}'\right)\phi_j^n\left(\hat{x}'\right)d\hat{x}' = \lambda^n\phi_i^n\left(\hat{x}\right) \tag{2.1}$$

where λ is the eignevalue and represents the weight of each given mode and ϕ are the orthogonal eigenfunetions whieh represent the spatial distribution of the basis set. The kernel R_{ij} is the two-point spatial-correlation tensor and ean be formulated for sealar or veetor flow properties sueh as the density and velocity fields that will be discussed below. Hilbert-Schmidt (see Holmes et al. 1996) theory specifies that there is a denumerable set of the eigenmodes that are orthonormal, and that the instantaneous field, in this example veloeity, can be represented as a linear combination of the product of time dependent coefficients with spatial basis funetions

$$u_i^n\left(\hat{x},t\right) = \sum_n a^n\left(t\right)\phi^n\left(\hat{x}\right) \tag{2.2}$$

where the expansion coefficients are ealeulated from

$$a^n\left(t\right) = \int_{\Omega} u_i\left(\hat{x},t\right)\phi_i^n\left(\hat{x}\right)d\hat{x}\,. \tag{2.3}$$

In order to obtain the time dependence of the expansion coefficients, the approaeh requires that the time-resolved instantaneous field is known at all spatial locations simultaneously to solve the integral in equation 2.3. This condition is not usually met in experiments, and one must use alternative methods, such as the Stochastic Estimation or low dimensional models based on Galerkin projeetions (Ukeiley et al. 2001) to determine the time dependenee of the expansion coefficients.

The use of Stochastic Estimation eombined with the POD has been termed "*modified* Stochastic Estimation" (mQSE) in the literature and has been used extensively for studying the time dependent features of subsonic eavity flow (Ukeiley and Murray 2005 and Murray and Ukeiley 2007). Perhaps one of the most important and novel features of the application in those studies was the use of the surfaee pressure as the estimation condition. In partieular, sinee time-resolved pressure measurements are readily obtained, this results in a time-resolved estimate of the low-dimensional veloeity field. The estimation can be written as

$$\tilde{a}^n(t) = \left\langle a^n(t) \mid p_k(t) \right\rangle \tag{2.4}$$

which states that the POD expansion coefficient is estimated given statistical information about its relationship to the surface pressure at several locations k. Just as with the formulation of the conventional stochastic estimation procedure, the estimated POD expansion coefficient can be written in a series expansion as

$$\tilde{a}^n(t) = A_{nk} p_k(t) + B_{nlm} p_l(t) p_m(t) \tag{2.5}$$

which has been truncated at the quadratic term (see Murray and Ukeiley 2003 for a validation). Minimizing the mean-square error between the estimated and true expansion coefficient results in a matrix equation

$$[C] = [P]^{-1}[V]. \tag{2.6}$$

where the matrices represent the various correlations between the surface pressure with itself and the surface pressure with the POD expansion coefficients and their explicit definitions can be found in Murray and Ukeiley (2007). Finally, the time dependent estimated velocity field can be reconstructed solving equation 2 with the solutions from equation 5.

Figure 1 summarizes the estimation procedure that is used to obtain the time dependent low-dimensional description of the cavity flow field. The top of this figure demonstrates that one starts from time resolved surface pressure data and independent snapshots of either the velocity or density fields. Then, through the equations described above, one estimates a low-dimensional representation of these fields as depicted by the dashed red lines in the bottom part of the figure.

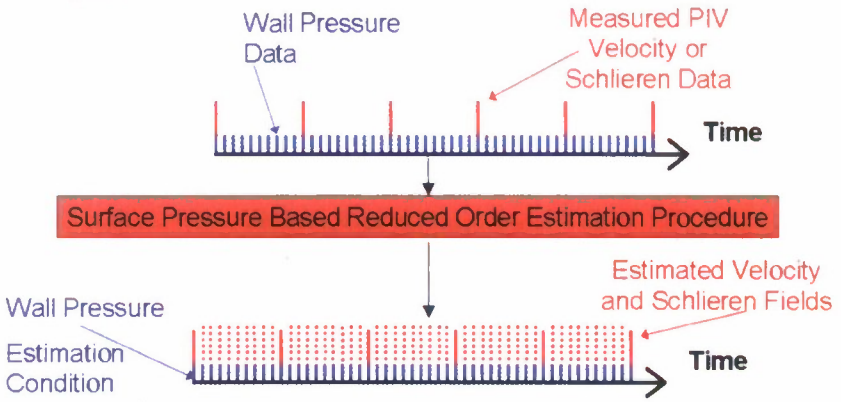

Figure 1: Flow Chart of Time Dependent Estimation Procedure.

It can be noted that in the formulation above we are using a static estimator of the flow field. However in the applications discussed below, the array of surface pressure sensors spans the whole domain of interest, which overcomes the need to account for convection in the flow field. However, we will present work below that uses a dynamic estimator of the surface pressure to incorporate memory effects.

2.2 Application

There were two sets of pressure data utilized in performing the mQSE. The first set, $P_k(t_\theta)$, are the pressure values associated with the θ=1 to M snapshots of the flow field. These values are used to calculate the correlations necessary to compute the estimation coefficients. If $P_k(t_\theta)$ is then reused to estimate the velocity field at every θ, the estimation effectively attempts to reconstruct the PIV data. This allows the estimated flow field and single-point statistics to be compared with the original data. The second set of pressure data, $P_k(t_\theta)$, represent θ=1 to N time-resolved pressure measurements sampled at 90 kHz. This data was used to estimate the time dependence of the flow using the mQSE. The results of this estimation are presented for several free stream Mach numbers. For all the estimates, the mQSE is applied only to the fluctuating quantities.

Evaluation of the Velocity Estimation

Based on the results from the Gappy POD to the experimental data set used here (see Murray and Ukeiley, 2007), only the first 8 POD modes were used in the mQSE to estimate the velocity field. The fraction of the total kinetic energy represented by these first 8 POD modes can be calculated by summing over the respective eigenvalues. At each Mach number, the first 8 POD modes account for approximately 50% of the total energy. Therefore, in order to match the kinetic energy present in the original data, the estimated velocity fluctuations were scaled up by the reciprocal of the include energy fraction. For example, if 8 modes represented 49% of the total energy, the estimated velocity fluctuations were scaled up by a factor of 2.04.

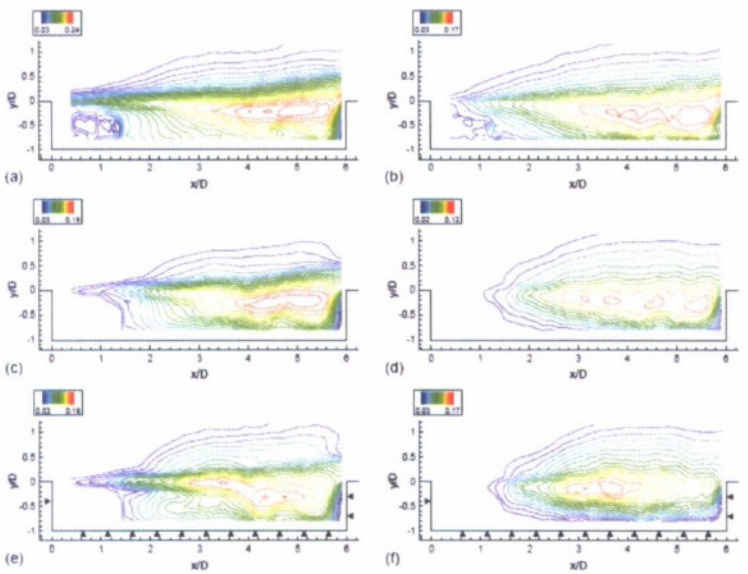

Figure 2: Comparison of the turbulence intensities between the PIV data and the mQSE estimation of the flow field for Mach 0.58: (a), (c), & (e) are streamwise turbulence intensity and (b), (d), & (f) are wall-normal turbulence intensity. (a) & (b) are from the PIV data, (c) & (d) were calculated from an 8 mode POD reconstruction of the PIV data, and (e) & (f) are from the mQSE estimation.

Figure 2 compares the streamwise and wall-normal turbulence intensities resulting from the mQSE estimation with the statistics of the original PIV data. Plots (a) and (b) show the turbulence intensities for the PIV data. In plots (c) and (d), the statistics were calculated for the PIV data after first reconstructing the snapshots using the first 8 POD modes. Plots (e) and (f) show the statistics calculated from the mQSE estimation of the PIV data. The contour levels show general agreement in both structure and magnitude between the original data and the mQSE estimation. Similar results were obtained for the other Mach numbers. A qualitative evaluation of the estimate is presented in figure 8 where a PIV snapshot taken from the Mach 0.58 data set is estimated using the associated pressure measurements plotted at the bottom of the figure. Plot (a) shows the original PIV data, and plot (b) shows an 8 mode POD reconstruction of the same snapshot. In plot (c) this snapshot has been estimated with the mQSE using the pressure distribution in plot (d). In all the plots of the flow field, the contours which outline the spanwise vorticity have the same magnitudes and the vectors are plotted using the same reference length. The validity of the chosen scaling parameter (based on the percentage of energy included in the first 8 POD modes) is demonstrated because the strength of the spanwise vorticity in (c) compares more favorably with the original PIV data in (a) than the 8 mode POD reconstruction shown in (b). However, the structure of the vorticity field in (c) is very similar to that in (b) which demonstrates the filtering that results from using only the first 8 POD modes in the mQSE.

Time Dependent Estimation of the Flow Field

The results presented in this section demonstrate the temporal dynamics of the flow field estimated using the mQSE. The main focus here is the comparison between the flow field dynamics and the instantaneous surface pressure loads which are shown along with each realization of the flow.

Each figure in this section shows nine consecutive realizations of the flow field. They are arranged such that time proceeds from top-to-bottom and left-to-right in each figure starting at t_0 and following at the noted intervals. The wall-pressure distribution is plotted directly below each image of the flow field using a bar-chart with a connecting spline curve. The discussion that follows also takes into account observations made by examining extended time-series animations.

Figure 3 through Figure 7 show the temporal evolution of the velocity field estimated using the mQSE. Contours of clockwise rotating spanwise vorticity are also shown in the plots. Figure 3 shows the mQSE results for the Mach 0.19 flow. Examination of the estimated time-series does not demonstrate a clear downstream propagation of structures in the shear layer (a downstream motion could only be noticed sporadically). Additionally, the surface pressure loads do not exhibit a clear wave-like structure. However, it is evident that increases in the wall pressure on the cavity floor occur below regions where the shear-layer streamlines are curved away from the cavity while decreases in the pressure accompany curvatures toward the cavity. The stream-traces, which were plotted using Tecplot's built-in utility, demonstrate the prevailing motion that occurs in the flow: The circulation region inside the cavity oscillates back and forth without any clear periodicity. Likewise, the aft-wall pressure loads, which are larger than at any other measurement location, were found to oscillate from large negative to large positive without a well-defined regularity. However, it did appear that the aft wall pressure was related to the shear layer streamlines either stagnating on or lifting over the aft wall. Figure 4 shows very

similar results for the Mach 0.29 flow. At this Mach number the shear layer still shows intermittent patterns of downstream propagating structures. In contrast to the Mach 0.19 flow, this intermittency is increased which explains the presence, while small in magnitude, of Rossiter tones in the measured spectra. This demonstrates the onset of well organized cavity flow oscillations that will become well defined at Mach 0.39. These results suggest that fully developed oscillations become sustained for the current configuration around Mach 0.3.

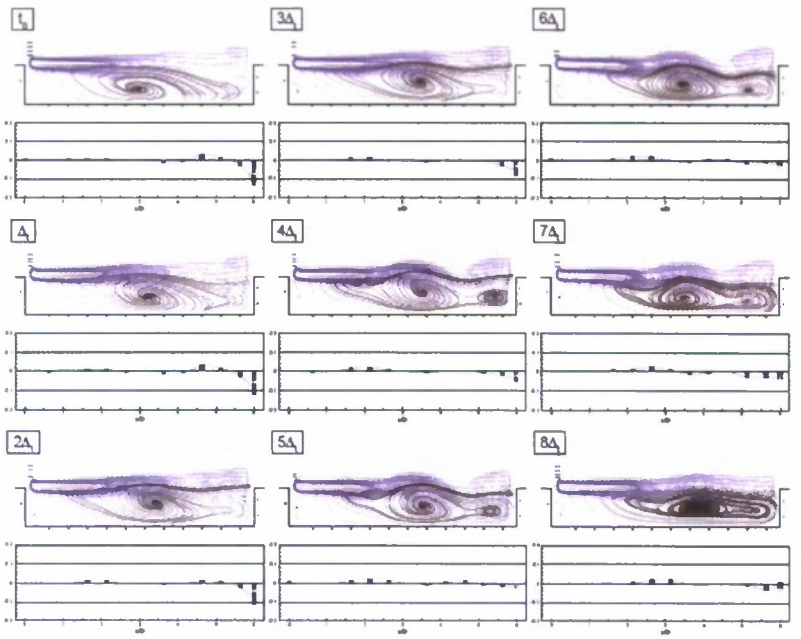

Figure 3: mQSE estimation of the Mach 0.19 cavity flow, $\Delta t = 44\mu s$. Contours outline areas of large negative spanwise vorticity. Streamtraces were plotted using Tecplot's streamtrace utility. Pressure values are in psi and plotted at their respective x/D location.

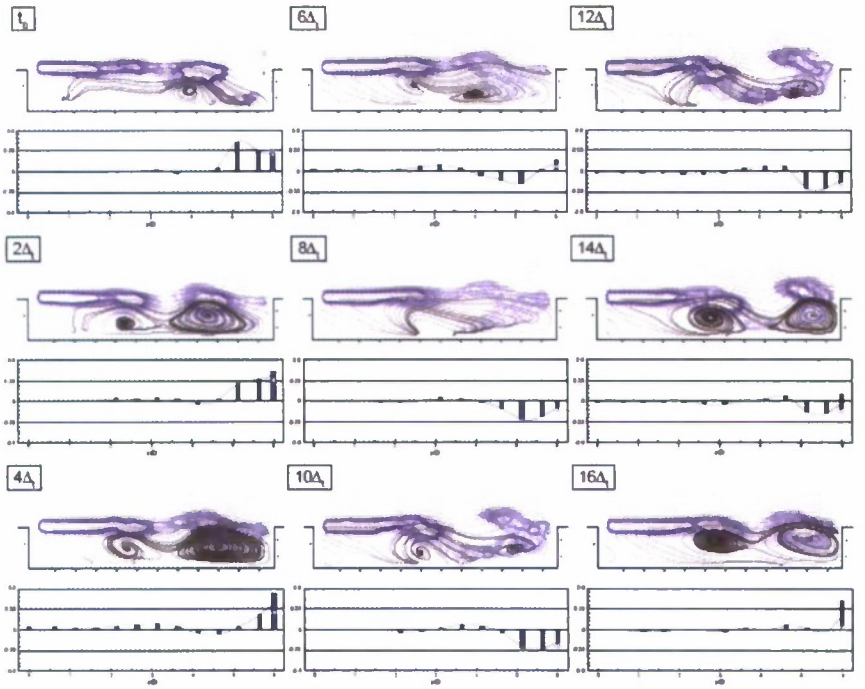

Figure 4 : Estimation of Mach 0.29 cavity flow: $\Delta t = 33\mu s$.

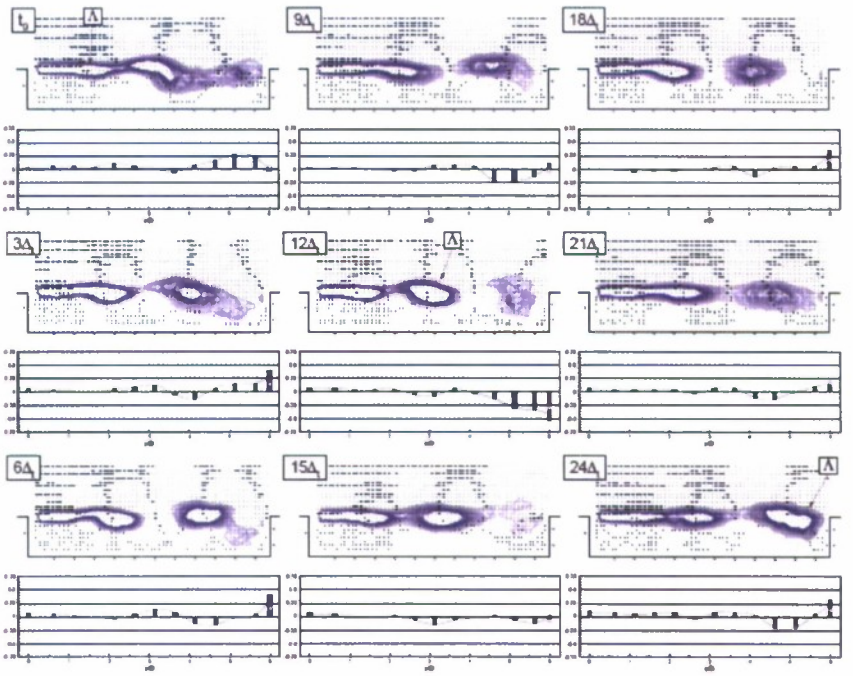

Figure 5: Estimation of Mach 0.39 cavity flow: $\Delta t = 22\mu s$.

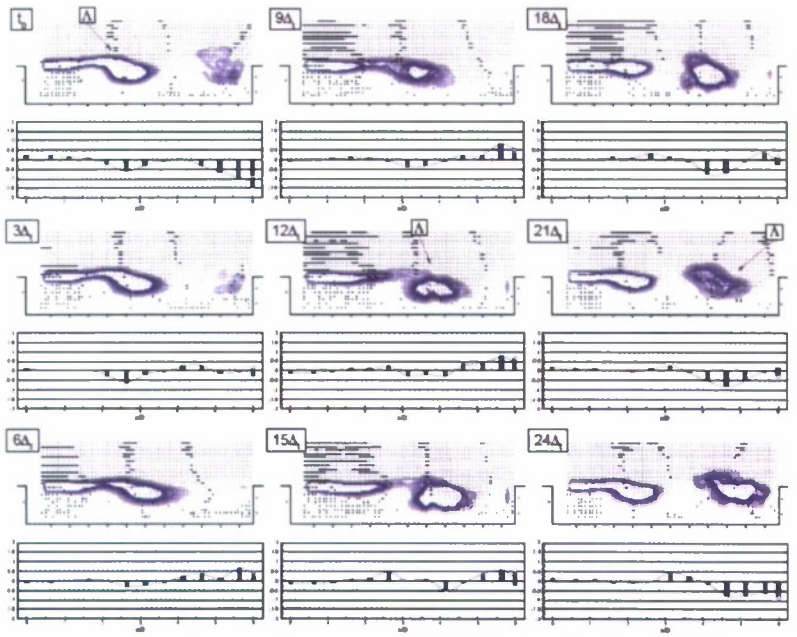

Figure 6: Estimation of Mach 0.58 cavity flow: $\Delta t = 11\mu s$.

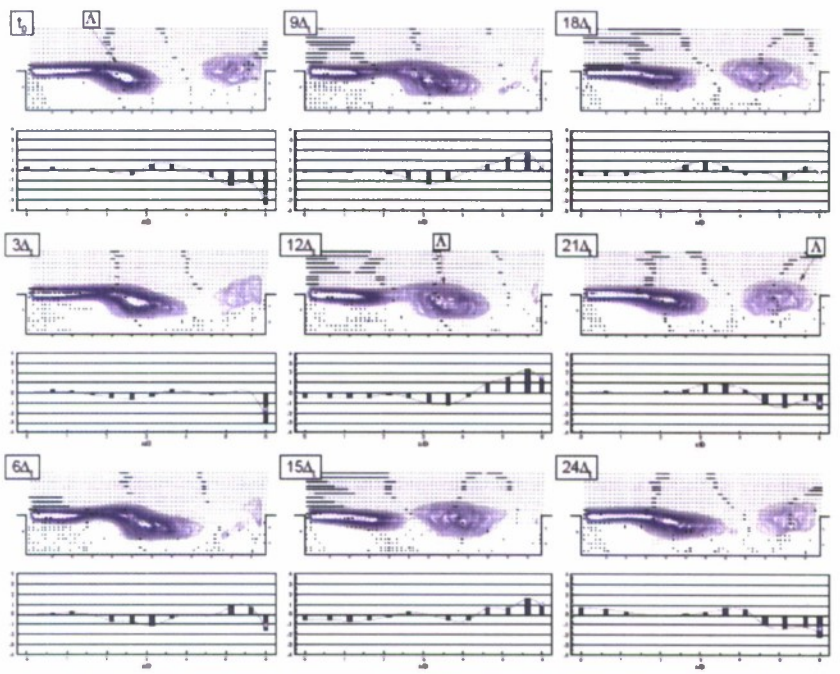

Figure 7: Estimation of Mach 0.73 cavity flow: $\Delta t = 11\mu s$.

Figure 5, Figure 6 and Figure 7 show the results for Maeh 0.39, 0.58, and 0.73 respeetively. Here, the stream-traees have been removed beeause the formation and downstream propagation of spanwise vortex struetures is elearly evident as shown by the eontour lines. In eaeh figure, a strueture is labeled as Λ and followed as it moves downstream through the shear layer. The loeation of the strueture is always aeeompanied by a negative pressure fluetuation on the eavity floor below it. The dominanee of a partieular Rossiter mode is observed in these figures by notieing the number of struetures that oeeupy the shear layer at any instant. At Maeh 0.39, there are generally two struetures with a third either forming or passing over the aft wall. This is eonsistent with Rossiter mode 3 whieh was shown to be dominant at this Maeh number. Similarly, at Maeh 0.58 and 0.73, there is generally only one strueture with another being either formed or interaeting with the aft wall. This is eonsistent with Rossiter mode 2 whieh is the dominant mode for these Maeh numbers. The estimated temporal evolution of the higher Maeh numbers demonstrates the relationship between the vortex struetures and the aft-wall pressure loads. Positive pressure fluetuations oeeur just after a vortex strueture has passed over the aft wall and the shear layer is then pulled into the eavity by the eireulation of the approaehing vortex. This eauses the shear layer to impaet the aft wall and stagnate there. Then, as the approaehing vortex reaehes the aft wall it brings the low pressure at its eore along with it while also defleeting the shear layer over the aft-wall resulting in a deerease in the pressure.

2.3 Source Identification

2.3.1 Methodology

An explieit equation for the pressure in terms of the veloeity ean be written for the ineompressible flow by taking the divergenee of the momentum equation and eliminating terms using the eontinuity requirement. The result is Poisson's equation:

$$\nabla^2 P = -\rho \frac{\partial^2}{\partial x_i \, \partial x_j} U_i U_j. \tag{2.7}$$

Taking eues from the work by Kraiehnan (1956) the above equation ean be integrated to give the instantaneous pressure, P(x, t), at a point, x, on a solid surfaee:,

$$P(\vec{x}, t) = 2\frac{\rho_0}{4\pi} \int_{y_2>0} \frac{\partial^2 U_i(\vec{y}, t) U_j(\vec{y}, t)}{\partial x_i \, \partial x_j} \frac{d^3\vec{y}}{|\vec{x} - \vec{y}|}, \tag{2.8}$$

where the integration is earried out over the positive half-plane ($y_2 > 0$) where the flow exists and a multiplieative faetor of 2 is ineluded so that the flow (souree region) is effeetively mirrored aeross the bounding surfaee.

Setting **x** = 0, defining r = |**x**−**y**|, and performing a double partial integration on the double divergenee of the veloeity produet yields

$$P(t) = \frac{\rho_0}{2\pi} \int_{y_2>0} d^3\vec{y} \underbrace{\left(\frac{3y_i y_j - r^2\delta_{ij}}{r^5}\right)}_{Q_{ij}} \underbrace{U_i(\vec{y},t)U_j(\vec{y},t)}_{R_{ij}}. \tag{2.9}$$

The term Q_{ij} is the classic form for a traceless tensor and drops off rapidly with $1/r^5$. If the cross-stream velocity, U_3, is zero, five of the nine terms in $Q_{ij}R_{ij}$ are eliminated which simplifies the integral:

$$P(t) = \frac{\rho_0}{2\pi} \int_{y_2>0} d^3\vec{y} \left[\underbrace{\left(\frac{3y_1 y_1 - r^2}{r^5}\right)}_{A} U_1U_1 + \underbrace{\left(\frac{6y_1 y_2}{r^5}\right)}_{B} U_1U_2 + \underbrace{\left(\frac{3y_2 y_2 - r^2}{r^5}\right)}_{C} U_2U_2 \right]. \tag{2.10}$$

With $U_3 = 0$, the quadrupole becomes aligned with the streamwise direction and inclined by 45 degrees to the horizontal. However, this does not completely remove the dependence of the calculated pressure on the cross-stream coordinate, y_3, because it is still included in the distance r^2. Figure 8 shows Q_{ij} plotted relative to the physical dimensions of the cavity showing the orientation and extent of the quadrupole for a calculation of the surface pressure at the center of the cavity floor. The figure demonstrates how fast the magnitude drops of with $1/r^5$ and shows that the effects of the end walls will be negligible for locations near the center of the cavity.

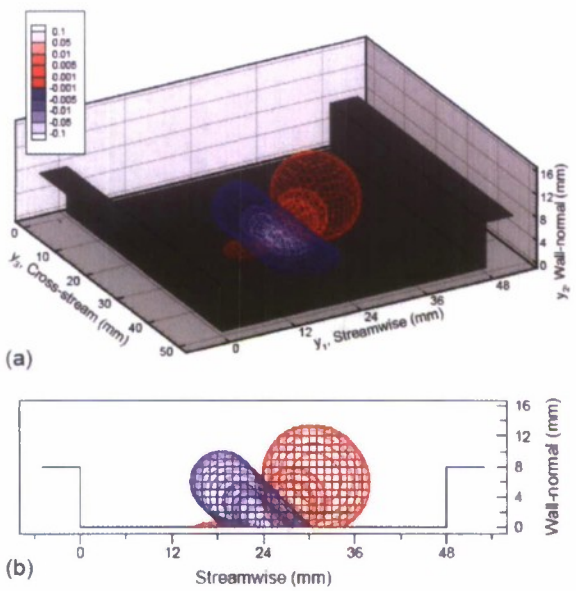

Figure 8: Depiction of the quadrupole Qij plotted relative to the physical dimensions of the rectangular cavity. Flow would be in the positive streamwise direction. The position of the quadrupole in the cavity is appropriate for calculating the surface pressure at the center of the cavity: (a) shows the full 3-dimensional extentand orientation of the quadrupole in the cavity for U3 = 0, (b) shows a 2-D slice along the cavity centerline.

Decomposing the pressure and velocity into mean and fluctuating components allows equation (2.7) to be written for the fluctuating pressure,

$$\nabla^2 p = -\rho \frac{\partial^2}{\partial x_i \partial x_j} \left(\underbrace{\overline{U}_i u_j + \overline{U}_j u_i}_{1} + \underbrace{u_i u_j - \overline{u_i u_j}}_{2} \right), \tag{2.11}$$

dependent on velocity source terms that are linear (1) and non-linear (2) with respect to the fluctuating velocity. This fluctuating pressure can be directly compared to the signals measured during the experiments using the wall-mounted pressure transducers. The integration in equation (2.10) can be applied separately to the linear and non-linear terms in equation (2.11). This allows an estimate of the pressure fluctuations associated with the mean-shear, p_{ms}, and turbulence-turbulence, p_{tt}, contributions to be computed separately and compared:

$$\tilde{p}_{ms}(\eta\Delta_t) = \frac{\rho_0}{2\pi} \sum_{n\,m\,z} \Delta_x \Delta_y \Delta_z \left[2A\overline{U}_1 \tilde{u}_1 + B(\overline{U}_1 \tilde{u}_2 + \overline{U}_2 \tilde{u}_1) + 2C\overline{U}_2 \tilde{u}_2 \right], \tag{2.12a}$$

$$\tilde{p}_{tt}(\eta\Delta_t) = \frac{\rho_0}{2\pi} \sum_{n\,m\,z} \Delta_x \Delta_y \Delta_z \left[A(\tilde{u}_1 \tilde{u}_1 - \overline{u_1 u_1}) + B(\tilde{u}_1 \tilde{u}_2 - \overline{u_1 u_2}) + C(\tilde{u}_2 \tilde{u}_2 - \overline{u_2 u_2}) \right]. \tag{2.12b}$$

The coefficients, A, B, and C, are defined in equation (2.10), and the mQSE estimated velocity fluctuations, u_i, provide time-dependent data for the calculation of the pressure fluctuations. Note that the mean quantities, U_i and $u_i u_j$, are computed directly from the PIV data and not from the mQSE estimation results.

In (2.12), the integration from (2.10) has been replaced by a summation with weights, Δx, Δy, and Δz for a trapezoidal approximation. In the streamwise and wall-normal directions, the spatial resolution of the PIV data dictates that $\Delta x = \Delta y = 0.8$ mm. The variation of the quadrupole in the spanwise direction must be accounted for; however, velocity data was measured (and therefore estimated) in a plane at only a single spanwise location (on the centerline). Therefore, for the purposes of this calculation, the velocity field was assumed to be homogeneous in the spanwise direction such that $U_i(y3) = U_i(y'3)$. This is not a valid assumption in terms of the flow physics, but it was used here out of necessity to carry out the calculation in (2.12). Finally, the width of the cavity was segmented into 10 equal parts such that $\Delta z = 5.08$ mm, and the velocity field was assumed to be the same in each spanwise segment.

Equation (2.12) was used to calculate p_{ms} and p_{tt} at the floor locations where the pressure fluctuations were measured during the experiment. The contribution of the linear and non-linear sources can be summed to give an estimate of the total fluctuating pressure load, $p_k(\eta\Delta t) = p_{ms,k}(\eta\Delta t) + p_{tt,k}(\eta\Delta t)$. This allows a direct comparison between the estimated and measured pressure loads for the same instants in time.

2.3.2 Source Identification Application

Figure 9 and Figure 10 show the time history of the measured cavity floor pressure loads at Mach 0.19 and 0.73 compared to the estimated fluctuations calculated from equation (16). In

each figure, time has been normalized by the convection velocity, $0.57U_{inf}$, and the cavity length, L, such that $\tau = 0.57U_{inf}t/L$. The results from these two Mach numbers are representative of all the Mach numbers studied here. At each Mach number, the measured pressure loads exhibit a predominant downstream propagation that occurs over a single cycle. This downstream motion becomes more dominant at the higher Mach numbers with a more pronounced periodicity and is represented well by the estimated pressure loads. Compared to p_{ms} and p_{tt}, only the mean-shear contribution to the pressure loads exhibits this same downstream propagation and periodicity. This observation suggests that the resonant features of the cavity are primarily related to the mean-shear contribution to the pressure loads.

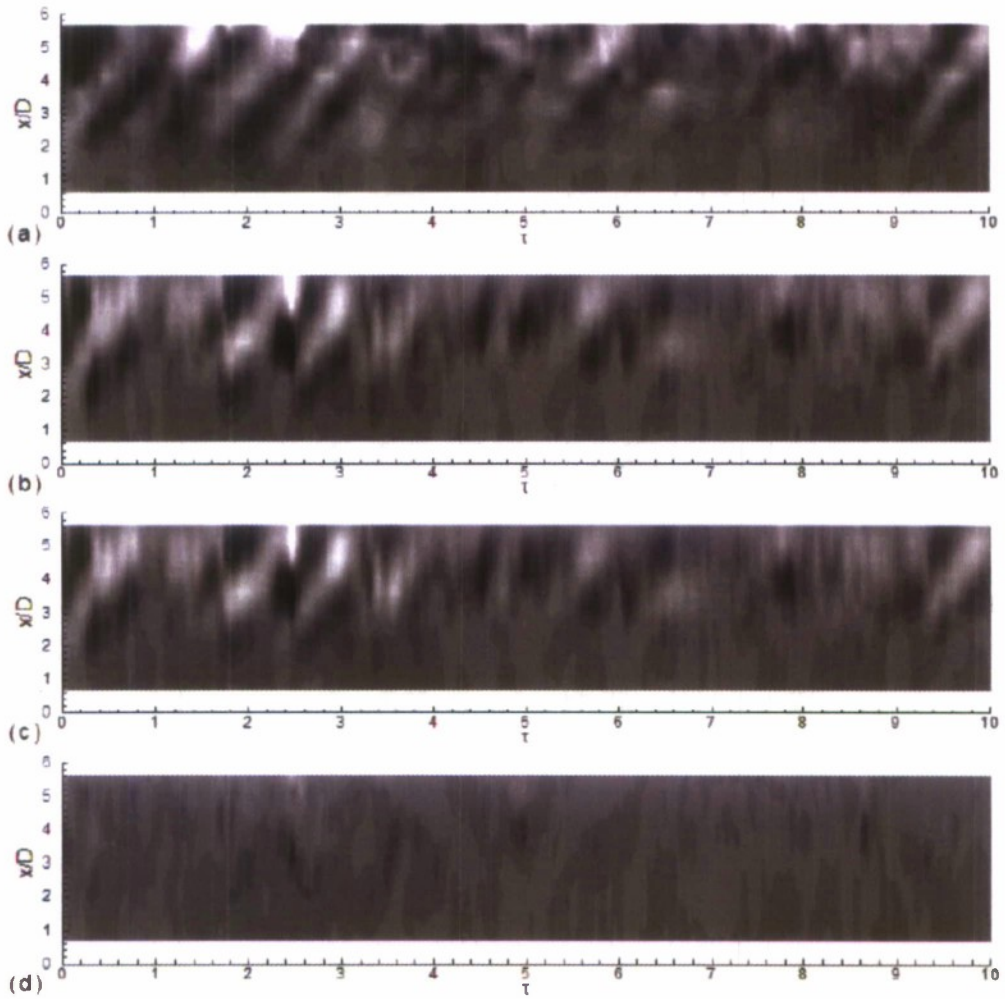

Figure 9: Time history of the estimated wall-pressure loads at Mach 0.19: (a) measured values used to calculated the estimated velocity field, $p_k(\eta\Delta t)$; (b) estimated pressure fluctuations, $p_k(\eta\Delta t)$; (c) estimated contribution to the pressure from the mean-shear component, $p_{ms,k}(\eta\Delta t)$; (d) estimated contribution from the non-linear component, $p_{tt,k}(\eta\Delta t)$. The time has been normalized such that $\tau = 0.57U_{inf}t/L$. Contour range is±0.08 psi and black is negative.

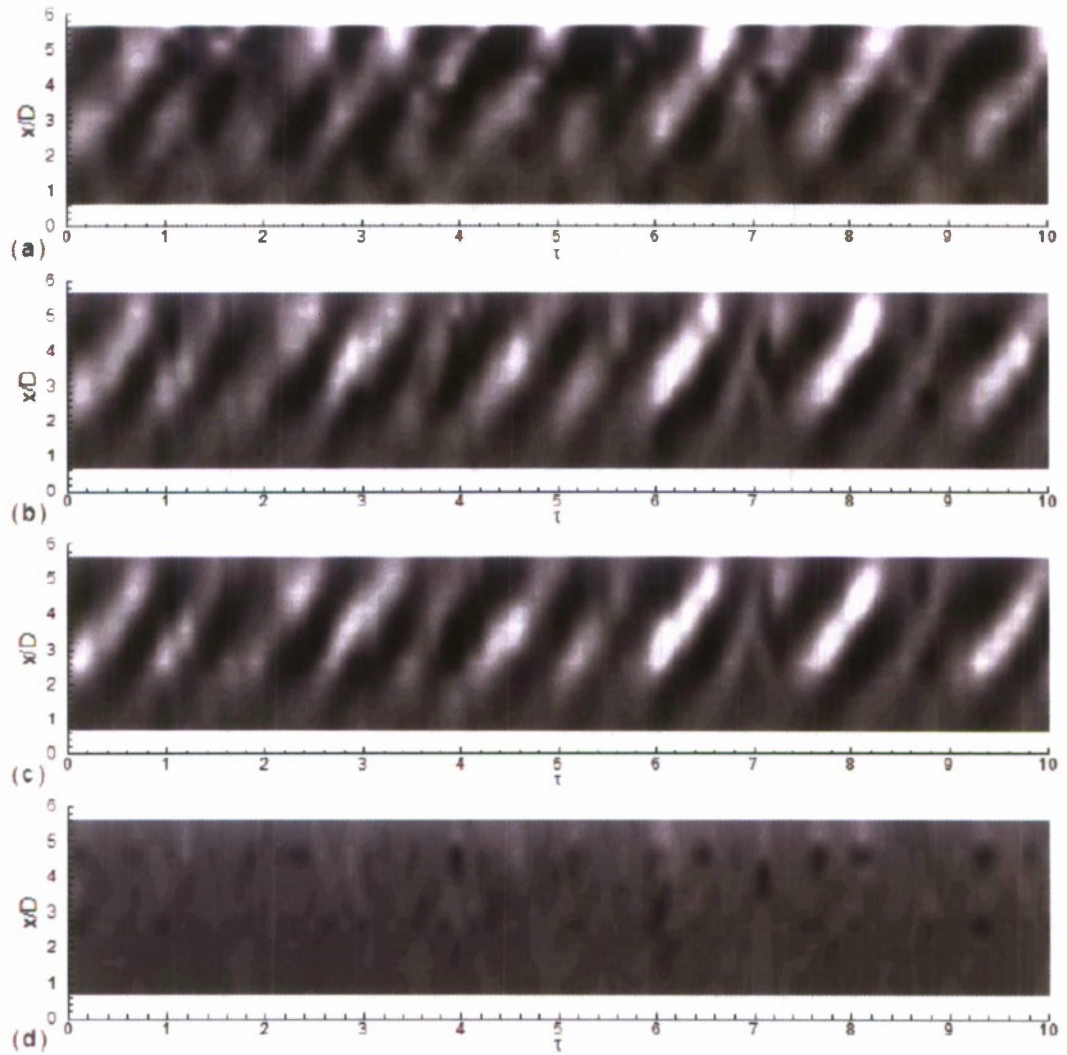

Figure 10: Time history of the estimated wall-pressure loads at Mach 0.73: (a) measured values used to calculated the estimated velocity field, $p_k(hDt)$; (b) estimated pressure fluctuations, $p_k(hDt)$; (c) estimated contribution to the pressure from the mean-shear component, $p_{ms,k}(hDt)$; (d) estimated contribution from the non-linear component, $p_{tt,k}(hDt)$. The time has been normalized such that $t= 0.57U_{inf}t/L$. Contour range is±0.08 psi and black is negative.

Figures 7 through 9 show the auto-spectral density of the measured pressure loads on the cavity floor compared to the spectra of the estimated pressure fluctuations and the contributions of the mean-shear and non-linear velocity sources. The one-sided auto-spectral density plotted in the figures, $G(\zeta\Delta_f)$, was calculated as

$$G_k(\zeta\Delta_f) = 2\langle \hat{p}_k^*(\zeta\Delta_f)\hat{p}_k(\zeta\Delta_f)\rangle/\Delta_f \tag{2.13}$$

where $p_k(\zeta\Delta_f)$ is a 1024 point FFT of the pressure, p* denotes the complex conjugate, and <·> denotes ensemble averaging over the 16 blocks of data. Results for Mach 0.19, 0.39 and 0.73 are shown and represent the same features found in the results at Mach 0.29 and 0.58.

The estimates p_2 and p_{12} both under-predict the magnitudes compared to the measured pressure spectra. This is most likely related to neglecting the effect of the end walls but could also be influenced by the limited extent of the PIV data. Nevertheless, the estimated pressure spectra still exhibit the resonant features at these measurement locations.

The broadband levels (particularly for the non-linear contribution) tend to be relatively flat and are often larger than that of the measured values at the higher frequencies. This is likely a result of the uncertainty in the PIV data. Assuming that the integration of equation (2.12) causes random error to have little relevance, the bias uncertainty in the PIV data becomes the primary source of error for the pressure calculation. Given a bias uncertainty of approximately 0.4 m/s with 1200 samples of the velocity in the PIV data, the pressure calculation could be effected by as much as $(0.4\text{m/s}/1200^{0.5}) \cdot 420\text{Pa} \cdot \text{s/m} = 4.8\text{Pa}$ which is approximately 107 dB referenced to 20 μPa. Although this is not an exact treatment of the uncertainty, it demonstrates that the uncertainty in the PIV data is on the order of the broadband levels in the calculated pressure spectra. This creates a kind of background noise floor for the estimated pressure spectra which would have a larger effect at the lower Mach numbers when the overall magnitudes of the pressure fluctuations are smaller than the higher Mach numbers.

In some instances, the estimated pressure exhibits a peak in the spectra that is absent in that of the measured pressure or vice versa. There is no clear explanation for this phenomenon at this time. However, it is possibly the result of the estimated pressure fluctuations being completely dependent on the velocity field without taking into account the effects of the cavity acoustics, scattering, or other similar factors which are known to be important in this type of problem. Nevertheless, the analysis still shows a clear distinction between the features of the linear and non-linear sources for the pressure loads. Most importantly, the results demonstrate that the mean-shear or linear contribution to the pressure fluctuations carries the resonant features of the measured pressure loads. The non-linear contribution is primarily broadband in nature and does not exhibit any of the dominant Rossiter mode features. In most cases, the mean-shear contribution even matches the magnitudes of the peaks in the measured spectra. Even at Mach 0.19, where a resonance does not clearly present itself, the mean-shear contributions matches the broad rise in energy at the lower frequencies below 1500 Hz. Therefore, the resonant features of the cavity are reflected predominately in the mean-shear contribution from Poisson's equation. These results suggest that a successful cavity resonance control strategy would modify the mean-shear characteristics of the shear-layer. This is in agreement with the host of leading edge devices used in either a passive or active sense to control cavity flows that have been studied by many authors as reviewed by Rowley & Williams(). The fact that the turbulence-interaction features of the shear-layer are not associated with the cavity resonance may help determine why some control strategies function more favorably than others.

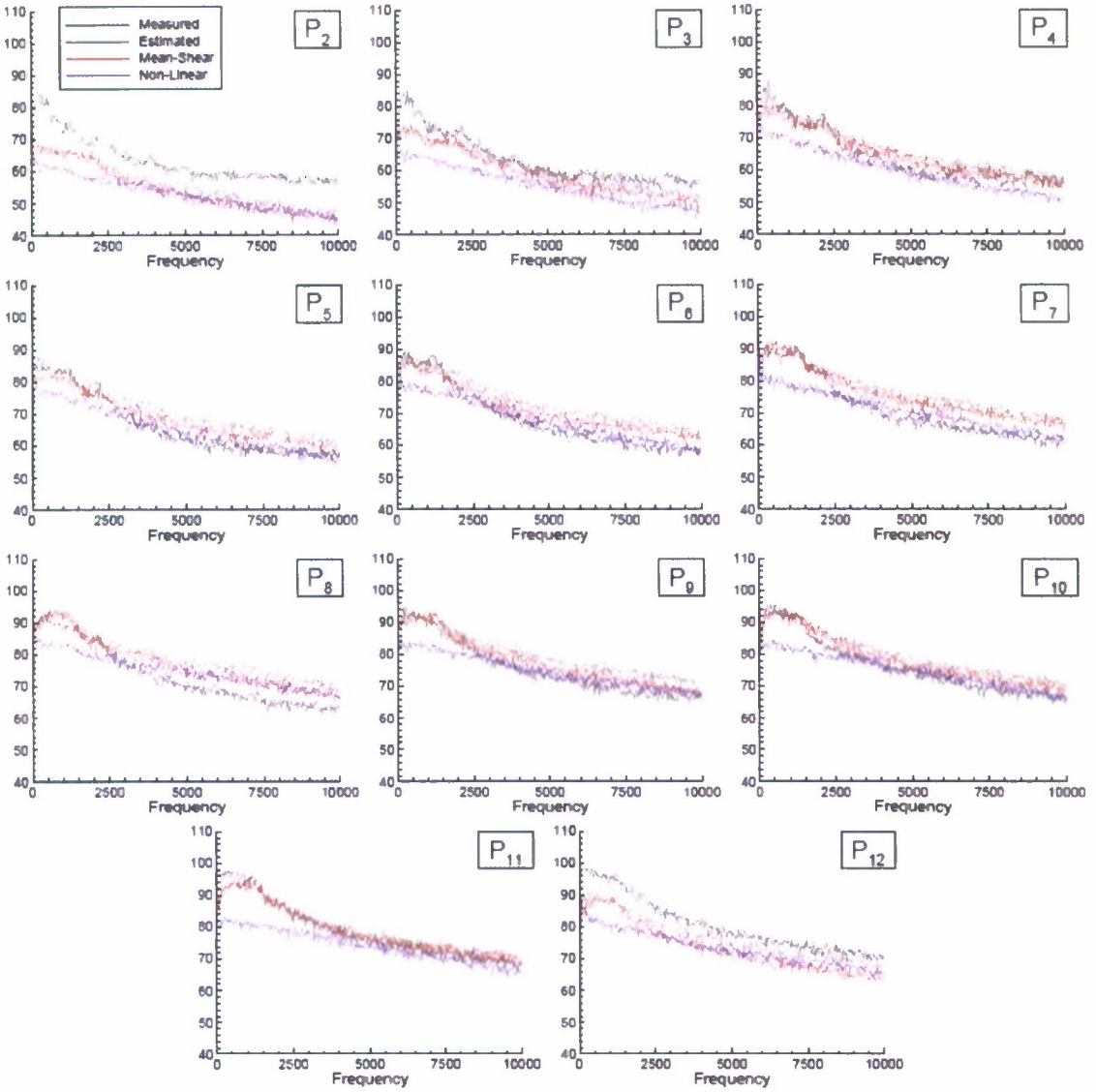

Figure 11: Auto-spectral density of the 11 floor mounted pressure measurements compared to the estimation results and the contributions from the mean-shear and non-linear components for Mach 0.19. Pressure measurement location, P_k, refers to the location along the cavity floor. Magnitude is dB/Hz referenced to 20 μPa.

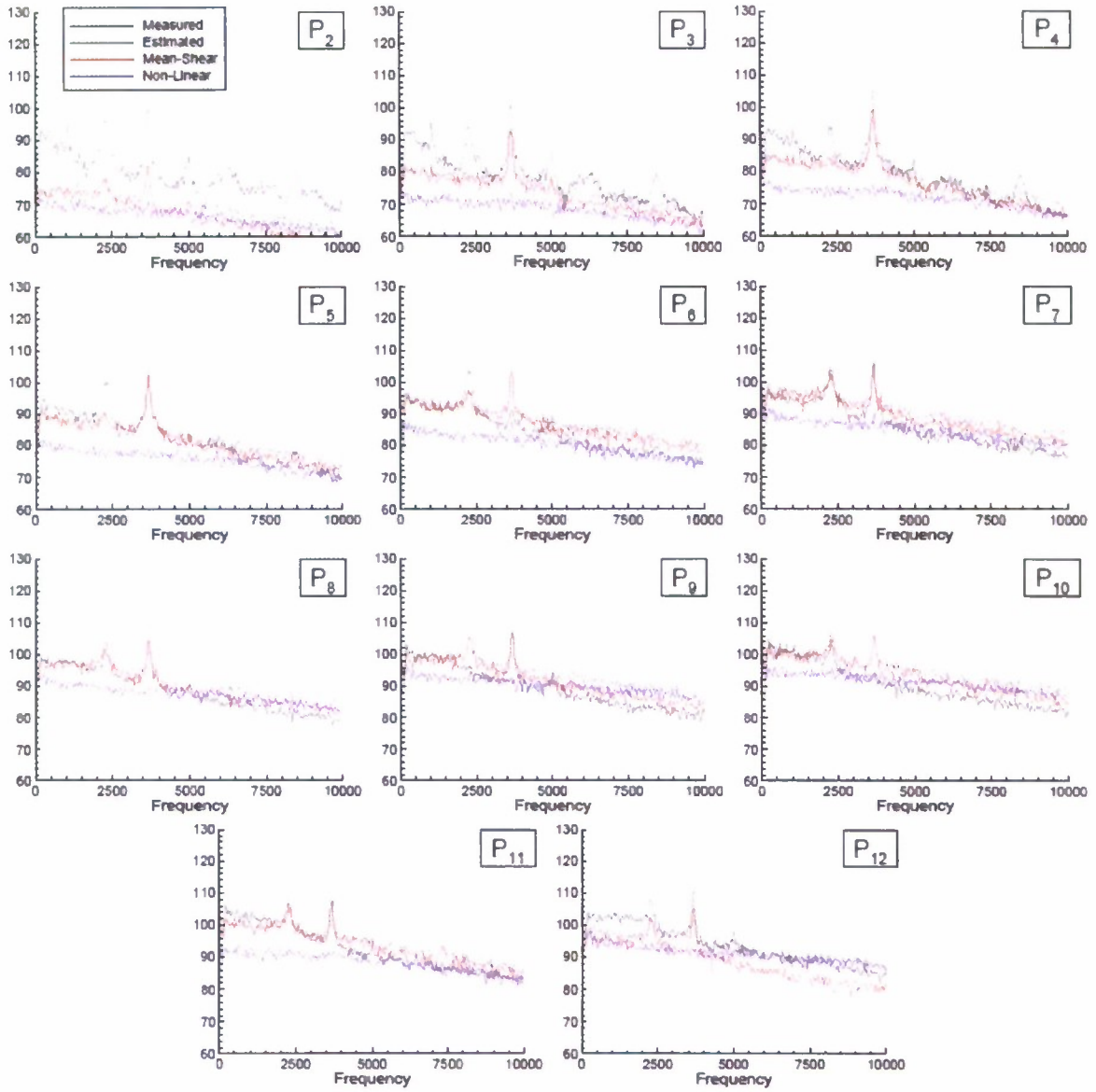

Figure 12: Auto-spectral density of the 11 floor mounted pressure measurements compared to the estimation results and the contributions from the mean-shear and non-linear components for Mach 0.39. Pressure measurement location, P_k, refers to the location along the cavity floor. Magnitude is dB/Hz referenced to 20 μPa.

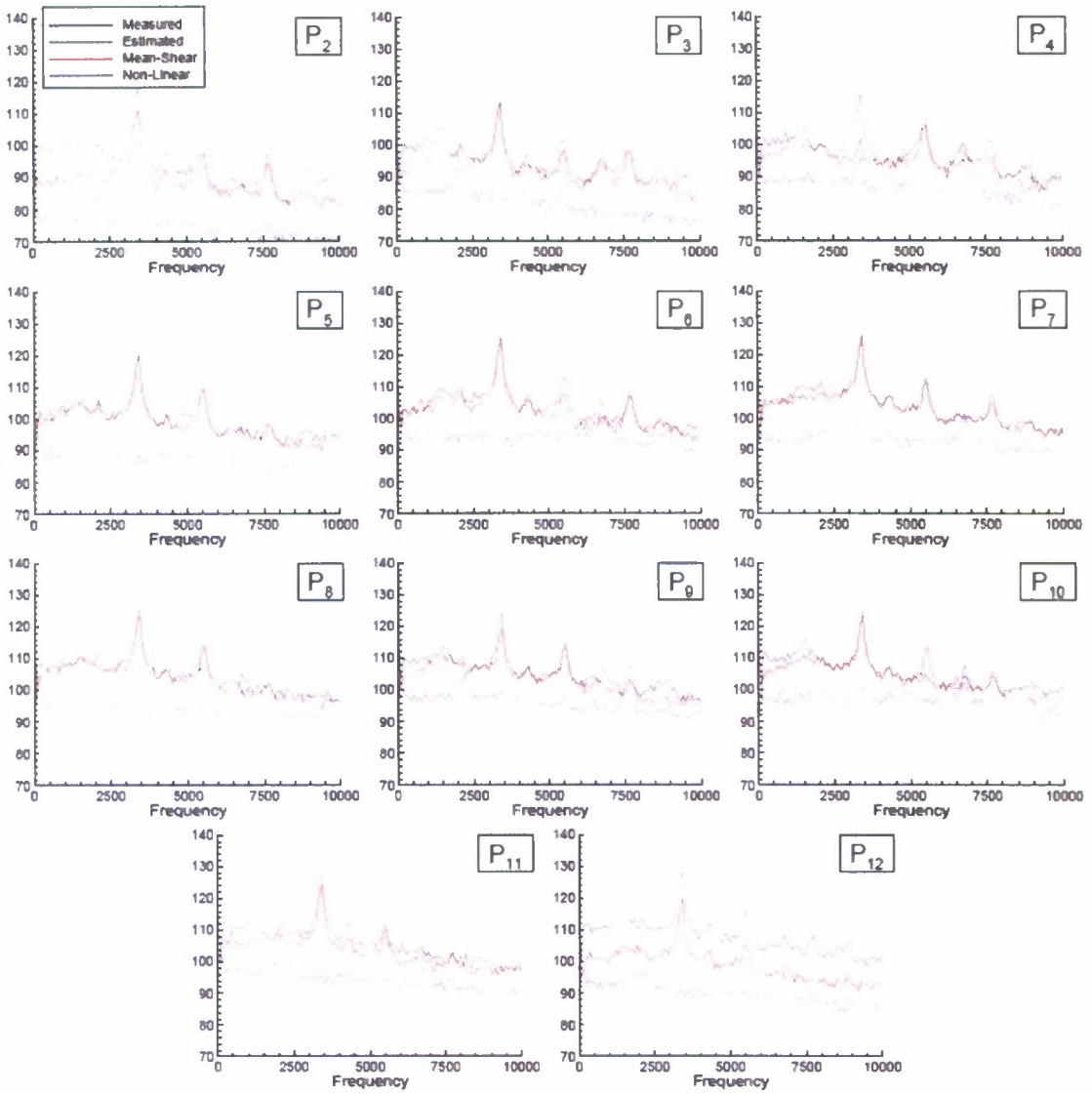

Figure 13: Auto-spectral density of the 11 floor mounted pressure measurements compared to the estimation results and the contributions from the mean-shear and non-linear components for Mach 0.73. Pressure measurement location, P_k, refers to the location along the cavity floor. Magnitude is dB/Hz referenced to 20 μPa.

3 Flow Physics of Successfully Controlled Cavity Flow

In the following seetion we will eompare various aspeets of the veloeity field for a sueeessfully eontrolled eavity flow. The data sets being used for this applieation is from a 3-dimensionsional eavity geometry sitting in a Maeh 1.5 flow. The eontrol eame from an array of miero-jets distributed at the leading edge of the eavity. These data sets are both numerieal and experimental. The experimental data set was aequired by Prof. Farrukh Alvi and his students at Florida State University. While the numerieal data set was generated by Dr. Srinivasan Arunajatesan at Combustion Researeh and Flow Teehnologies using their one equation Large Eddy Simulation model. In what follows we will only eoneentrate on eomparing the flow eharacteristies between the baseline (no eontrol) and the ease where the floe eontrol resulted in the maximum reduetion of fluetuating surfaee pressure. The details of the experiments, numeries and the effieaey of the eontrol on the surfaee pressure ean be found in Arunajatesan et al (2009), Ukeiley et al, (2008) and Sheehan (2007). It should be noted that work being presented in this this seetion was part of eollaboration between this AFOSR program with other programs at AFRL/RBAI

3.1 Cavity and Actuation Description

The analysis being presented in this seetion is for a nominal length to depth ratio 5.6 eavity whieh was three dimensional in nature with slanted side walls and a sloping floor. A sehematic of the eavity is shown in Figure 14.

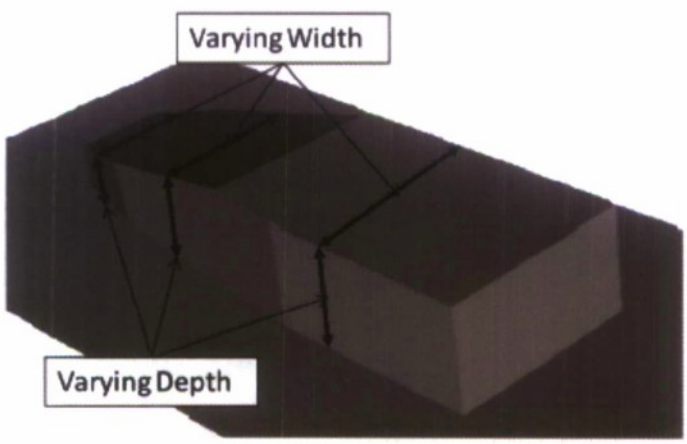

Figure 14: Sehematie of thc nonrectangular eavity being studied in thepresent work.

The aetuation eonsisted eight 400 μm mierojets whieh were loeated just upstream of the eavity leading edge at a distanee of four mierojet diameters from the leading edge. The spacing between the mierojets matehes that in the experimental work at FSU presented in Ukeiley et al (2008) and Sheehan (2007), which was parametrically optimized. A schematie of the orientation and loeation of the mierojets ean be seen in Figure 15. The mierojet pressures are 40 psig and

are operated choked. These conditions correspond to the conditions where the microjets' effectiveness started to saturate.

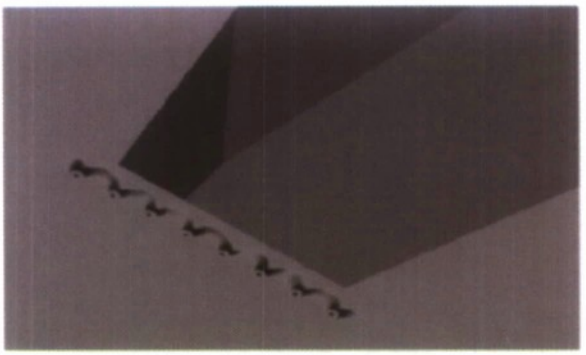

Figure 15: Schematic of the microjet actuators.

The effects of the control on the root mean square surface pressure fluctuations are presented in Figure 16 for both the experiments and the numerical simulations. Clearly there is a significant reduction in the fluctuating surface pressure for cases. It also should be noted even though there are some differences between the numerical and experimental results (~10%) they both show approximately the same levels of reduction. Additional it was demonstrated in the Ukeiley et al (2008) and Arunajatesan et al (2009) that there were reductions in both the tonal and broad band features of the fluctuating surface pressure spectra.

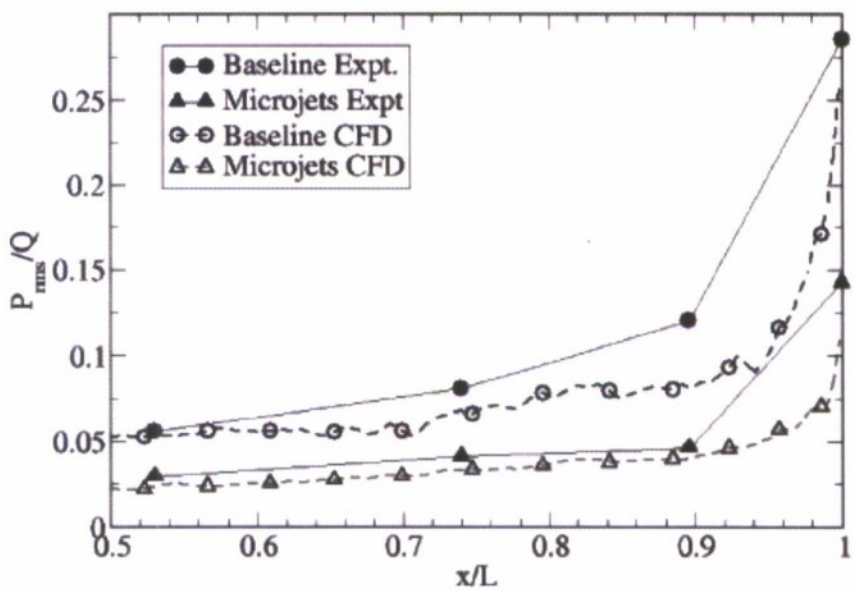

Figure 16: Reductions of root mean square surface pressure fluctuations for both experimental and numerical data sets.

3.2 Mean and Turbulent Flow Fields

Figure 17 displays contours of the mean flow for both the control and no control cases for both the streamwise and wall-normal components. From this figure one can see substantial changes in the flow patterns within the cavity. Examining the streamwise component one clearly observes that the shear layer is lifted and it does not appear to have as significant an impact with the aft wall. The artifact of this lifting of the shear layer can be seen by examining the wall-normal velocity where there is clearly less of downward velocity on the aft wall.

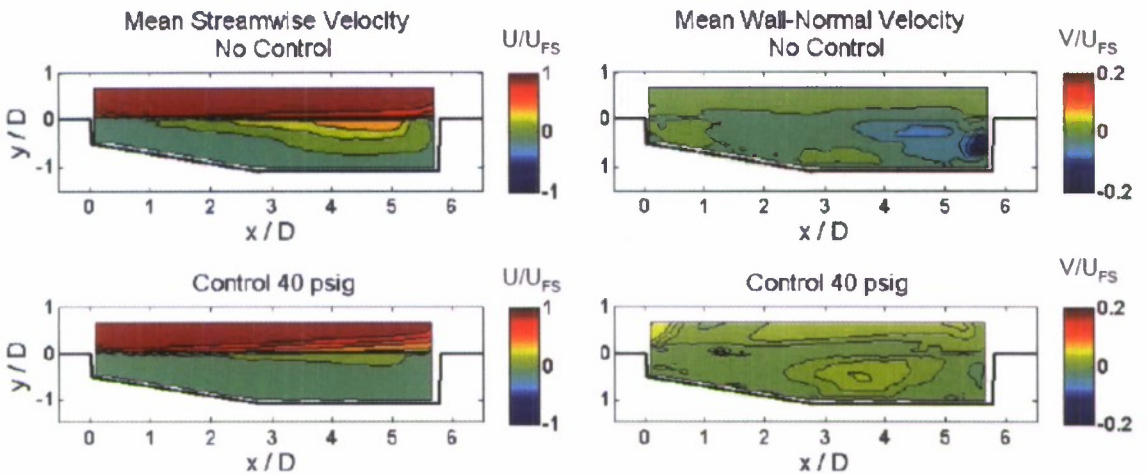

Figure 17: Mean flow velocity contours demonstrating the effects of the leading edge microjets.

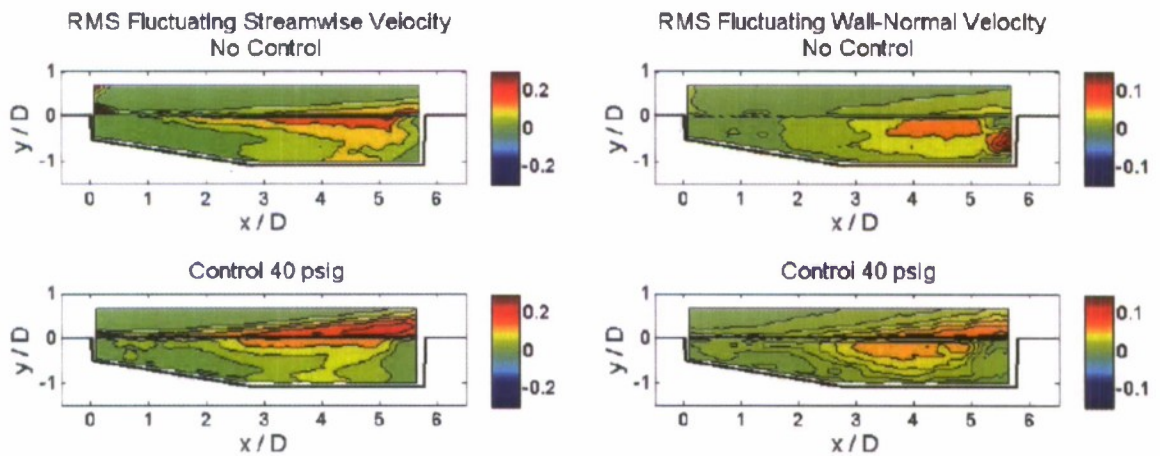

Figure 18: RMS flow velocity contours demonstrating the effects of the leading edge microjets.

Figure 18 displays the contours of the root mean square of the fluctuating velocities for both the controlled and no control scenarios. Once again the lofting of the shear layer is apparent

from studying where the peak levels in the streamwise component reside. Also apparent from these figures is that the shear layer for the controlled case thickens quite a bit more than the uncontrolled case in the initial part of its development. From examination of the wall-normal rms contours there is a reduction in the size of the unsteady region at the aft end of the cavity. Additionally, there is a lifting of the most intense fluctuations out of the cavity. Although not presented above the observations from the numerical simulations were quite similar although the effects on the fluctuating velocity were not as substantial.

3.3 Proper Orthogonal Decomposition

An application of the Proper Orthogonal Decomposition was carried out on both the experimental and numerical data sets discussed above. Results for the baseline cavity are compared with the microjet control cases, as these were the only cases where experimental flowfield data is available. The snapshot method (Sirovich, 1987) was used to extract the POD modes from the flowfield solution due to its computational efficiency with highly spatially resolved data. The analysis discussed first only uses the velocity data from the cavity midplane. The kinetic energy norm comprising only of u and v (neglecting w) is used to compare with the modes obtained from PIV on a similar plane from the experimental data.

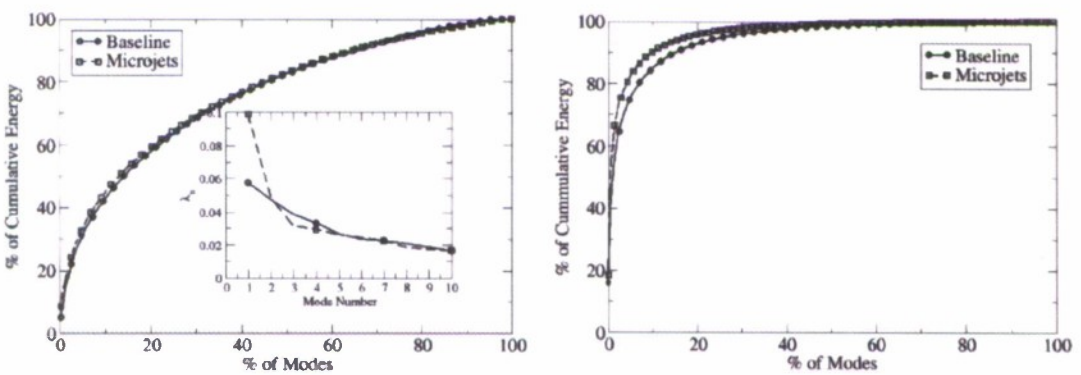

Figure 19: Comparsion of POD modes with and without control.

The convergence of the energy in the POD modes for both the numerical and experimental data sets for both the baseline and controlled cases is presented in Figure 19. An interesting observation from these plots is that, contrary to expectations, the convergence of the control case is better than the baseline case. There is more energy in the first mode, which has typically been interpreted to imply an increase in large-scale organization of the flow. As has been discussed here and elsewhere (Arunajatesan, 2006), the use of microjets leads to a reduction in the flow structure coherence. This behavior of the modes is also observed experimentally, as shown in Figure 19b where the POD modes for the experimental data set also show that the amount of energy in the first mode is larger for the controlled flow for the baseline even though these modes contain a higher percentage of the overall energy. However, one must be careful in

interpreting these results, as it will be demonstrated later that neglecting the w in the norm has led to this contrary result, and a full 3-D POD may be required.

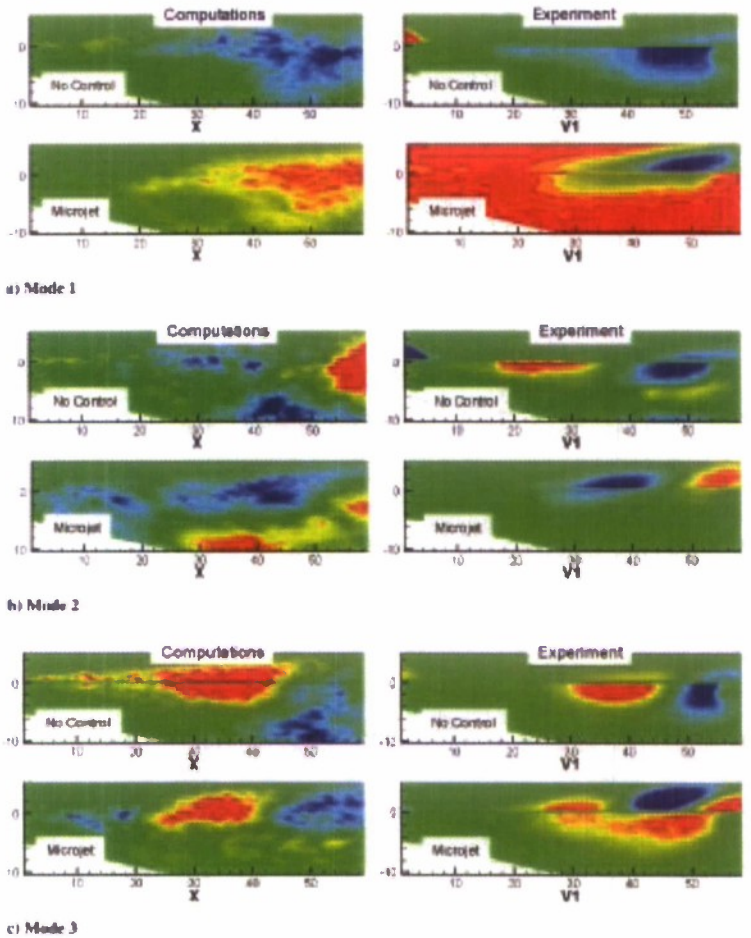

Figure 20: Comparison of streamwise POD modes of baseline vs. control cases.

A comparison of the first three POD modes of the streamwise component from both the experiment and simulation results is presented in Figure 20. In general, the experimentally and numerically extracted POD modes show agreement with the differences in spatial resolution being quite apparent though. For the first mode the effect of control is to loft the shear layer slightly over the cavity, as is shown qualitatively by both the simulation and experiment. However, the effect is more pronounced in the experiment. The second and third modes are qualitatively similar with the third mode representing the dominant wavelength of structures that is very similar to that in the experiment. Further, the modes with and without control appear to be more or less similar in nature except in the close proximity to the leading edge of the cavity where the control concept is applied. This inference reinforces the earlier results about the turbulence field being only slightly different for most of the cavity except near the leading edge.

In an attempt to more quantitatively assess the similarity of the POD modes the similarity function (Rempfer et al, 1994) was calculated for the experimentally determined POD modes and is presented in Figure 21. This function uses the fact that the POD modes are orthonormal hence

the inner product of two modes which are the same would be one. In Figure 21 the inner product of the first 20 modes from the baseline (no control) case are taken with the first 20 modes from the controlled case. In the plot (based on the color code in the legend) square which are blue represent mode combinations where the inner product is small and the modes are not similar. On the contrary squares which are red represent values of the inner product is approaching one and hence these mode combinations represent modes which are similar for both the controlled and baseline cases. An example of on such combination is the fourth mode from the controlled flow and the seventh mode from the baseline. The end goal of studying this will be to identify key flow features that exist in both the baseline and controlled cases so more intelligent control can be developed in the future to push the flow to one dominated by these features.

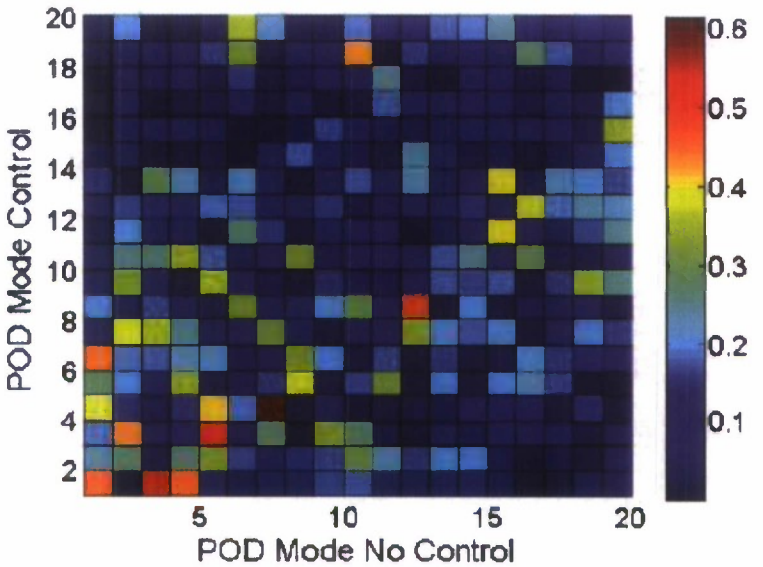

Figure 21: Similarity function from experimental POD modes demonstrating similarities in the modes from the controlled and baseline cases.

4 Closed-Loop Active Control Studies

In this seetion we will present results from and applieation of elosed loop adaptive eontrol to a resonating eavity flow. While the applieation is admittedly at a lower Mach number the methodologies developed here are can be utilized at higher free stream Mach numbers if actuators with enough authority can be developed. This eontrolled flow will serve as base flow in follow on studies for us to develop a bctter understanding of what the eontrol, which is based on reducing the surfaee pressure fluetuations, does to the flow.

In this ehapter, first, a fccdbaek control methodology is developed for reducing thc flow-indueed eavity oseillation and broadband pressure fluctuations. Then, an aetive flow control aetuator is designed and investigated. Finally, adaptive system ID and eontrol algorithms are eombined and implemented in real-timc to achieve the flow control. In order to aehieve the objeetives, a MIMO system ID algorithm are derived and discussed first. Then, the MIMO adaptive GPC algorithm is deseribed. This is followed by a description of the wind tunnel faeilities and the data processing methods. Wind tunnel experimental results for both open-loop (baseline) and elosed-loop are then presented and diseussed. Finally, the eonelusions and future work arc presented.

4.1 System Identification Algorithm

In this seetion, a MIMO system ID algorithm is developed. A linear system model is summed with the r inputs $[u]_{r\times 1}$ and the m outputs $[y]_{m\times 1}$. For simplifieation, the order p of thc feedbaek loop is assumed the same as the order of the forward path. At speeifie time indcx k, the system can be cxpressed as

$$\begin{aligned} \boldsymbol{y}(k) &= \boldsymbol{\alpha}_1 \boldsymbol{y}(k-1) + \boldsymbol{\alpha}_2 \boldsymbol{y}(k-2) + \cdots + \boldsymbol{\alpha}_p \boldsymbol{y}(k-p) \\ &\quad + \boldsymbol{\beta}_0 \boldsymbol{u}(k) + \boldsymbol{\beta}_1 \boldsymbol{u}(k-1) + \boldsymbol{\beta}_2 \boldsymbol{u}(k-2) + \cdots + \boldsymbol{\beta}_p \boldsymbol{u}(k-p) \end{aligned} \tag{4.1}$$

Where

$$\boldsymbol{u}(k) = [u(k)]_{r\times 1} = \begin{bmatrix} u_1(k) \\ u_2(k) \\ \vdots \\ u_r(k) \end{bmatrix}_{r\times 1}, \boldsymbol{y}(k) = [y(k)]_{m\times 1} = \begin{bmatrix} y_1(k) \\ y_2(k) \\ \vdots \\ y_m(k) \end{bmatrix}_{m\times 1} \tag{4.2}$$

$$\begin{cases} \boldsymbol{\alpha}_1 = [\alpha_1]_{m\times m}, \boldsymbol{\alpha}_2 = [\alpha_2]_{m\times m}, \cdots, \boldsymbol{\alpha}_p = [\alpha_p]_{m\times m} \\ \boldsymbol{\beta}_0 = [\beta_0]_{m\times r}, \boldsymbol{\beta}_1 = [\beta_1]_{m\times r}, \cdots, \boldsymbol{\beta}_p = [\beta_p]_{m\times r} \end{cases}$$

Define the observer Markov parameters

$$\boldsymbol{\theta}(k) = \left[\boldsymbol{\alpha}_1 \quad \cdots \quad \boldsymbol{\alpha}_p \mid \boldsymbol{\beta}_0 \quad \cdots \quad \boldsymbol{\beta}_p \right]_{m\times[m*p+r*(p+1)]} \tag{4.3}$$

and the regression vector

$$\boldsymbol{\varphi}(k)=\begin{bmatrix} y(k-1) \\ \vdots \\ y(k-p) \\ \hline u(k) \\ \vdots \\ u(k-p) \end{bmatrix}_{[m^*p+r^*(p+1)]\times 1} \tag{4.4}$$

substituting Equation 4.3 and Equation 4.2 into Equation 4.1 yields a matrix equation for the filter outputs

$$\left[\hat{y}(k)\right]_{m\times 1}=\left[\hat{\boldsymbol{\theta}}(k)\right]_{m\times[(m^*p+r^*(p+1))]}\left[\boldsymbol{\varphi}(k)\right]_{[(m^*p+r^*(p+1))]\times 1} \tag{4.5}$$

Furthermore, the errors are defined as

$$\left[\boldsymbol{\varepsilon}(k)\right]_{m\times 1}=\left[\hat{y}(k)\right]_{m\times 1}-\left[y(k)\right]_{m\times 1} \tag{4.6}$$

Finally, the observer Markov parameters 4.2 can be identified recursively by

$$\hat{\boldsymbol{\theta}}(k+1)=\hat{\boldsymbol{\theta}}(k)-\mu\boldsymbol{\varepsilon}(k)\boldsymbol{\varphi}^T(k) \tag{4.7}$$

In order to automatically update the step size, choose

$$\mu=\frac{1}{\sigma+\|\boldsymbol{\varphi}\|_2} \tag{4.8}$$

where σ is a small number to avoid the singularity when $\|\boldsymbol{\varphi}\|_2$ is zero.

GENERALIZED PREDICTIVE CONTROL ALGORIHTM

The generalized predictive control (GPC) algorithm belongs to a family of the most popular model predictive control (MPC). The MPC algorithm is a feedback control method, different choices of dynamic models, cost functions and constraints can generate different MPC algorithms. It was conceived near the end of the 1970s and has been widely used in industrial process control. The methodology of MPC is represented in Figure 22, where k is the time index number, u(k) are the input sequences, and y(k) are the actual output sequences. The $\hat{y}(k)$ and $y_r(k)$ are estimated output and reference signals, respectively.

Two comments are made here to describe all MPC algorithms. First, at each time step, a specific cost function is constructed by a series of future control signals up to u(k+s) and a series of future error signals, which are the differences between the estimated output signals $\hat{y}(k+j)$

and the reference signals $y_r(k+j)$. Second, a series of future inputs u(k+j) are calculated by minimizing this cost function, and only the first input signal is provided to the

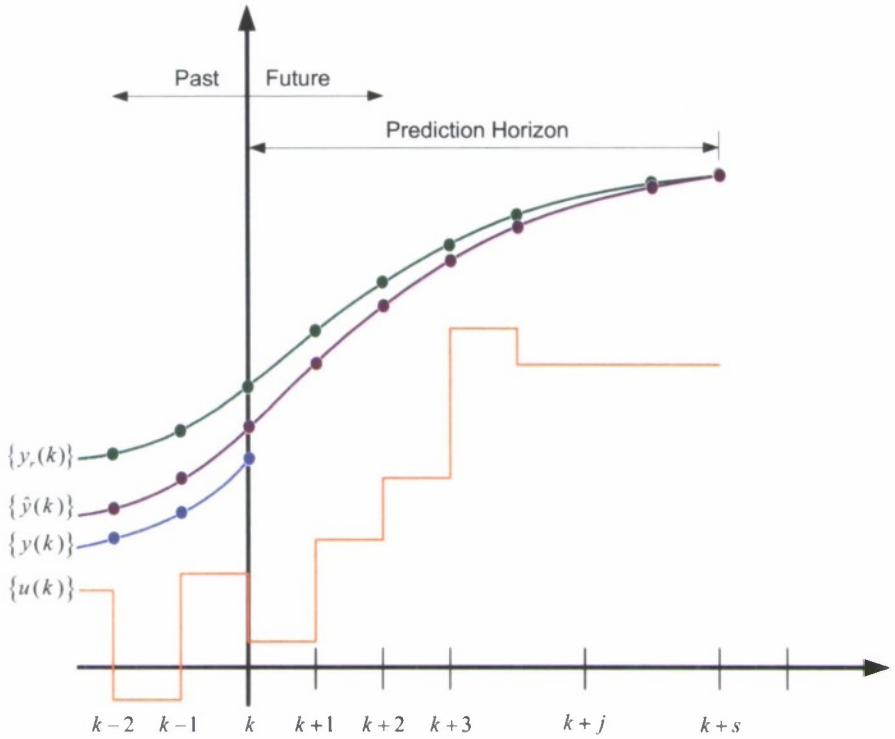

Figure 22: Model predictive control strategy.

system. At the next sampling interval, new values of the output signals are obtained, and the future control inputs are calculated again according to the new cost function. The same computations are repeated. Juang et al. (1997, 2001) give the derivation of the adaptive MIMO GPC algorithm. This algorithm is an effective control method for systems with problems of non-minimum phase, open loop unstable plants or lightly damped systems. It is also characterized by good control performance and high robustness. Furthermore, the GPC algorithm can deal with the multi-dimension case and can easily be combined with adaptive algorithms for self-tuning real-time applications. The problem of flow-induced open cavity oscillations exhibit several theses issues, therefore, the GPC is considered as a potential candidate controller.

Two modifications are made for this algorithm. First, a input weight matrix is integrated into the cost function, this control matrix can put the penalty for each control input signal and further to tune the performance for each input channels. Second, a recursive version of GPC is developed for real-time control application.

MIMO Adaptive GPC Model

In this section, a MIMO model with IIR structure is considered. A linear and time invariant system with r inputs $[u]_{r\times 1}$ and m outputs $[y]_{m\times 1}$, at the time index k can be expressed as

$$\begin{aligned} \boldsymbol{y}(k) &= \boldsymbol{\alpha}_1 \boldsymbol{y}(k-1) + \boldsymbol{\alpha}_2 \boldsymbol{y}(k-2) + \cdots + \boldsymbol{\alpha}_p \boldsymbol{y}(k-p) \\ &\quad + \boldsymbol{\beta}_0 \boldsymbol{u}(k) + \boldsymbol{\beta}_1 \boldsymbol{u}(k-1) + \boldsymbol{\beta}_2 \boldsymbol{u}(k-2) + \cdots + \boldsymbol{\beta}_p \boldsymbol{u}(k-p) \end{aligned} \tag{4.9}$$

where

$$\boldsymbol{u}(k) = \left[u(k)\right]_{r\times 1} = \begin{bmatrix} u_1(k) \\ u_2(k) \\ \vdots \\ u_r(k) \end{bmatrix}_{r\times 1}, \boldsymbol{y}(k) = \left[y(k)\right]_{m\times 1} = \begin{bmatrix} y_1(k) \\ y_2(k) \\ \vdots \\ y_m(k) \end{bmatrix}_{m\times 1} \tag{4.10}$$

$$\begin{cases} \boldsymbol{\alpha}_1 = \left[\alpha_1\right]_{m\times m}, \boldsymbol{\alpha}_2 = \left[\alpha_2\right]_{m\times m}, \cdots, \boldsymbol{\alpha}_p = \left[\alpha_p\right]_{m\times m} \\ \boldsymbol{\beta}_0 = \left[\beta_0\right]_{m\times r}, \boldsymbol{\beta}_1 = \left[\beta_1\right]_{m\times r}, \cdots, \boldsymbol{\beta}_p = \left[\beta_p\right]_{m\times r} \end{cases}$$

Shifting k step ahead from the Equation (4.9), the output vector y(k+j) can be derived as

$$\begin{aligned} \boldsymbol{y}(k+j) &= \boldsymbol{\alpha}_1^{(j)} \boldsymbol{y}(k-1) + \cdots + \boldsymbol{\alpha}_{p-1}^{(j)} \boldsymbol{y}(k-p+1) \\ &\quad + \boldsymbol{\alpha}_p^{(j)} \boldsymbol{y}(k-p) + \boldsymbol{\beta}_0 \boldsymbol{u}(k+j) + \boldsymbol{\beta}_0^{(1)} \boldsymbol{u}(k+j-1) + \cdots \\ &\quad + \boldsymbol{\beta}_0^{(j)} \boldsymbol{u}(k) + \boldsymbol{\beta}_1^{(j)} \boldsymbol{u}(k-1) + \cdots + \boldsymbol{\beta}_p^{(j)} \boldsymbol{u}(k-p) \end{aligned} \tag{4.11}$$

Where

$$\begin{cases} \left[\boldsymbol{\alpha}_1^{(j)}\right]_{m\times m} = \boldsymbol{\alpha}_1^{(j-1)} \boldsymbol{\alpha}_1 + \boldsymbol{\alpha}_2^{(j-1)} \\ \left[\boldsymbol{\alpha}_2^{(j)}\right]_{m\times m} = \boldsymbol{\alpha}_1^{(j-1)} \boldsymbol{\alpha}_2 + \boldsymbol{\alpha}_3^{(j-1)} \\ \vdots \\ \left[\boldsymbol{\alpha}_{p-1}^{(j)}\right]_{m\times m} = \boldsymbol{\alpha}_1^{(j-1)} \boldsymbol{\alpha}_{p-1} + \boldsymbol{\alpha}_p^{(j-1)} \\ \left[\boldsymbol{\alpha}_p^{(j)}\right]_{m\times m} = \boldsymbol{\alpha}_1^{(j-1)} \boldsymbol{\alpha}_p \end{cases}, \begin{cases} \left[\boldsymbol{\beta}_0^{(j)}\right]_{m\times r} = \left(\boldsymbol{\alpha}_1^{(j-1)} \boldsymbol{\beta}_0 + \boldsymbol{\beta}_1^{(j-1)}\right) \\ \left[\boldsymbol{\beta}_1^{(j)}\right]_{m\times r} = \left(\boldsymbol{\alpha}_1^{(j-1)} \boldsymbol{\beta}_1 + \boldsymbol{\beta}_2^{(j-1)}\right) \\ \vdots \\ \left[\boldsymbol{\beta}_{p-1}^{(j)}\right]_{m\times r} = \left(\boldsymbol{\alpha}_1^{(j-1)} \boldsymbol{\beta}_{p-1} + \boldsymbol{\beta}_p^{(j-1)}\right) \\ \left[\boldsymbol{\beta}_p^{(j)}\right]_{m\times r} = \boldsymbol{\alpha}_1^{(j-1)} \boldsymbol{\beta}_p \end{cases} \tag{4.12}$$

and with initial

$$\begin{cases} \left[\boldsymbol{\alpha}_1^{(0)}\right]_{m\times m} = \boldsymbol{\alpha}_1 \\ \left[\boldsymbol{\alpha}_2^{(0)}\right]_{m\times m} = \boldsymbol{\alpha}_2 \\ \vdots \\ \left[\boldsymbol{\alpha}_{p-1}^{(0)}\right]_{m\times m} = \boldsymbol{\alpha}_{p-1} \\ \left[\boldsymbol{\alpha}_p^{(0)}\right]_{m\times m} = \boldsymbol{\alpha}_p \end{cases}, \begin{cases} \left[\boldsymbol{\beta}_0^{(0)}\right]_{m\times r} = \boldsymbol{\beta}_0 \\ \left[\boldsymbol{\beta}_1^{(0)}\right]_{m\times r} = \boldsymbol{\beta}_1 \\ \vdots \\ \left[\boldsymbol{\beta}_{p-1}^{(0)}\right]_{m\times r} = \boldsymbol{\beta}_{p-1} \\ \left[\boldsymbol{\beta}_p^{(0)}\right]_{m\times r} = \boldsymbol{\beta}_p \end{cases} \tag{4.13}$$

The quantities $\boldsymbol{\beta}_0^{(k)}$ (k=0,1,…) are the impulse response sequence of the system. Defining the following the vector form

$$\boldsymbol{u}_p(k-p) = \begin{pmatrix} u(k-p) \\ u(k-p+1) \\ \vdots \\ u(k-1) \end{pmatrix}_{(r*p)\times 1}, \boldsymbol{u}_{j+1}(k) = \begin{pmatrix} u(k) \\ u(k+1) \\ \vdots \\ u(k+j) \end{pmatrix}_{(r*(j+1))\times 1}$$
$$\boldsymbol{y}_p(k-p) = \begin{pmatrix} y(k-p) \\ y(k-p+1) \\ \vdots \\ y(k-1) \end{pmatrix}_{(m*p)\times 1} \tag{4.14}$$

the predictive index j=0,1,2,…,q,q+1,…,s-1, , and

$$\boldsymbol{u}_s(k) = \begin{pmatrix} u(k) \\ u(k+1) \\ \vdots \\ u(k+s-1) \end{pmatrix}_{(r*s)\times 1}, \boldsymbol{y}_s(k) = \begin{pmatrix} y(k) \\ y(k+1) \\ \vdots \\ y(k+s-1) \end{pmatrix}_{(m*s)\times 1} \tag{4.15}$$

Finally, the predictive model for future outputs, $\mathbf{y}_s$, is obtained, this future outputs consists of a weighted summation of future inputs, $\mathbf{u}_s$, previous inputs, $\mathbf{u}_p$, and previous outputs, $\mathbf{y}_p$

$$\boldsymbol{y}_s(k) = \boldsymbol{T}\boldsymbol{u}_s(k) + \boldsymbol{B}\boldsymbol{u}_p(k-p) + \boldsymbol{A}\boldsymbol{y}_p(k-p) \tag{4.16}$$

where

$$\boldsymbol{T} = \begin{bmatrix} \boldsymbol{\beta}_0 & 0 & \cdots & 0 \\ \boldsymbol{\beta}_0^{(1)} & \boldsymbol{\beta}_0 & \cdots & 0 \\ \vdots & \vdots & \ddots & \vdots \\ \boldsymbol{\beta}_0^{(s-1)} & \boldsymbol{\beta}_0^{(s-2)} & \cdots & \boldsymbol{\beta}_0 \end{bmatrix}_{(m*s)\times(r*s)} \tag{4.17}$$

$$\boldsymbol{B}=\begin{bmatrix} \boldsymbol{\beta}_p & \boldsymbol{\beta}_{p-1} & \cdots & \boldsymbol{\beta}_1 \\ \boldsymbol{\beta}_p^{(1)} & \boldsymbol{\beta}_{p-1}^{(1)} & \cdots & \boldsymbol{\beta}_1^{(1)} \\ \vdots & \vdots & \ddots & \vdots \\ \boldsymbol{\beta}_p^{(s-1)} & \boldsymbol{\beta}_{p-1}^{(s-1)} & \cdots & \boldsymbol{\beta}_1^{(s-1)} \end{bmatrix}_{(m*s)\times(r*p)} \tag{4.18}$$

$$\boldsymbol{A}=\begin{bmatrix} \boldsymbol{\alpha}_p & \boldsymbol{\alpha}_{p-1} & \cdots & \boldsymbol{\alpha}_1 \\ \boldsymbol{\alpha}_p^{(1)} & \boldsymbol{\alpha}_{p-1}^{(1)} & \cdots & \boldsymbol{\alpha}_1^{(1)} \\ \vdots & \vdots & \ddots & \vdots \\ \boldsymbol{\alpha}_p^{(s-1)} & \boldsymbol{\alpha}_{p-1}^{(s-1)} & \cdots & \boldsymbol{\alpha}_1^{(s-1)} \end{bmatrix}_{(m*s)\times(m*p)} \tag{4.19}$$

MIMO Adaptive GPC Cost Function

Assume the control inputs (present input and future inputs) depend on the previous inputs and output and can be expressed as

$$\left[\boldsymbol{u}_s(k)\right]_{(s*r)\times 1}=\left[\boldsymbol{H}\right]_{(s*r)\times[p*(m+r)]}\begin{bmatrix} \boldsymbol{u}_p(k-p) \\ \boldsymbol{y}_p(k-p) \end{bmatrix}_{[p*(m+r)]\times 1} \tag{4.20}$$

Two potential cost functions are list below. The first one consists terms of future outputs and a trace of the feedback gain matrix

$$J(k)=\boldsymbol{y}_s^{\,T}(k)\boldsymbol{Q}\boldsymbol{y}_s(k)+\gamma\cdot tr\left(\boldsymbol{H}^T\boldsymbol{H}\right) \tag{4.21}$$

and the second definition of cost function based on the total energy of future outputs as well as the inputs

$$J(k)=\frac{1}{2}\left(\boldsymbol{y}_s^{\,T}(k)\boldsymbol{Q}\boldsymbol{y}_s(k)+\boldsymbol{u}_s^{\,T}(k)\boldsymbol{R}\boldsymbol{u}_s(k)\right) \tag{4.22}$$

The output weight matrix $\boldsymbol{Q}$, input weight matrix $\boldsymbol{R}$ and the control horizon s are important parameters for tuning the controller. The horizon s is usually chosen to be several times longer than the rise time of the plant in order to ensure a stable feedback controller (Gibbs et al. 2004). Also, if the predict horizon range is from zero to infinity, the resulting controller approaches the steady-state linear quadratic regulator (Phan et al. 1998).

MIMO Adaptive GPC Law

In order to minimize the cost function, three approaches are considered as follows.

- Based on Equation (4.21), the control coefficients can be update using adaptive gradient algorithm.
- Based on Equation (4.22), the optimum solution can be derived. However, this method requires the calculation of a matrix inverse, so the computational complex is higher.
- Based on Equation (4.22), the control coefficients can be updated using an adaptive gradient algorithm.

The first approach is examined by Kegerise et al. (2004). In the next section, the latter two approaches are derived.

MIMO Adaptive GPC Optimum Solution

Based on the cost function (4.22), the goal is to find $[H]_{(s^*r)\times[p^*(m+r)]}$ or $[u_s(k)]_{(s^*r)\times 1}$ to minimize the cost function. We will show that both minimizing the cost function (4.22) with respect to control matrix $[H]_{(s^*r)\times[p^*(m+r)]}$ and input vector $[u_s(k)]_{(s^*r)\times 1}$ will provide the same result. To simplify the expression, let's define

$$[v_p]_{[p^*(m+r)]\times 1} = \begin{bmatrix} u_p(k-p) \\ y_p(k-p) \end{bmatrix}_{[p^*(m+r)]\times 1} \tag{4.24}$$

with some algebraic manipulation, the optimum solution is obtained

$$u_s|_{opt} = -\left(T^T Q T + R\right)^{-1} T^T Q [B \quad A][v_p] \tag{4.24}$$

It is easy to apply the optimal solution of the Equation (4.24) on the cavity problem. However, the matrix inversion calculation has high computational complexity. Only if the model order is low enough, the optimal input can be used in real-time application.

MIMO Adaptive GPC Recursive Solution

To avoid calculating the inverse of the matrix in Equation (4.24), the stochastic gradient descend method can be used to update the control matrix H using the following algorithm

$$H(k+1) = H(k) - \mu \frac{\partial J(k)}{\partial H(k)} \tag{4.25}$$

therefore, the recursive solution is given by

$$H(k+1) = H(k) - \mu \left\{ \left(T^T Q T + R\right) H(k) + T^T Q [B \quad A] \right\} [v_p][v_p]^T \tag{4.26}$$

Since only present r controls $[u(k)]_{rx1}$ are applied to the system, only the first r rows in Equation (4.26) are used

$$[h(k+1)] = [h(k)] - \mu \underbrace{\left\{ \left(T^T Q T + R\right)[H(k)] + T^T Q [B \quad A] \right\}}_{\text{first r rows}} [v_p][v_p]^T \tag{4.27}$$

The output weight matrix Q, input weight matrix R and the control horizon s are tuning for testing their effects to the control performance.

4.2 Wind Tunnel Experiment and Setup

The experimental facilities and instruments used in this study are described in detail in this section. These devices consist of a blowdown wind tunnel with a test section and cavity model, unsteady pressure transducers, data acquisition systems, and a DSP real-time control system. Actuator system used in this study is described also in this section.

Wind Tunnel Facility

The compressible flow control experiments are conducted in the University of Florida Experimental Fluid Dynamics Laboratory. A schematic of the supply portion of the compressible flow facility is shown in Figure 23. This facility is a pressure-driven blowdown wind tunnel, which allows for control of the upstream stagnation pressure but without temperature control.

The compressed air is generated by a Quincy screw compressor (250 psi maximum pressure, Model 5C447TTDN7039BB). A desiccant dryer (ZEKS Model 730HPS90MG) is used to remove the moisture and residual oil in the compressed air. The flow conditioning is accomplished first by a settling chamber. The stagnation chamber consists of a 254 mm

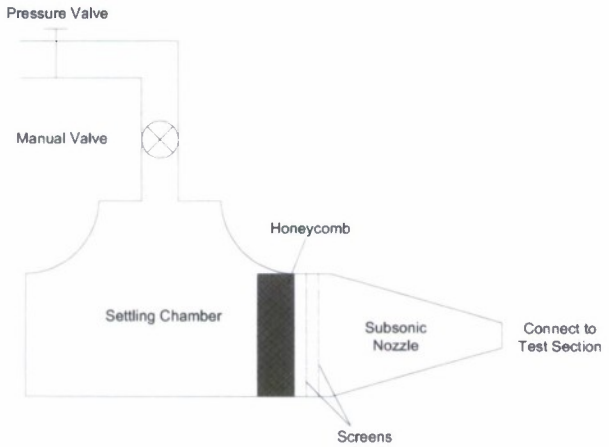

Figure 23: Schematic of the wind tunnel facility.

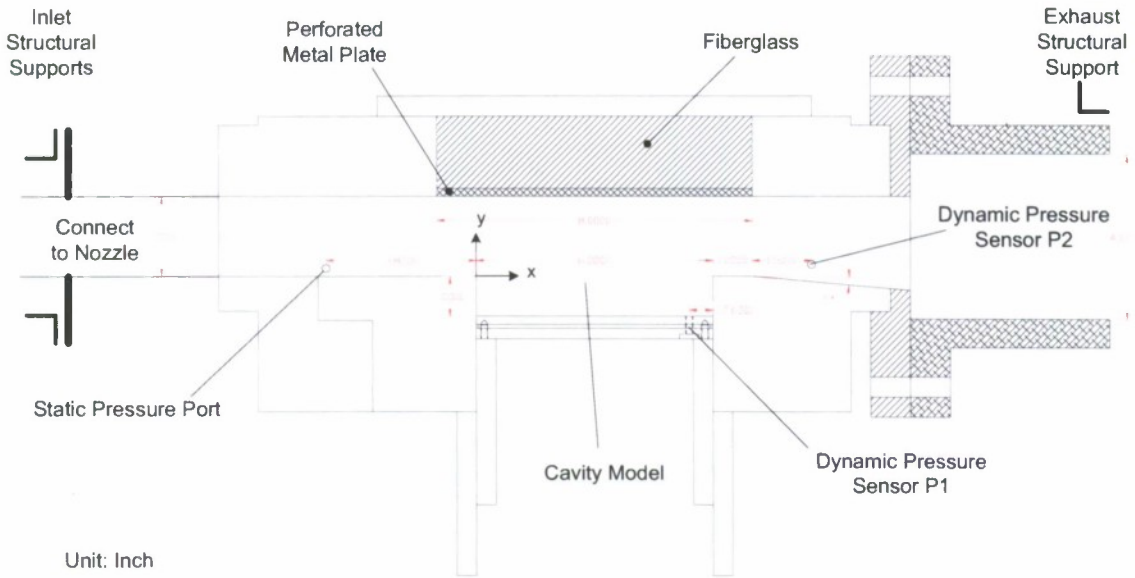

Figure 24: Schematic of the test section and the cavity model. Dimensions are inches.

diameter cast iron pipe supplied with the clean, dry compressed air. A computer controlled control valve (Fischer Controls with body type ET and Acuator Type 667) is situated approximately 6 meters upstream of the stagnation chamber with a 76.2 mm diameter pipe connecting the two. A flexible rubber coupler is located at the entrance of to the stagnation chamber to minimize transmitted vibrations from the supply line. The stagnation chamber is mounted on rubber vibration isolation mounts. A honeycomb and two flow screens are located at the exit of the settling chamber and the start of the contraction section, respectively. The honeycomb is 76.2 mm in width (the cell is 76.2 mm long) with a cell size of 0.35 mm. Two anti-turbulence screens spaced 25.4 mm apart are used; these screens have 62% open area and use 0.1 mm diameter stainless steel wire. For the current experiment, the facility was fitted with a subsonic nozzle that transitions from the 254 mm diameter circular cross-section to a 50.8 mm x 50.8 mm square cross-section linearly over a distance of 355.6 mm. The profile designed for this contraction found in previous work provides good flow quality downstream of the contraction (Carroll et al. 2004). The overall area contraction ratio from the settling chamber to the test section is 19.6:1. For the present subsonic setup, the freestream Mach number can be altered from approximately 0.1 to 0.7, and the facility run times are approximately 10 minutes at the maximum flow rate due to the limited size of the two storage tanks, each with volume of 3800 gallons.

Test Section and Cavity Model

A schematic of the test section with an integrated cavity model is shown in Figure 24. The origin of the Cartesian coordinate system is situated at the leading edge of the cavity in the mid-plane. The test section connects the subsonic nozzle exit and the exhaust pipe with 431.8 mm long duct with a 50.8 mm x 50.8 mm square cross section.

The eavity model is eontained inside this duct and is a canonical rectangular eavity with a fixed length of L=152.4 mm and width of W=50.8 mm and is installed along the floor of the test seetion. The depth of the eavity model, D, can be adjusted continuously from 0 to 50.8 mm. This meehanism provides a range of cavity length-to-depth ratios, L/D, from 3 to infinity. The cavity model spans thc width of thc tcst scction W. However, a small cavity width is not desirable, beeausc the side wall boundary layer growth introduces three-dimensional effects in thc aft region of the cavity. As a result, the growth of thc sidewall boundary layers in the test seetion may result in modest flow acccleration. The boundary layers have not been characterized in this study. Nevertheless, the eavity geometry applied in this study is eonsistent with previous efforts in the literature (Kegerise et al. 2007a,b) eonsidered to bc shallow and narrow, so two-dimensional longitudinal modes will be dominant (Heller and Bliss 1975). Removablc, optical quality plexiglas windows with 25.4 mm thiekness bound either side of the eavity model to provide a full view of the eavity and the flow above it. The floor of the cavity is also made of 14 mm thiek plexiglas for optical access.

Two different wind tunnel eavity eeiling eonfigurations arc available. The first onc is an aluminum platc with 25.4 mm thiekness that ean be eonsidered a rigid-wall boundary condition. This boundary eondition helps excite the eavity vertical modcs and the "eut-on" frequencies of the eavity/duet eonfiguration (Rowlcy and Williams 2006). The performanee of this ceiling is discussed in the next ehapter.

In order to simulatc an unbounded cavity flow eneountered in practical bomb-bay eonfigurations, a flush-mounted aeoustie treatment is eonstrueted to replaee the rigid eeiling plate. The new eavity eeiling modifies thc boundary eonditions of the previous sound hard eeiling. This aeoustie treatment eonsists of a porous metal laminate (MKI BWM series, Dynapore P/N 408020) baeked by 50.8 mm thiek bulk pink fiberglass insulation (Figure 24). This aeoustie treatment eovers the whole eavity mouth and extends 1 ineh upstream and downstream of the leading edge and trailing edge, respcetively. This kind of aeoustie treatment reduees refleetions of aeoustie waves. The performanee of this treatment is assessed in the next ehapter.

The exhaust flow is dumped to atmosphere via a 5 degree angle diffuser attached to the rear of the cavity model for pressure reeovery. A custom rectangular-to-round transition pieee is used to conneet the reetangular diffuser to the 6 ineh diameter exhaust pipe.

Three struetural supports are used to reduee tunnel vibrations (Carroll et al. 2004). Two of these struetural supports attaeh to both sides of the test seetion inlet flange, and the additional structural support is installed to support the iron exhaust pipe (Figure 24).

Pressure/Temperature Measurement Systems

Stagnation pressure and temperature are monitored during eaeh wind tunnel run and eonverted to Mach number via the standard isentropie relations with an estimated uneertainty of ± 0.01. The referenee tube of the pressure transdueer is eonneeted to statie pressure port (shown in Figure 24) using 0.254 mm ID vinyl tubing to measure the upstream statie pressure of the eavity. The stagnation and static pressurcs are measured separatcly with Druek Model DPI145 pressure transducers (with a quoted measurement precision of 0.05% of reading). The stagnation temperature is measured by an OMEGA thermoeouple (Model DP80 Series, with 0.1 deg. C nominal resolution).

Two pressure transducers are located in the test section to measure the pressure fluctuations. The first transducer is a flush-mounted unsteady Kulite dynamic pressure transducer (Model XT-190-50A) and is an absolute transducer with a measured sensitivity (2.64 +/- 0.06)x10^{-7} V/Pa with a nominal 500 kHz natural frequency, 3.447x10^{5} Pa (50 psia) max pressure, and is 5 mm in diameter. This pressure transducer is located on the cavity floor (y=-D) 0.6 inch upstream from the cavity real wall (x=L), and 8.89 mm (z=8.89 mm) away from the mid-plane. This position allows optical access from the mid-plane of cavity floor for flow visualization and avoids the possibility of coinciding with a pressure node along the cavity floor (Rossiter 1964). The second pressure transducer is also an Kulite absolute transducer (with measured sensitivity (5.13 +/- 0.03)x10^{-7} V/Pa and nominal 400 kHz natural frequency, 1.724x10^{5} Pa (25 psia) max pressure, 5 mm in diameter), and it is flush mounted in the tunnel side wall 63.5 mm downstream of the cavity as shown in Figure 24. From a series of vibration impact tests performed in a previous study (Carroll et al. 2004), the results indicated that the pressure transducer outputs are not affected by the vibration of the structure. An experiment to validate this hypothesis is discussed in the next Chapter. Due to a modification of the experimental setup, the second pressure sensor is moved to the cavity floor (Figure 24) for both open-loop control and closed-loop control.

A PC monitors the upstream Mach number, stagnation pressure, and stagnation temperature, as well as the static pressure. This computer is also used for remote pressure valve control (Figure 23) in order to control the freestream Mach number using a PID controller. In addition, an Agilent E1433A 8-channel, 16-bit dynamic data acquisition system with built-in anti-aliasing filters acquires the unsteady pressure signals and communicates with the wind tunnel control computer via TCP/IP for synchronization. The code for both data acquisition and remote pressure control output generation are programmed in LabVIEW. The pressure sensor time-series data are also collected for both the baseline and controlled cavity flows for post-test analysis.

Facility Data Acquisition and Control Systems

The schematic of the control hardware setup is shown in Figure 25. For the real-time digital control system, the voltage signals from the dynamic pressure transducers are first pre-amplified and low-pass filtered using Kemo Model VBF 35. This filter has a cutoff range 0.1 Hz to 102 kHz, and three filter shapes can be used. Option 41 with nearly constant group delay (linear phase) in the pass band and 40dB/octave roll-off rate is chosen. The cutoff frequency is 4 kHz for a sampling frequency of 10.24 kHz. The signal is then sampled with a 5-channel, 16-bit, simultaneous sampling ADC (dSPACE Model DS2001).

The control algorithms are coded in SIMULINK and C code S-functions and are compiled via Matlab/Real-Time Workshop (RTW). These codes are uploaded and run on a floating-point DSP (dSPACE DS1006 card with AMD Opteron™ Processor 3.0GHz) digital control system. The DSP was also used to collect input and output data from the DS2001 ADC boards as well as computing the control signal once per time step. At each iteration, the computed control effort is converted to an analog signal accomplished using a 6-channel 16-bit DAC (DS2102). This signal is passed to a reconstruction filter (Kemo Model VBF 35 with identical settings to the anti-alias filters) to smooth the zero-order hold signal from the DAC. The output from this filter is then sent to a high-voltage amplifier (PCB Model 790A06) to produce the input signal for the actuator. The computer is also able to access the data with the dSPACE system via the Matlab mlib software provided by dSPACE Inc.

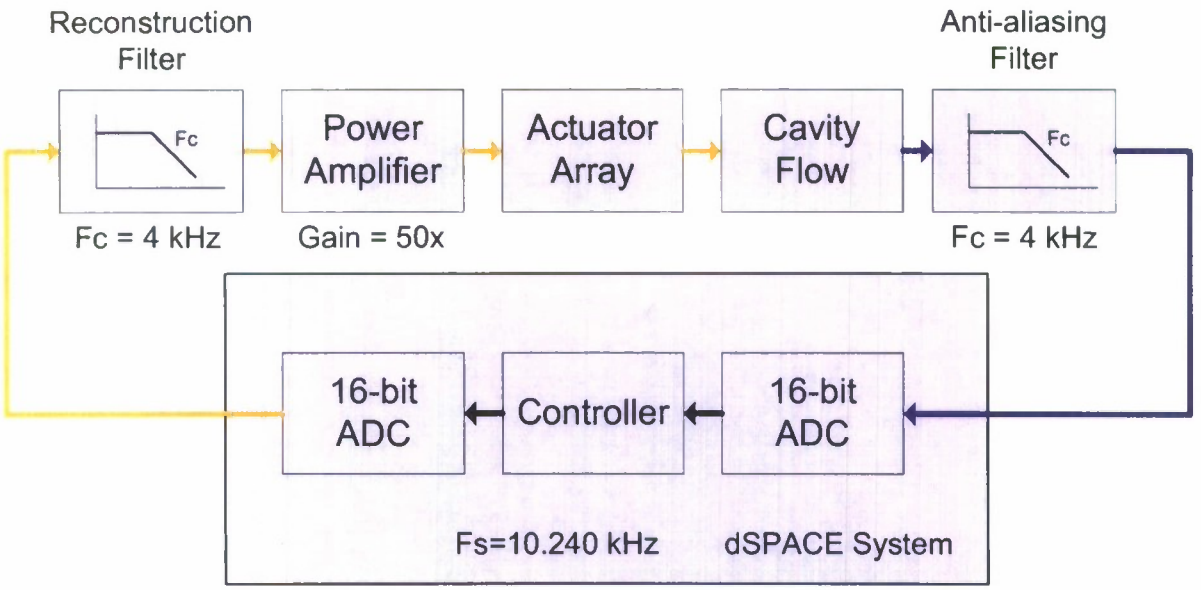

Figure 25: Schematic of the control hardware setup.

Actuator System

In order to achieve effective closed-loop flow control, high bandwidth and powerful (high output) actuators are required. According to Cattafesta et al. (2003), one kind of actuator – called "Type A" – has these desirable properties. Such actuators include piezoelectric flaps and have successfully been used for active control of flow-induced cavity oscillations by Cattafesta (1997) and Kegerise et al. (2002). Their results show that the external flow has no significant influence of the actuator dynamic response over the range of flow conditions. Their later work (Kegerise et al. 2004; 2007a,b) also shows that one bimorph piezoelectric flap actuator is capable of suppressing multiple discrete tones of the cavity flow if the modes lie within the bandwidth of the actuator. Therefore, the piezoelectric bimorph actuator is a potential candidate for the present cavity oscillation problem.

Another candidate actuator is the synthetic or zero-net mass-flux jet (Williams et al. 2000; Cabell et al. 2002; Rowley et al. 2003, 2006; Caraballo et al. 2003, 2004, 2005; Debiasi et al. 2003, 2004; Samimy et al. 2003, 2004; Yuan et al. 2005). This actuator can be used to force the flow via zero-net-mass flux perturbations through a slot in the upstream wall of the cavity. Although the actuator injects zero-net-mass through the slot during one cycle, a non-zero net momentum flux is induced by vortices generated via periodic blowing and suction through the slot.

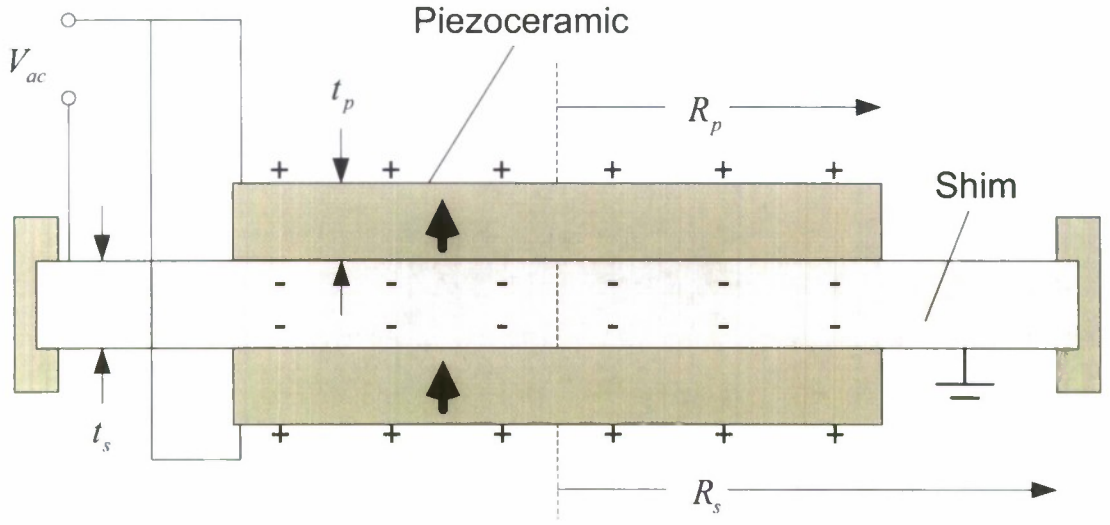

Figure 26: Bimorph bender dise aetuator in parallel operation.

In this researeh, a piezoeleetrie-driven synthetie jet aetuator array is designed. This type of synthctic jet based aetuators normally gives a larger bandwidth than the piezoeleetrie flap type of aetuators. A typieal eommereial parallel operation bimorph piezoeleetrie dise (APC Ine., PZT5J, Part Number: P412013T-JB) is used for this design. The eomposite plate is a bimorph piezoeleetrie aetuator, which ineludes two piezoeleetrie patehes on upper and lower sides of a brass shim in parallel operation (Figure 26). The final design of the actuator array eonsists of 5 single aetuator units. Eaeh aetuator unit eontains one eomposite plate and two reetangle orifices shown in Figure 27. The designed slot geometries for the aetuator array are shown in Figure 28

Another advantage of this design is that it avoids the pressure imbalance problem on the two sides of the diaphragm during the experiment. Since the two eavities on either side of a single aetuator unit are vented to the loeal statie pressure, the diaphragm is not statieally deflected when the tunnel statie pressure deviates from atmosphere. The ehallenge is whether these aetuators ean provide strong enough jets to alter the shear layer instabilities in a broad Maeh number range and also whether the aetuators produee a eoherent signal that is sufficient for effeetive system identifieation and eontrol.

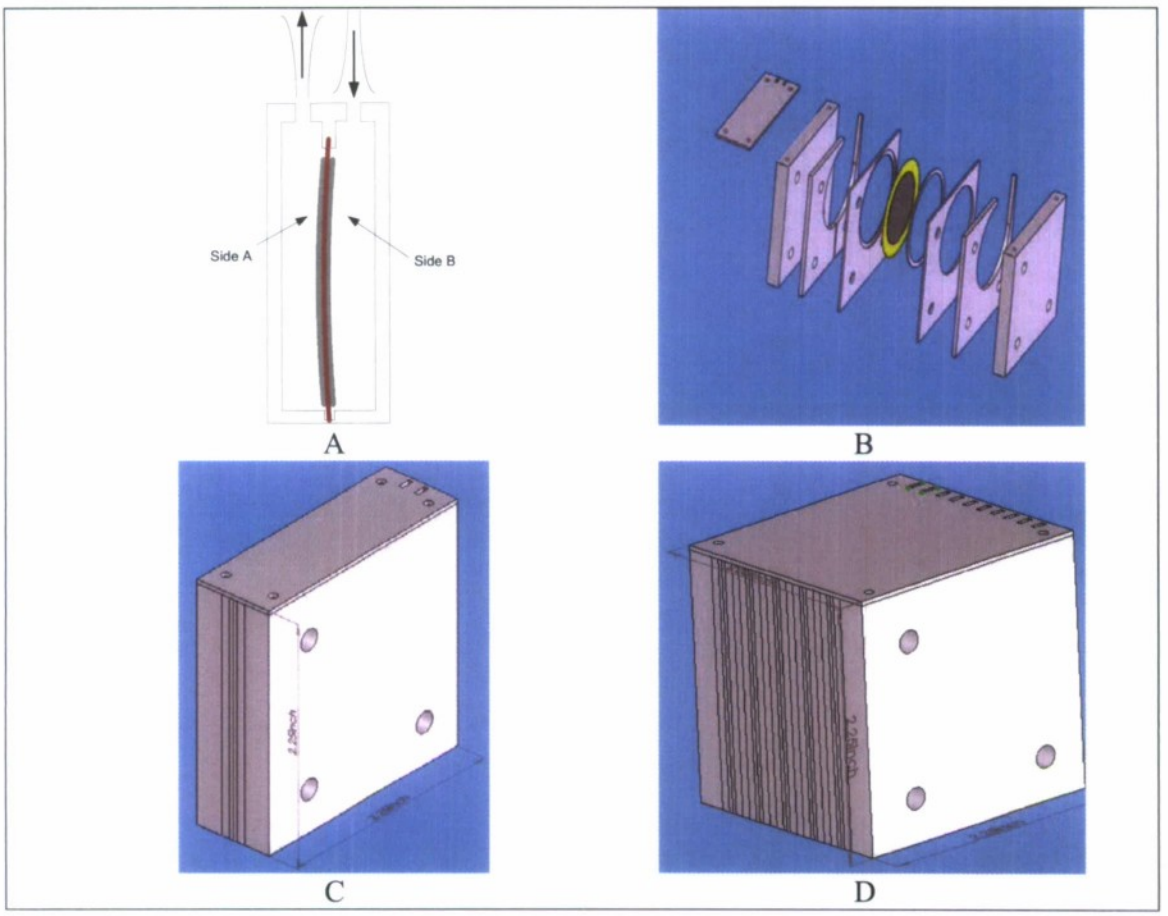

Figure 27: Designed ZNMF actuator array. A) Operation plot. B) Assembly diagram of single unit. C) Singe unit of the actuator. D) Actuator array.

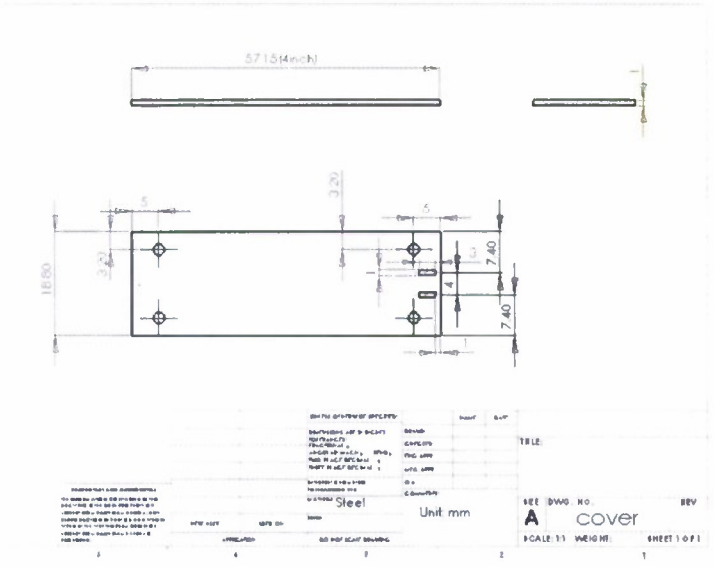

Figure 28: Dimensions of the slot for designed actuator array.

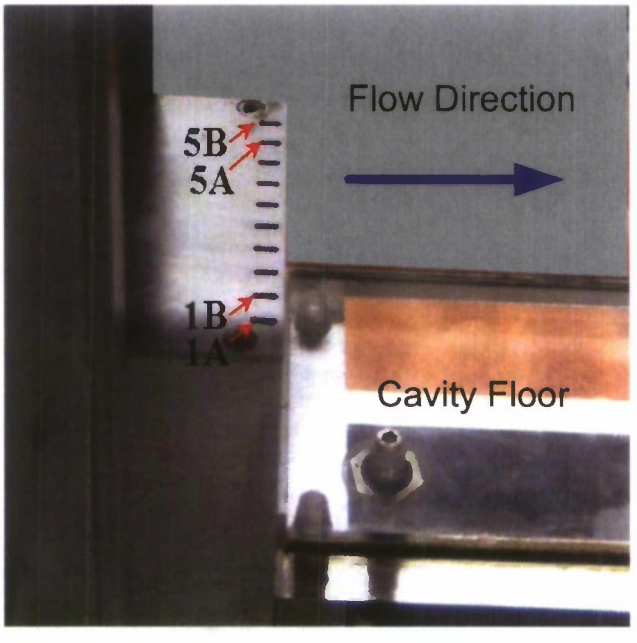

Figure 29: ZNMF actuator array mounted in wind tunnel.

A lumped element actuator design code (Gallas et al. 2003) was used together with an experimental trial-and-error method to design the single actuator unit. To calibrate this compact actuator array, the centerline jet velocities from each slot are measured using constant-

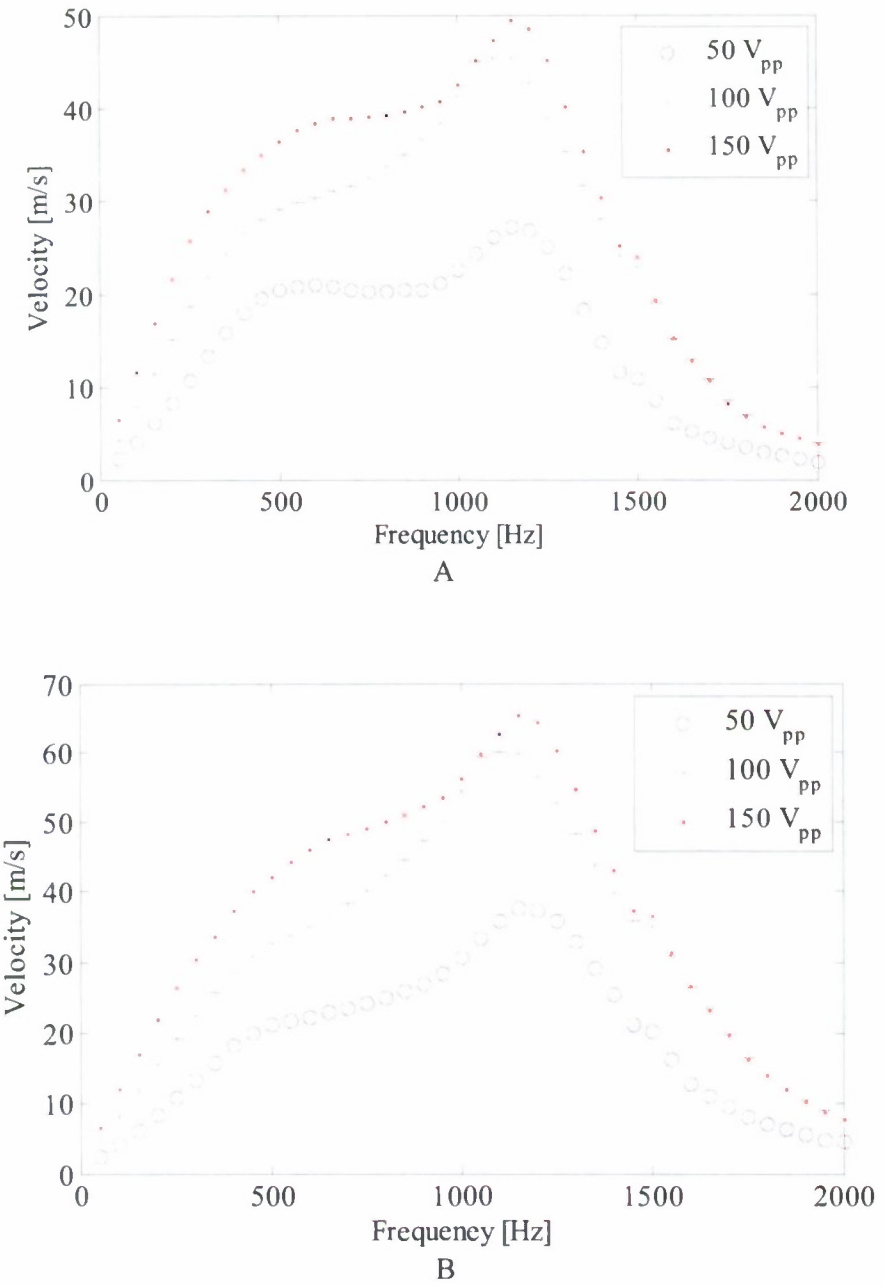

Figure 30: Bimorph 3 centerline rms velocities of the single unit piezoelectric based synthetic actuator with different excitation sinusoid input signal. A) For side A. B) For side B.

temperature hotwire anemometry (Dantec CTA module 90C10 with straight general purpose 1-D probe model 55p11 and straight short 1-D probe support model 55h20). A Parker 3-axis traverse system is used to position the probe at the center of actuator slots. The sinusoidal excitation signal from the Agilent 33120A function generator is fed to the 790A06 PCB power amplifier with a constant gain of 50 V/V. The piezoceramic discs are driven at three input voltage levels: 50 Vpp, 100 Vpp, and 150 Vpp, respectively, over a range of sinusoidal frequencies from 50 Hz

to 2000 Hz in steps of 50 Hz. Each bimorph dise serves as a wall between two eavities labeled side A and side B. The notation used to identify eaeh bimorph and its eorresponding slots is shown in Figure 29. The rms velocities of the slots 3A and 3B loeated in thc eenterline of the cavity are shown in Figure 30 as an example. Figure 31 shows the simulation result ealculatcd by the LEM actuator design code and is superposed on the cxperimental result, Figurc 30. Thc results show that, the LEM aetuator dcsign code provides a prctty aeeurate rms vclocity estimation of synthetic jet over a large frequency range between 50 Hz and 2000 Hz. Finally, the mcasure input current level to the actuator array after the amplifier is measured. The results arc shown in Figure 32 and indieate that the input eurrent will saturate above 136mApp, whieh means if thc input voltage is larger than 100 Vpp, the current to the aetuator will keep a eonstant value. During the closed-loop experiments, an upper limit of 150 Vpp is used sinee the eurrent probe is unavailablc.

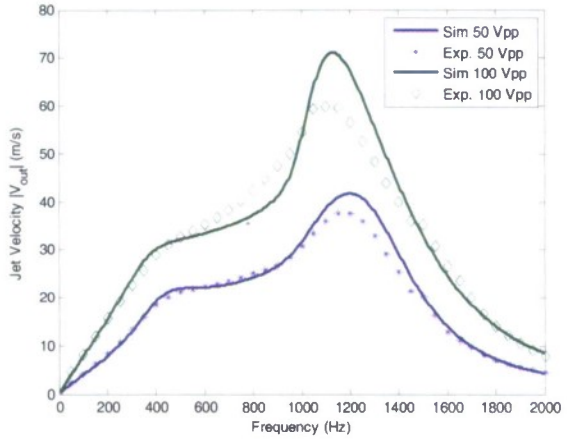

Figure 31: The comparison plot of thc cxpcrimcnt and simulation result of thc actuator design eode for bimorph 3. The output is the eenterline rms velocities of the single unit piezoelectric based synthctic actuator with different excitation sinusoid input signal for side B.

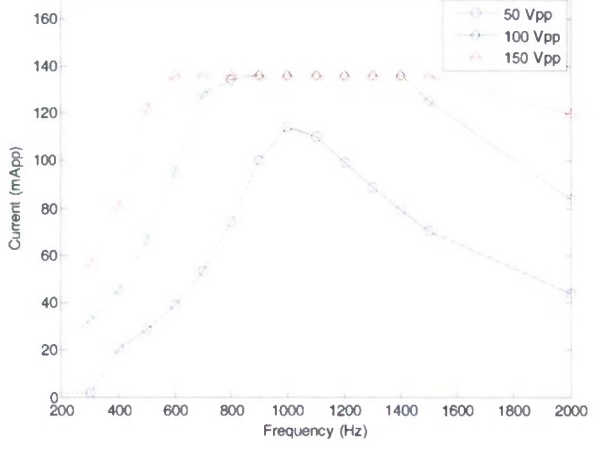

Figure 32: Current saturation effects of thc amplifier.

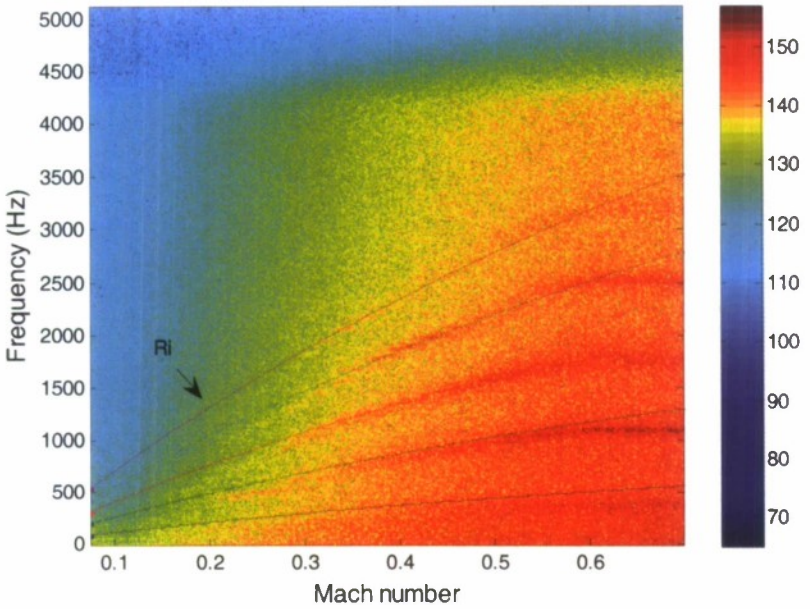

Figure 33: Spectrogram of pressure measurement (ref 20e-6 Pa) on the cavity floor with acoustic treatment superimposed with the Rossiter modes at L/D=6 (with α=0.25, κ=0.7).

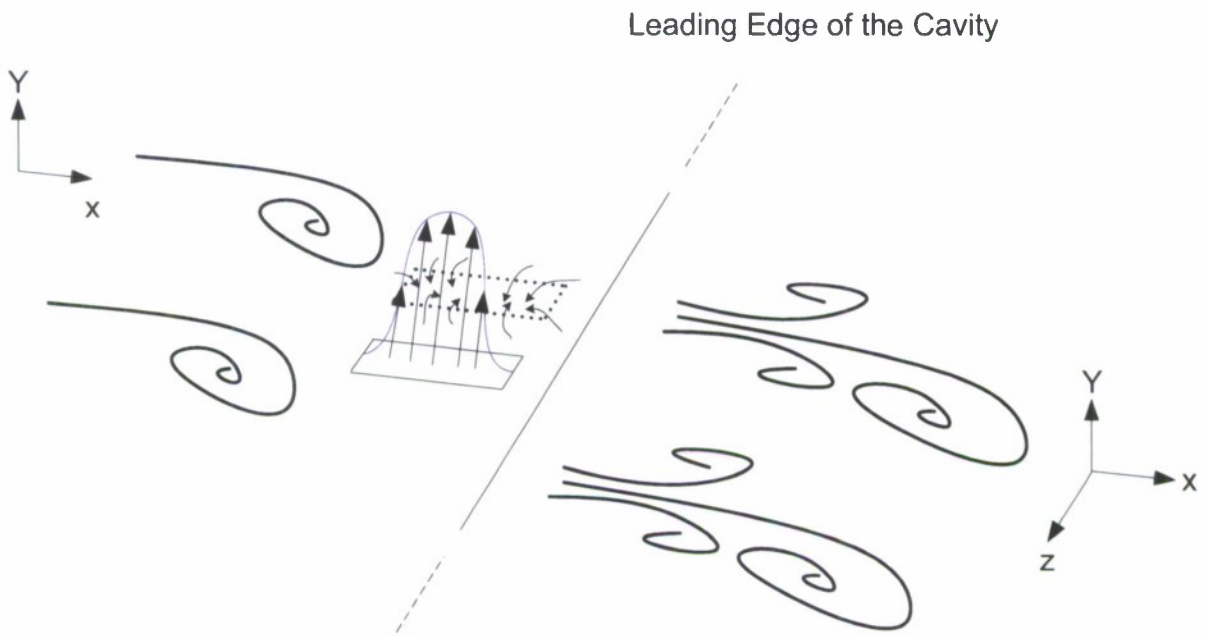

Figure 34: Schematic of a single periodic cell of the actuator jets and the proposed interaction with the incoming boundary layer.

Figure 33 shows the spectrogram of the pressure measurement on the cavity floor with acoustic treatment. The Rossiter modes are superimposed on this figure. The experimental details are explained in the next chapter. For this study, the lower portion of the Mach number range (from 0.2 to 0.35) is our control target as an extension to previous work by Kegerise et al. (2007a,b). The desired bandwidth of the designed actuator should cover the dominant peaks of Rossiter mode 2, 3 and 4, which is between 500 Hz and 1500 Hz. (Rossiter mode 1 is usually weaker compared to Rossiter modes 2, 3 and 4.) Over this frequency range, the designed actuator can generate large disturbances. In addition, the array produces normal oscillating jets that seek to penetrate the boundary layer, resulting in streamwise vortical structures. In essence, it acts like a virtual vortex generator. A simple schematic of the actuator jets interacting with the flow vortical structures is shown in Figure 34 The approach boundary layer contains spanwise vorticity in the x-y plane (the coordinate is shown in Figure 24). By interacting with the ZNMF actuator jets, the 2D shape of the vortical structures transform to a 3D shape with spanwise vortical structures. These streamwise vortical disturbances seek to destroy the spanwise coherence of the shear layer, and the corresponding Rossiter modes are disrupted (Arunajatesan et al. 2003). Alternatively, the introduced disturbances may modify the stability characteristics of the mean flow, so that the main resonance peaks may not be amplified (Ukeiley et al. 2003). Unfortunately, the flow interaction was not characterized in this report and will be addressed in future work.

Instead of using one specific amplitude and one frequency in open-loop control, a closed-loop control algorithm is used in this study to exam the effects of the disturbance with multiple amplitudes and multiple frequencies. Thus, the present actuator represents a hybrid control approach, in which we seek to reduce both the Rossiter tones and the broadband spectral level.

4.3 Wind Tunnel Experimental Results and Discussion

In the present baseline (i.e., uncontrolled) experimental study, flow-acoustic resonances in the test section region and in the cavity region are examined. A schematic of the simplified wind tunnel model and the cavity region of the experimental setup are shown in Figure 35.

Data Analysis Methods

The cavity and wind tunnel acoustic modes can be obtained experimentally using two approaches. One way is to measure the output of each unsteady dynamic pressure sensor for different fixed freestream Mach numbers and then find the spectral peaks for each discrete Mach number. However, with this method it is difficult to track the gradual frequency changes with Mach number. The other choice is to record each unsteady pressure sensor output continuously as the Mach number is increased gradually over the desired range. Then, a joint-time frequency analysis (JTFA) (Qian and Chen 1996) is applied to these recorded pressure time series data. JTFA provides information on the measurement in both the time and frequency domains. Finally, the time axis is converted to Mach number via synchronized measurements of the Mach number versus time. Similar analysis methods can be found in Cattafesta et al. (1998), Kegerise et al. (2004), and Rowley et al. (2005). In this study, the sampling frequency for experimental data collection is 10.24 kHz and the frequency resolution is 5 Hz. The cut-off frequency of the anti-aliasing filter is 4 kHz, and 500 continuous blocks of time series data are used in the analysis. During the experiment, Mach number sweeps from 0.1 to 0.7 in about 100 seconds.

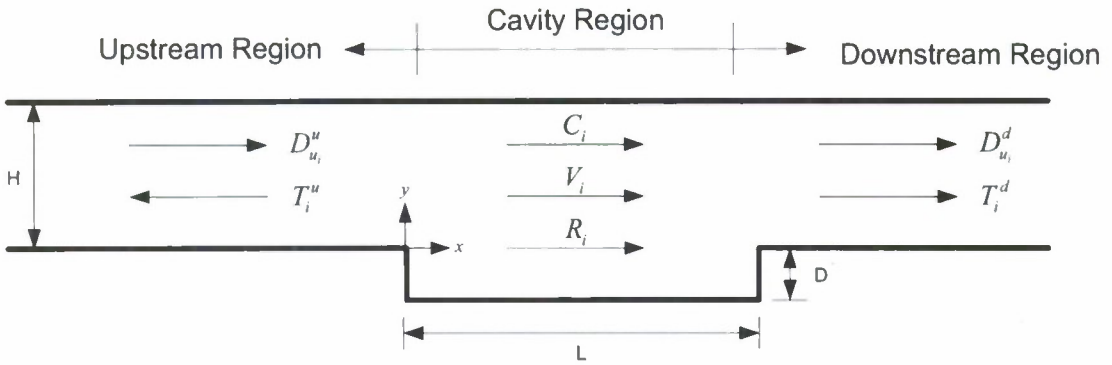

Figure 35: Schematic of simplified wind tunnel and cavity regions acoustic resonances for subsonic flow.

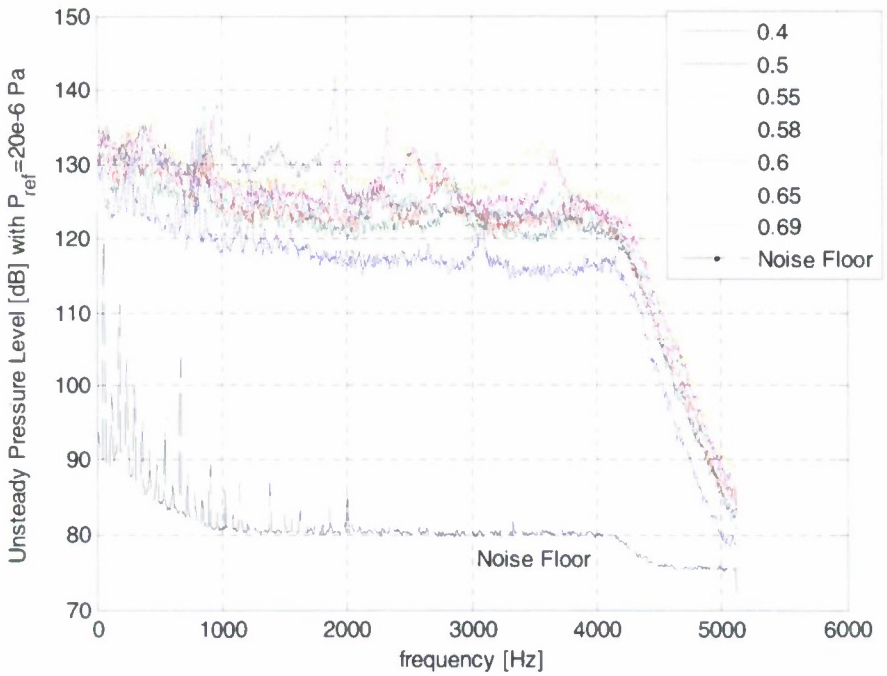

Figure 36: Noise floor level comparison at different discrete Mach numbers with acoustic treatment at trailing edge floor of the cavity with L/D=6.

Noise Floor of Unsteady Pressure Transducers

The effective in-situ noise floor of the two unsteady pressure transducers is presented in Figure 36. Each noise floor measurement is compared with the spectra obtained at different discrete Mach numbers for the acoustically treated L/D=6 cavity. Within the tested frequency range, the signal-to-noise ratio (SNR) is in excess of 30 dB, which demonstrates adequate resolution of unsteady pressure transducers for the present experiments despite their large full-scale pressure ranges.

Baseline Experimental Results and Analysis

The unsteady pressure transducer JTFA measurement for the trailing edge floor of the cavity is shown in Figure 37. The results illustrate a very clean flow field below Mach 0.6. Therefore, the experimental Rossiter modes R_i shown in JTFA plot (Figure 37) now follow the estimated Rossiter curves. At higher upstream Mach numbers (M>0.6), the experimental Rossiter modes deviate slightly from the expected Rossiter curves. This is partly because the estimated curves use the upstream static temperature to calculate the speed of sound. This estimation does not account for the expected significant static temperature drop due to the large flow acceleration near the aft cavity region seen by Zhuang et al. (2003). Another possible reason for these deviations of the flow-acoustic resonance comes from the structural vibration coupling with the Rossiter modes. At high Mach numbers above 0.6, the structural vibrations may cause a lock-on phenomenon with the Rossiter modes. For this study, all experiments are thus performed below M = 0.6.

In conclusion, the observed flow-acoustic behavior of the acoustically treated cavity model behaves as expected below M = 0.6 and is therefore suitable for application of open-loop and closed-loop flow control.

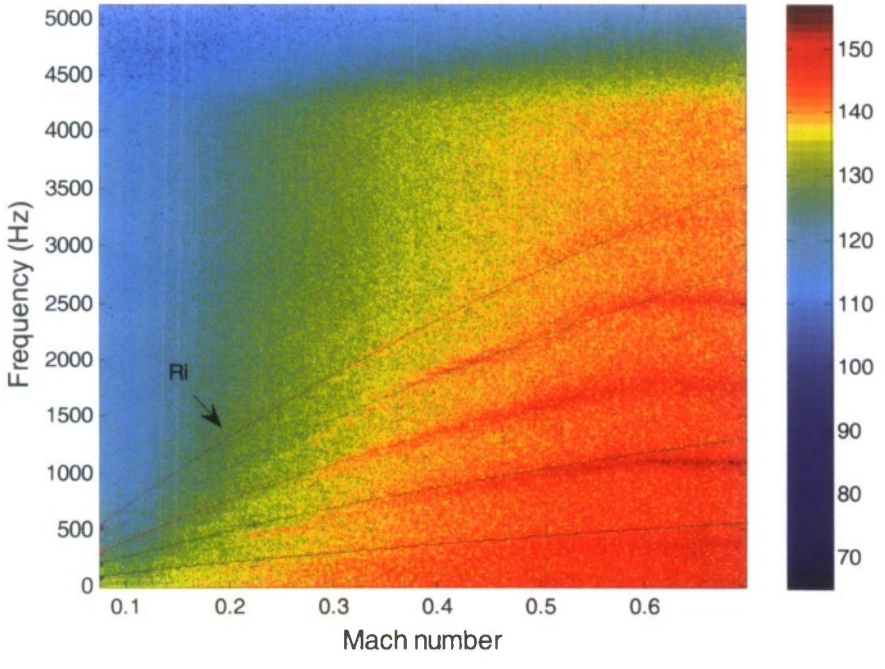

Figure 37: Spectrogram of pressure measurement (ref 20e-6 Pa) on the cavity floor with acoustic treatment superimposed with the Rossiter modes at L/D=6 (with α=0.25, κ=0.7).

Open-Loop Experimental Results and Analysis

The open-loop and closed-loop experimental results using the designed actuator array are shown in this section. Before the control experiments, measurements of the pressure sensor at the surface of the trailing edge of the cavity with the without the actuator turned on are shown in Figure 38. Without the upcoming flow, the noise floor shows a significant peak at 660 Hz and a

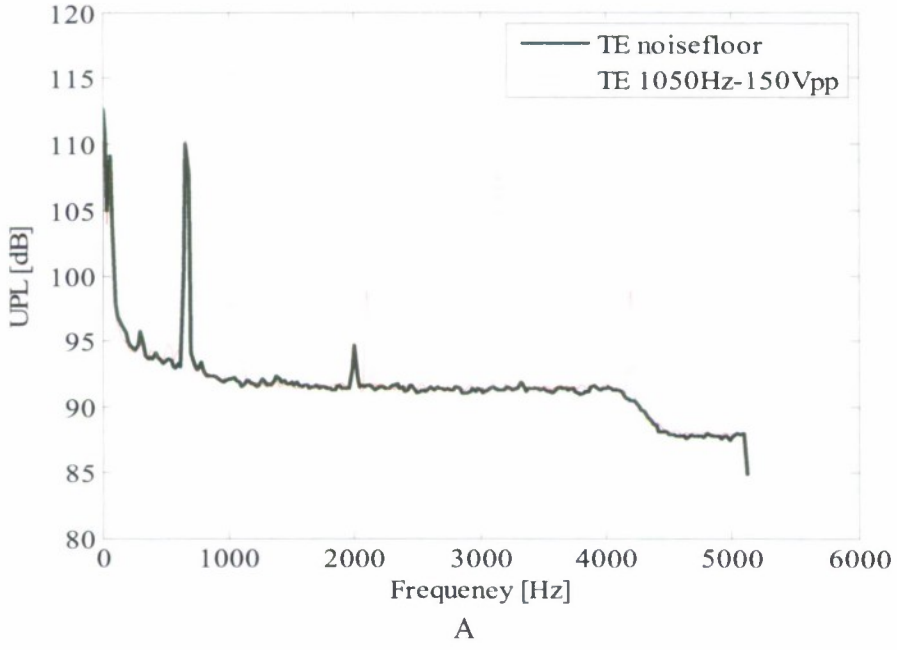

A

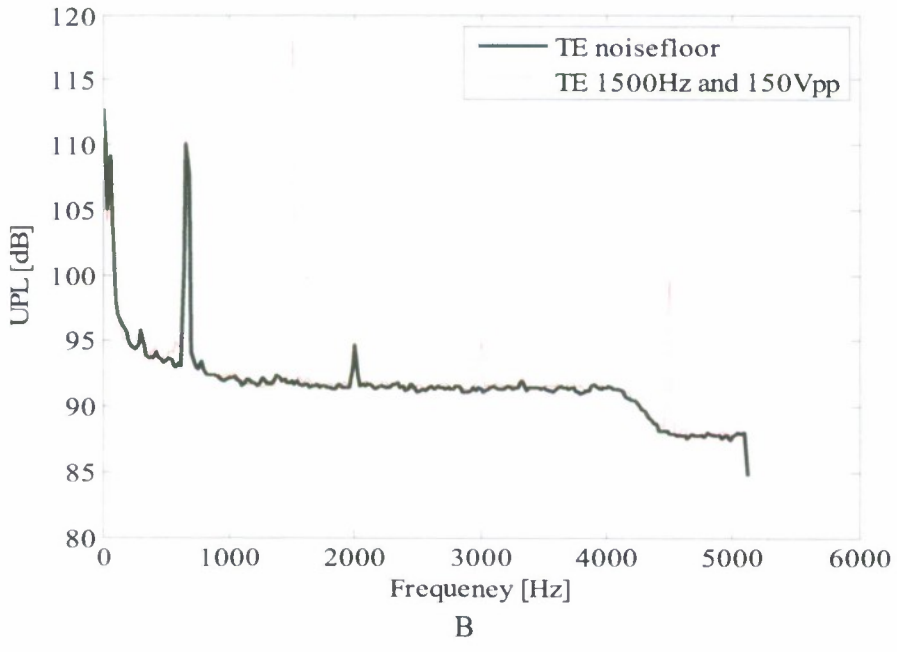

B

Figure 38: Noise floor of the unsteady pressure level at the surface of the trailing edge of the cavity with and without the actuator turned on. A) The exciting sinusoidal input has frequency 1050 Hz and amplitude 150 Vpp. B) The exciting sinusoidal input has frequency 1500 Hz and amplitude 150 Vpp. The peaks near 600 Hz and 2000 Hz are electronic noise.

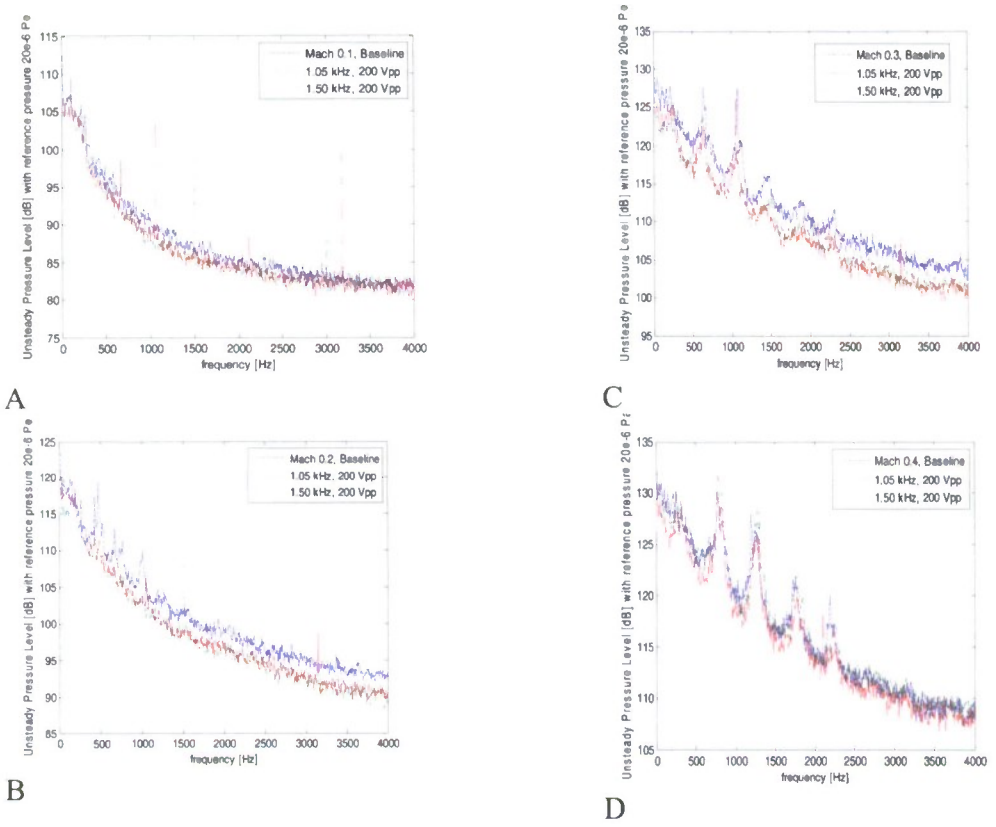

Figure 39: Open-loop sinusoidal control results for flow-induced cavity oscillations at trailing edge floor of the cavity. A) At Mach number 0.1. B) At Mach number 0.2. C) At Mach number 0.3. D) At Mach number 0.4. The cavity model with 6 inch long and L/D=6.

small peak at 2000 Hz. The pressure sensor can also sense the acoustic disturbances associated with the excitation frequency and its harmonics, and the measured unsteady pressure level can reach 115-120 dB. The extent to which the measured levels deviate from theses values with flow on (considered below) indicates the relative impact of the actuator on the unsteady flow.

First, open-loop active control is explored. The purpose of the open-loop experiments is to verify if the synthetic jets generated from the designed actuator array can affect and control the cavity flow. A parametric study for the open-loop control is explored first. A sinusoidal signal is chosen as the excitation input with the frequency swept from 500 Hz to 1500 Hz. The open-control performance is best over the frequency range 1000 Hz to 1500 Hz, which corresponds to the resonance frequencies of the actuator array. Since at the resonance frequency, the actuator array can generate larger velocity jet, and the blow coefficient $B_c = \dot{m}/(\rho U_\infty A_{cavity})$ increases. As a result, the control effect increases.

For these open-loop tests, the upstream flow Mach number is varied from 0.1 to 0.4. For illustration purposes, results are examined here for two sinusoidal signals with 200 Vpp and excitation frequencies at either 1.05 kHz or 1.5 kHz to drive the actuator array. The 1.05 kHz excitation frequency is close to the resonance frequency of the actuator, while the 1.5 kHz frequency lies between the second and third Rossiter modes. The experimental results shown in

Figure 39 illustrate that this actuator array ean successfully reduce multiple Rossiter modes, particularly at Maeh number 0.2 and 0.3. In addition, the pressure fluctuation is mitigated at the broadband level on the surface of the cavity floor for all the tested flow eonditions. However, new peaks are generated by the exeitation frequeneies and their harmonies, espeeially at low Mach number 0.1. With increasing upstream Maeh number, the unsteady pressure level also increases and the effect of the control is reduced. Note the synthetic jets introduee temporal and spatial disturbanees to modify the mean flow instabilities and destroy the eoherenee structure in spanwise, respectively. The effeetiveness of the actuator seales with the momentum coefficient, whieh is inversely proportional to the square of the freestream velocity. So, as the upstream Mach number increases, the synthetie jets are eventually not strong enough to penetrate the boundary layer and the eontrol effeet is reduced. Future work should perform detailed measurements to validate this hypothesis.

The results of the opcn-loop control suggest that this kind of actuator array can generate significant disturbances not only along the flow propagation direction but also in the spanwise direction of the cavity. The combination of these effects disrupts the Kelvin-Helmholtz type of convective instability waves, which are the souree of the Rossiter modes. As a result, multiple resonances are redueed via active control. The experimental results also show the limitation of the open-loop eontrol.

Closed-Loop Experimental Results and Analysis

The open-loop control results suggest that this eompaet aetuator array may be effeetive for adaptive closed-loop control. As discussed abovc, the synthetic jets add disturbances to disrupt the spanwise coherence strueture of the shear layer and result in a broadband reduetion of the oscillations. However, at the same time, the coherence between thc drive signal and the unsteady pressure transducer will be reduced. High coherenee is eonsidered essential for accurate system identification methods. To exam the accuracy of the system ID algorithm with the ehange of the estimated order, an off-line system ID analysis is first performed. The nominal flow condition is chosen at M = 0.275 (to match that of Kegerise et al. 2007a,b) with a L/D=6 cavity, and two system ID signals, one with white noise (broadband frequeney and amplitude 0.29 Vrms) and the other with a chirp signal (amplitude 0.86 Vrms and f_L = 25 Hz to f_H = 2500 Hz in T = 0.05 see), are used as a broadband excitation souree to identify the system. The running error variances the system ID are shown in Figure 40. It is clear that the larger the estimated order, p, the more accurate is the system ID algorithm. However, due to the limitations of the DSP hardware, we eannot ehoose very large values of the estimated order for system ID algorithm on-line.

Onc potential advantage of thc closed-loop adaptive control algorithm is that it does not rely exelusively on aecurate system ID. Figure 41 shows the result of the closed-loop real-time adaptivc system ID together with the GPC control algorithm for an upstream Mach number 0.27. Based on thc above system ID results, due to the DSP hardware limitation, the estimated GPC ordcr and the predictivc horizon are chosen as 14 and 6, respectively. The breakdown voltage of the actuator array restricts the exeitation voltage level; therefore, the diagonal element of the input weight penalty matrix R is chosen as 0.1. This researeh represents an extension of Kegerise et al. (2007b) where the system ID algorithm and the elosed-loop eontroller design algorithm are used simultaneously in a real-time application. It is important to

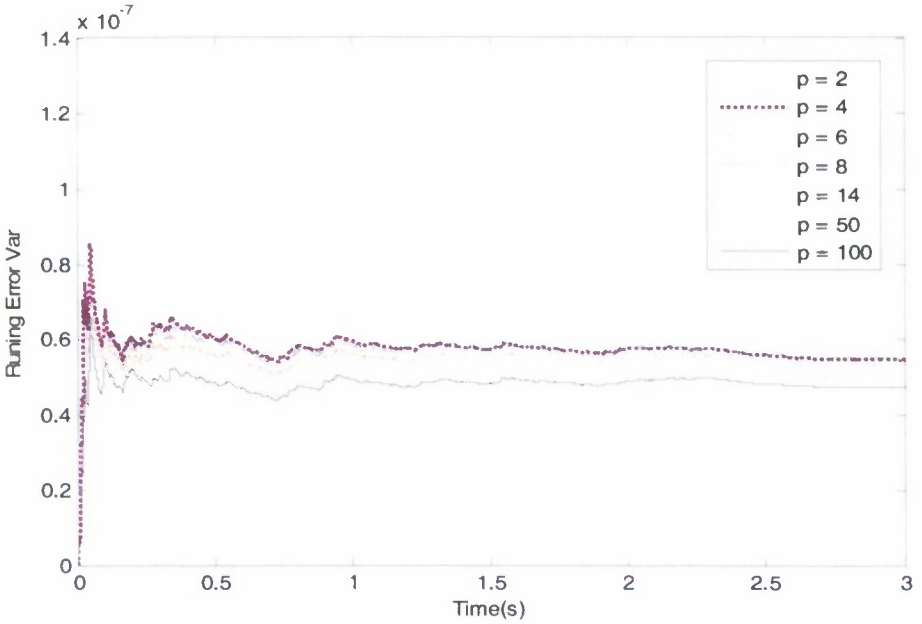

A

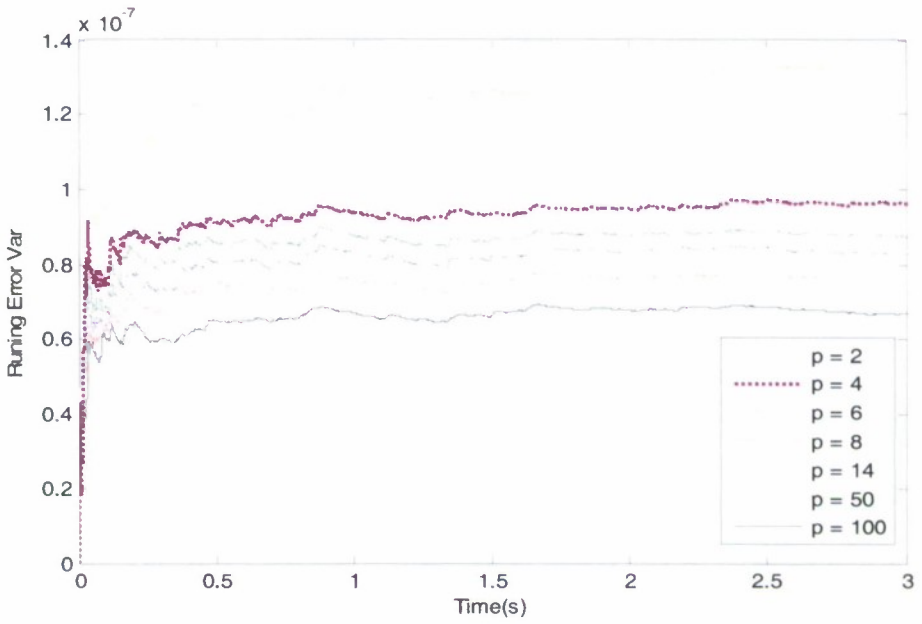

B

Figure 40: Running error variance plot for the system identification algorithm. A) With chirp signal as input. B) With white noise signal as input. Upstream Mach number is 0.275, L/D=6.

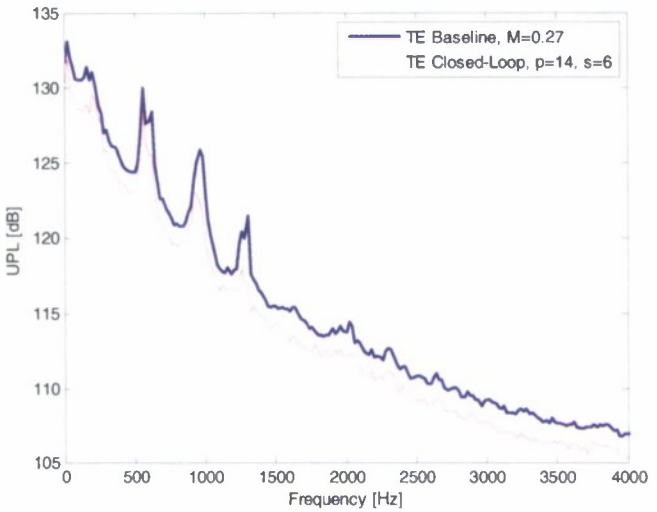

Figure 41: Closed-Loop active control result for flow-induced cavity oscillations at Mach 0.27 at the trailing edge floor of the L/D =6 cavity. The control algorithm uses an estimated order of 14 for both the system ID and GPC algorithms, and the predictive horizon is chosen as 6. A chirp signal is used as the system ID excitation source.

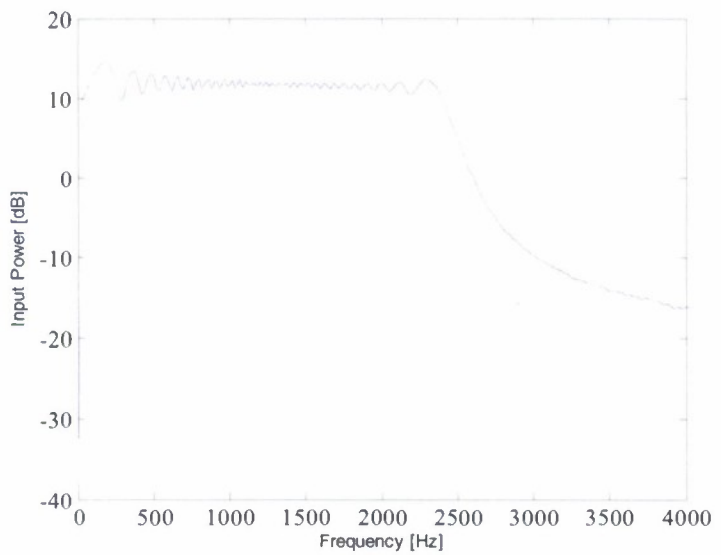

Figure 42: Input signal of the Closed-Loop active control result for flow-induced cavity oscillations at Mach 0.27 at the trailing edge floor of the L/D =6 cavity. The control algorithm uses an estimated order of 14 for both the system ID and GPC algorithms, and the predictive horizon is chosen as 6. A chirp signal is used as the system ID excitation source.

note that only the system ID white noise or chirp signal is used to identify the open-loop dynamics, and the feedback signal is not used for this purpose. Clearly, the results show that the GPC controller can generate a series of control signals to drive the actuator array resulting in

significant reductions for the second, third, and fourth Rossiter modes by 2 dB, 4 dB, and 5 dB, respectively. In addition, the broadband background noise is also reduced by this closed-loop controller; the OASPL reduction is 3 dB. The input signal is shown in Figure 42.

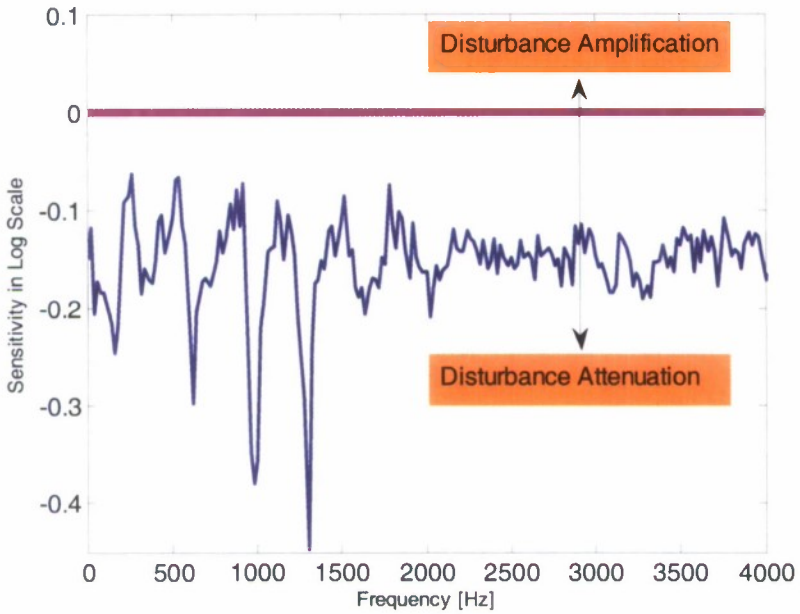

Figure 43: Sensitivity function of the closed-loop control for M=0.27 upstream flow condition. The estimated order is 14, prediction horizon is 6, and the input weight R is 0.1.

The sensitivity function discussed earlier is shown in Figure 43. A negative amplitude value indicates disturbance attenuation, while a positive value indicates disturbance amplification. The results show that all the points are negative, which indicates the closed-loop controller reduces the pressure fluctuation power at all frequencies. The spillover phenomenon (Rowley et al. 2006) is not observed in Figure 43. The spillover problem is generated because either the disturbance source and control signal or the performance sensor output and the measurement sensor output (feedback signal) are collocated.

The Bode's integral formula is,

$$\int_0^\infty \log\left|S(i\omega)\right| d\omega = \pi \sum_k \mathrm{Re}(p_k) \tag{4.1}$$

where p_k are the unstable poles of the loop gain of the closed-loop system. So, for a stable system, any negative area at the left hand side of the Equation 4.1 must be balanced by an equal positive area at the left hand side of the Equation 4.1. However, for present closed-loop control study, the left hand side of the Bode's integral formula is -38 rad/sec, which shows that Bode's integral formula does not hold here. Since this formula is valid for a linear controller, the combination of the adaptive system ID and controller is apparently nonlinear. A more detailed study is required in the future to validate this hypothesis.

A parametric study of the GPC is then studied by varying the estimated order and the predictive horizon. Figure 44 and Figure 45show that the control effects improve with

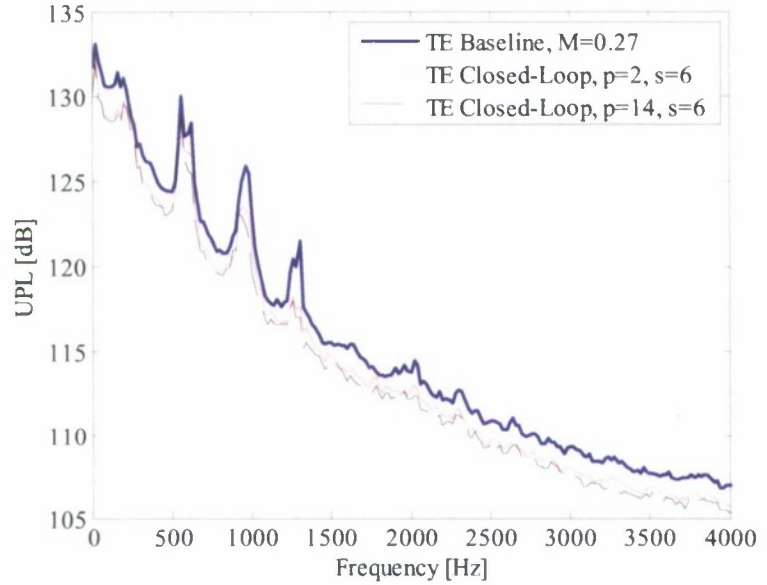

Figure 44: Unsteady pressure level of the closed-loop control for M=0.27, L/D=6 upstream flow condition with varying estimated order. The prediction horizon is 6, and the input weight is 0.1. The excitation source for the system ID is a swept sine signal.

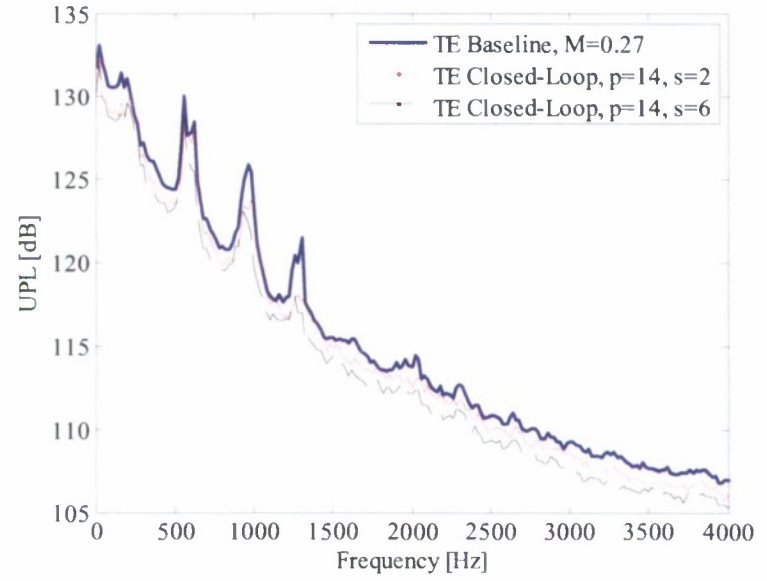

Figure 45: Unsteady pressure level of the closed-loop control for M=0.27, L/D=6 upstream flow condition with varying predictive horizon s. The estimated order of the system is 6, and the input weight is 0.1. The excitation source for the system ID is a swept sine signal.

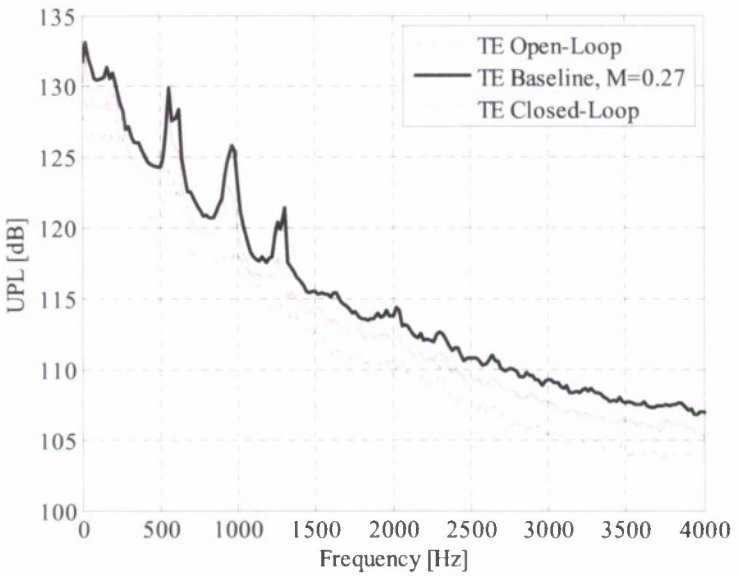

Figure 46: Unsteady pressure level comparison between the open-loop control and closed-loop control for M=0.27 upstream flow condition. The open-loop control uses a sinusoidal input signal at 1150 Hz forcing and 150 Vpp and the rms value is 53 V. The closed-loop control uses an estimated order 14, predictive horizon 6, input weight 0.1, and the input rms value is 43 V.

increasing order and predictive horizon.

The comparison between the open-loop and closed-loop results is shown in Figure 46for the same flow condition. Notice that the baseline measurement for a same flow condition can vary a little from case to case. The open-loop control uses a sinusoidal input signal at 1150 Hz forcing and 150 Vpp and the rms value of the input is 53V. The closed-loop control uses the estimated order 14, the predictive horizon 6, and the input weight 0.1, and the input rms value is 43 V.

5 Development of Quantitative Schlieren System

As mentioned earlier in order to be able to improve the estimate of the time dependent flow field and calculate the sources of the intense fluctuating pressures in the cavity in a compressible flow we will need to determine quantitative information about the density field. This section details the parts of this effort which were devoted to developing a quantitative Schliern tool. The following section will start with a brief introduction which is followed by a description of the experimental setup. This is followed by a sub-section which describes the analysis using the Two Microphone Method and the quantitative Schlieren instrument to investigate the acoustic field in a normal impedence tube where special attention is provided to the photodetector, enabling the estimate of the overall instrument sensitivity. Finally we will presents the results and discussion on experiments in the impedance tube.

5.1 Introduction and Experimental Set Up

The schlieren technique allows for the visualization of large density gradients commonly encountered in applications such as optical component testing and high-speed flows. The technique proved indispensable for supersonic flow imaging since World War II when it was applied to weapons development (Settles, 2001). It has also been used for turbulent flow visualization that uses various methods to produce density gradients such as a thermal gradient (Davis, 1971) or a gaseous mixture e(Al-Ammar et al, 1998).

Based on earlier work of Davis (1971) along with Wilson and Damkevela (1970) McIntyre et al (1991) developed a modern schlieren technique termed "optical deflectometry". The method coupled a conventional z-type schlieren system with photodetectors possessing very high frequency response to quantify density gradients in high-speed turbulent shear flows. The technique has been used to quantify cavity shear layers (Garg and Cattafesta, 2001) and high-speed axisymmetric jets(Doty and McLaughlin, 2005). Also of interest is the effort by Garg and Settles (1998) to develop a quantitative focused schlieren instrument which limits the integration path to approximately 5 mm. The tool developed here adapts the optical deflectometry technique to measure the acoustic field in a normal-incidence acoustic impedance tube.

A schematic of the normal-incidence acoustic impedance tube is shown in Figure 47. The tube is 0.724 m long with a 25.4 mm square cross section; it allows a plane wave acoustic field over a frequency range of 0 – 6.7 kHz. The walls of the impedance tube consist of 22 mm thick aluminum. A 22 mm thick aluminum plate is placed at one end of the tube to simulate a sound-hard boundary condition. A compression driver (JBL Pro 2426H) was mounted at the opposite end of the tube via a circular-to-square transition piece. A 5 kHz sinusoidal waveform is generated using an Agilent 33120A function generator and a Techron 7540 power amplifier. The test section was located at the end of the tube close to the specimen. In this study, borosilica optical quality glass windows are located 32.86 mm from the specimen and are 170 mm long, 25.4 mm wide, and 3.175 mm thick. The transition from the test section to the specimen is smooth and care is taken to minimize leakage at all joints in the tube.

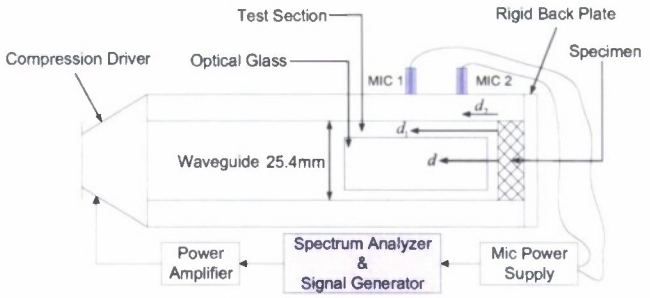

Figure 47: Schematic of normal incidence impedance tube.

The setup of the z-type optical deflectometer is shown in Figure 48**Error! Reference source not found.**, and a list of the labeled system components is provided in the Appendix. The light source consisted of a 100 W tungsten-halogen lamp in air-cooled aluminum housing. An f2/50.8 mm condenser lens focused the light on an adjustable rectangular aperture set at 1 mm by 2 mm, which was placed at the focal point of the first parabolic mirror (f10/100 mm). The resulting collimated beam passes through the test section, and the second parabolic mirror focuses the beam on a knife edge mounted on a 1-D traverse system (Newport Model ESP100) for nanometer-automated positioning during calibration. Two focusing lenses were used to project the shlieren image on a translucent screen mounted on a 2-D traverse (Velmex Model MB4012P40J-S4) controlled using a Velmex controller (Velmex Model VXM 1). A fiber-optic cable with a 0.25 mm diameter pinhole aperture is mounted on the screen to route the optical signal to an avalanche photodiode (Hamamatsu Model C5460-01). A second fiber-optic sensor is used to monitor intensity variations of the source.

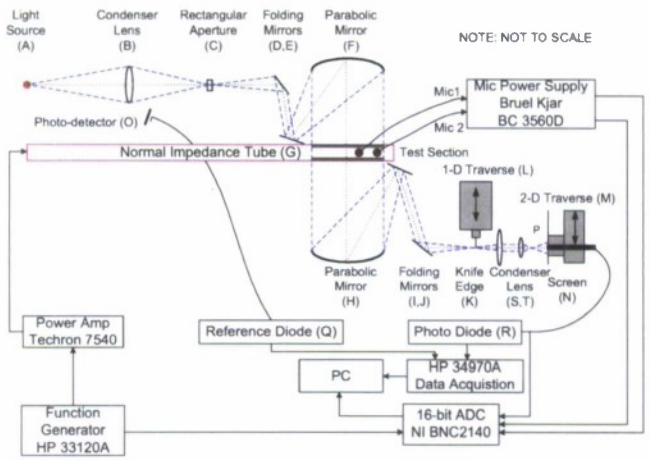

Figure 48: Schematic of optical deflectometer setup.

Two 3.175 mm diameter Brüel and Kjær (Type 4138) microphones are used for simultaneous acoustic pressure measurements to reconstruct the standing plane wave pattern in the test section. These two microphones, referred to as Mic 1 and Mic 2, are placed $d_1 = 63.8$ mm and $d_2 = 44.8$ mm from the specimen, respectively. They are flush mounted in a rotating plug to the

top of the tube, and both microphones are connected to a Brüel and Kjær PULSE Multi-Analyzer System (Type 3560), which served as the power supply for the microphones. The analysis was carried out entirely in the frequency domain and ensemble averaging was performed over 1,000 periodic blocks of data with 512 data points in each block, thereby reducing uncorrelated noise. The sampling frequency of the data acquisition system was set at 51.2 kHz, providing a frequency resolution of 100 Hz. The output signals of the two microphones and the two photodiodes were passed to a 16-bit A/D converter (National Instrument Model NI4522) with built-in anti-aliasing filters. The dc component of the reference photodiode signal used to correct for the temporal variations in the light source intensity was sampled using a HP34970A data acquisition unit. The positioning, data acquisition, and traverse systems were processed and controlled using LabVIEW.

5.2 Two-microphone method

TMM is used to measure the complex reflection coefficient and the normal incident acoustic impedance (Chung & Blaser, 1980 and Seybert & Ross, 1977). This complex reflection coefficient completely specifies the acoustic field for planar modes and is used to calculate the density fluctuation gradient along the tube axis. A frequency response function H_{12} between Mic 1 and Mic 2 is estimated by

$$\hat{H}_{12} = \frac{\hat{G}_{12}}{\hat{G}_{11}} \tag{5.1}$$

where $\hat{G}_{12}$ is the estimated cross spectrum between Mic 1 and Mic 2, and $\hat{G}_{11}$ is the estimated autospectrum of Mic 1 using standard methods described in reference 0.
The complex reflection coefficient is(Seybert & Ross, 1977)

$$R = \frac{\hat{H}_{12} - e^{-jks}}{e^{jks} - \hat{H}_{12}} e^{2jkd_1} \tag{5.2}$$

where $j = \sqrt{-1}$, k is the wave number of the air along the axis of the tube, d_1 is the distance from Mic 1 to the specimen, and $s = d_1 - d_2$ is the distance between Mic 1 and Mic 2. The uncertainty associated with this method is described in Shultz et al (2007).
Since the TMM assumes that the sound field inside the tube is planar, the time-harmonic acoustic field is (Blaekstock, 2000)

$$\begin{aligned} p(d,t) &= P_{in}\left(e^{jkd} + Re^{-jkd}\right)e^{-j\omega t} \\ &= P(d)e^{-j\omega t} \end{aligned} \tag{5.3}$$

where P_{in} is the complex incident wave amplitude. For a linear isentropic process, pressure and density fluctuations are related by

$$P(d) = \rho(d)c_0^2 \tag{5.4}$$

where c_0 is the isentropic sound speed. Therefore, the pressure gradient in the d direction is

$$\frac{\partial P(d)}{\partial d} = c_0^2 \frac{\partial \rho(d)}{\partial d} \tag{5.5}$$

Substituting Equation (5.3) into Equation (5.5) results in

$$\frac{\partial \rho(d)}{\partial d} = P_{in} jk \left(e^{jkd} - Re^{-jkd} \right) / c_0^2 \tag{5.6}$$

The goal of the approach in this paper is to determine the density fluctuation gradient using the non-intrusive optical deflectometer device.

5.3 Quantitative Schlieren method

The static calibration establishes the relationship between the light intensity fluctuation on the image screen and the density gradient fluctuation in the test section. The angular deflection ε_d is related to the density gradient in the d direction via (Settles, 2001)

$$\varepsilon_d \approx \frac{kW}{n_0} \cdot \frac{\partial \rho}{\partial d} \tag{5.7}$$

where $k = 2.259 \times 10^{-4}\ \mathrm{m^3/kg}$ is the Gladstone-Dale constant for air at standard conditions, W is the width of the test section along the optical path, and n_0 is the refractive index of the medium. As shown in Figure 49, assuming that the knife-edge is perpendicular to the direction of the angular deflection, parallel light rays deflected by a small angle ε_d result in a displacement of the light source image by an amount

$$\Delta a = f_2 \varepsilon_d \tag{5.8}$$

where f_2 is the focal length of the second parabolic mirror.

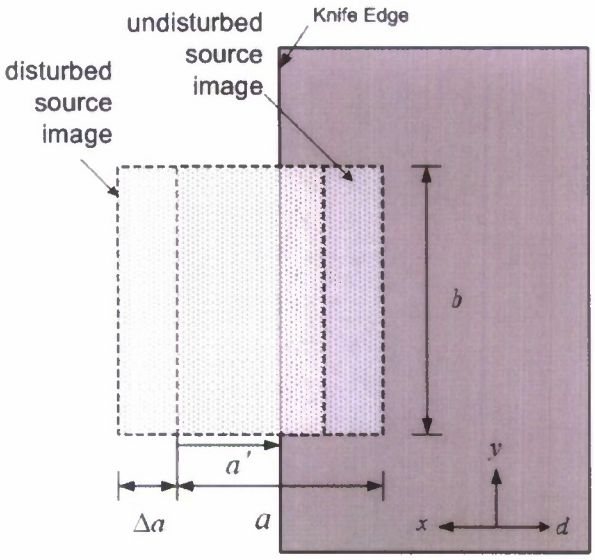

Figure 49: Light source image in the plane of the knife edge (50% cut-off).

Figure 49 shows the illuminated side of the knife-edge, on which a conjugate image of the rectangular source appears. However, the knife-edge cuts off a fraction, typically 50%, of the incident light to achieve the schlieren effect. Assuming that the power of the light beam is conserved after passing through the knife-edge and that diffraction effects can be neglected, then

$$I_{screen} A_{screen} = I_{KE} a' b \tag{5.9}$$

where I_{screen} and I_{KE} are the intensity of the beam at the screen and knife edge, respectively, b is the height of the source image at the knife-edge position, and a' is the dimension of the source that is not cut off by the knife edge. As shown in Figure 49, when parallel light rays are refracted due to a density gradient in the test section, the light source image shifts by an amount Δa. As a result, the change in the intensity on the image screen is

$$\Delta I = \frac{I_{KE} \Delta a b}{A_{screen}} \tag{1}$$

Equations (5.7) – (5.10) are combined to find the optical sensitivity of the schlieren instrument, defined as the change in intensity per unit change in the density gradient

$$S_{optical} = \frac{\Delta I}{\partial \rho / \partial d} = \frac{k f_2 W}{a' n_0} \cdot I_{screen} \tag{5.11}$$

To measure ΔI, a linear avalanche photodiode is mounted on the image screen. This photodetector itself has a sensitivity $S_{pd} = \Delta V / \Delta I$ that converts intensity fluctuations into voltage fluctuations. The total sensitivity of the sensor is the product $S_{total} = S_{optical} S_{pd}$. Clearly, it is desirable to have a large sensitivity, but other considerations, such as sensor noise and

bandwidth, should be considered when designing the instrument. Equation (5.11) shows how to increase $S_{optical}$, namely by increasing f_2. However, the apparent possibility of increasing I_{screen} and increasing the cutoff (by decreasing a') has important implications for the choice of the photodetector. These issues are considered below.

The device is calibrated to obtain the overall sensitivity. The photodetector is placed in the 1.22× magnified screen image at various locations in the d direction, namely at thirty equally spaced positions to cover one acoustic wavelength under study (5 kHz). At each location, the knife-edge was traversed from full to no cutoff to obtain the relationship between the knife-edge position, which is related to the density gradient, and ΔV. Note that a static calibration is only required at one point in the test section for a schlieren system with a perfectly uniform cut-off. However, the calibration was repeated at the 30 locations along the test section to assess cut-off non-uniformity and improve the system accuracy.

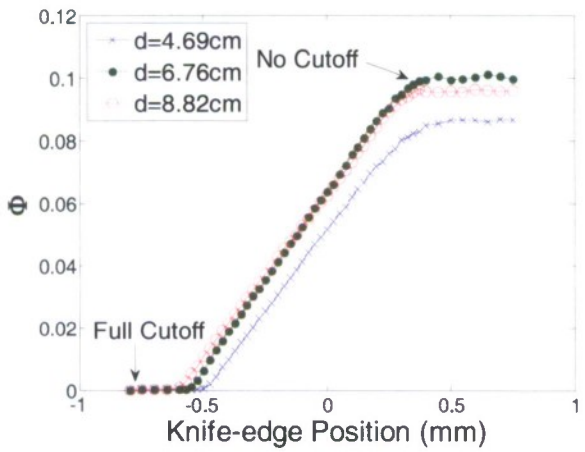

Figure 50: Photodiode knife-edge static calibrations for different locations in test section.

Figure 50 shows three typical static calibration curves for 4th, 15th, and 24th of the 30 locations in the test section. The zero knife-edge position corresponds to a nominal 50% cut-off. The data are presented in normalized form

$$\Phi = \frac{V_{pd} - V_{pd,dark}}{V_{ref} - V_{ref,dark}} \tag{5.12}$$

where V_{pd} is the dc voltage of the photodiode mounted on the image screen, V_{ref} is the dc voltage of the reference photodiode, and $V_{pd,dark}$ and $V_{ref,dark}$ are their respective values when no light is admitted to the sensors. Equation (5.12) thus accounts for any temporal variations in the source and also corrects for any dc offsets in the photodiodes.

As revealed in Figure 50, the normalized output of the photodiode has a linear relationship with the knife-edge position except near full or no cutoff where diffraction effects are important. As predicted by Equation (5.11), operating near full cutoff increases the sensitivity; however, the instrument is nonlinear in this regime. Hence, the device is operated in the linear regime of Figure 50.

The effect of non-uniform cut-off in the image plane leads to variations in the static calibration curves. However, only the slopes, $\Delta\Phi/\Delta a$, of the static calibration curves are required to calculate the density gradient. A calibration curve was found at each of the thirty locations, and the slope in the linear region was calculated for subsequent data reduction. The mean slope of the calibration curve was 0.106 mm^{-1} with a standard deviation of 0.005 mm^{-1}, illustrating a variation in cutoff uniformity of approximately 5%.

Equation (5.12) defines Φ for the undisturbed case. For the disturbed case in the presence of acoustic waves in the tube, the time-harmonic fluctuating density gradient causes a voltage fluctuation V' in the photodiode output, leading to

$$\Delta\Phi = \Phi' - \Phi = \frac{V'}{V_{ref} - V_{ref,dark}} \tag{5.13}$$

Knowledge of the local slope combined with $\Delta\Phi$ gives Δa. Equations (5.7) and (5.8) are then used to calculate the density gradient fluctuation. The magnitude and phase of V' are determined from the coherent power spectrum using the cross spectrum between the photodiode and Mic 1.

The optical deflectometer requires a high-sensitivity, low-noise photodetector. Three common photodetectors include a photomultiplier tube (PMT), a silicon avalanche photodiode (APD), or the pixels of a CCD camera.[0] The selection of the appropriate photodetector depends on the specific application and the required signal-to-noise ratio of the experiment. Therefore, estimating the noise characteristics of the photodetector in the optical configuration is important. In addition, the noise model of the photodetector can be combined with the quantitative schlieren device sensitivity S_{total} to calculate the minimum detectable signal

$$MDS = V_{noise} / S_{total} \tag{5.14}$$

with dimensions of density gradient. Unlike previous versions of the optical deflectometer, where large density gradients are present (perhaps due to shock waves), the appropriate objective here is to measure infinitesimal density gradients corresponding to low-amplitude acoustic waves. From Equation (5.14), this is achieved both by reducing the noise floor of the photodetector and maximizing the device sensitivity.

An APD (Hamamatsu Model C5460-01) photodetector was chosen for this experiment. The APD possesses high bandwidth and high sensitivity. As described in references Virgin et al (2005), an APD becomes the best choice when the background illumination level is high. Conversely, a PMT is the proper choice for low illumination levels. In a schlieren system that uses a high intensity source, an APD is more appropriate. A noise model for this type of photodetector is derived below.

A linear photodetector generates an internal current i_{in} that is proportional to the input light power L_{in}

$$i_{in} = S_p \mu L_{in} \tag{5.15}$$

where S_p is the anode radiant sensitivity, and μ is a voltage-to-current conversion factor. An amplifier then boosts this input current to generate an output current $i_{out} = G \cdot i_{in}$. The input detector current consists of a mean (dc) and a fluctuating (ac) component

$$i_{in} = \bar{i} + i' \tag{5.16}$$

due to background light power and fluctuations of the input light power, respectively.

A noise flow diagram is shown in Figure 51. Two major sources of noise are Johnson (thermal) noise, i_J, and shot noise, i_{shot}. Johnson noise is a constant background noise and it is a function of the Boltzmann's constant, K, experimental ambient temperature, T, the bandwidth of the system, B, and the device resistance, R. This quantity is expressed as an alternating current and is defined as

$$i_J^2 = \frac{4KTB}{R} \tag{5.17}$$

Therefore, Johnson noise is a constant background noise and is independent of the changed input light power.

On the other hand, shot noise is a current directly affected by the incident light power, and is consequently multiplied by the APD by a gain factor G. The total noise added during this multiplication process is from the main noise sources, the background current, and fluctuating current, and the dark current. In addition, a surface leakage current, which is not affected by the internal gain, is also generated by the dark current. As a result, shot noise can be expressed by Virgin et al (2005)

$$i_{shot}^2 = 2E(\bar{i} + i' + i_{dg})BG^2F + 2Ei_{ds}B \tag{5.18}$$

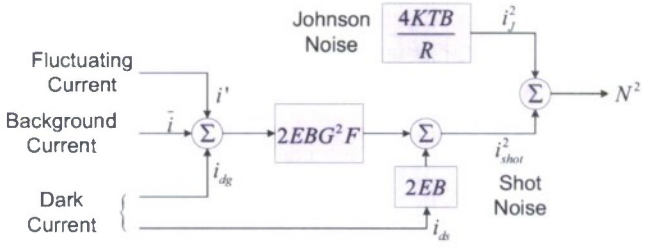

Figure 51: Measured noise sources and the noise flow.

where E is the electron charge constant, F is an excess noise factor, i_{ds} is surface leakage current, which is the dark current not subject to gain, and i_{dg} is an internal current, which is the dark current subject to gain and is described by

$$i_d = i_{ds} + G \cdot i_{dg} \tag{5.19}$$

The internal gain factor, G, is a critical parameter. It is a wavelength dependent value, and the excess noise factor F is a function of this gain factor. It should be noted that all the noise sources generate white noise with bandwidth limited by the sampling frequency or the maximum bandwidth of the detector.

The final measured total noise current, N, is the L^2 norm of Johnson noise and the shot noise,

$$N = \sqrt{i_{shot}{}^2 + i_J{}^2}$$
$$= \sqrt{2E(\bar{i} + i' + i_{dg})BG^2F + 2Ei_{ds}B + \frac{4KTB}{R}} \tag{5.20}$$

The quantitative sensitivity of the photodeteetor, defined by the relationship between the light fluetuation intensity on the image sereen and the voltage fluetuation output from the photodeteetor, is eonsidered. The fluetuating eurrent and voltage after the internal gain ean be expressed by

$$i' = S_p \mu G L' \tag{5.21}$$

and

$$V' = \frac{i'}{\mu} = S_p G L' \tag{5.22}$$

respeetively, where L' is the input light power fluetuation. This quantity ean be related to the sehlieren system by the light intensity ehange on the image sereen as

$$L' = \Delta I \cdot A_{\det ector} \tag{5.23}$$

where $A_{\det ector}$ is the area of the deteetor head exposed to the light. Therefore, the measured voltage fluetuating signal ean be rewritten as

$$V' = S_p G \Delta I \cdot A_{\det ector} \tag{5.24}$$

Thus, the quantitative sensitivity of the photodeteetor, S_q^{ph}, defined as the rate of ehange of measured photodeteetor voltage fluetuating signal with respeet to the input light fluetuation intensity ean be expressed as

$$S_q^{ph} = \frac{V'}{\Delta I} = S_p G A_{\det ector} \tag{5.25}$$

The signal to noise ratio (SNR) for the measurement of the light fluetuation intensity is defined by

$$SNR = \frac{V'}{(N/\mu)} \tag{5.26}$$

In general, the lowest deteetable limit is $(V')_{\min} = (N/\mu)$ at $SNR = 1$. In terms of the power, this situation indieates the measured voltage fluetuating signal has the same power level as the noise. Therefore, we arrive at a noise equivalent power (NEP) expression from Equation (5.22).

$$NEP = (L')_{\min} = \frac{(V')_{\min}}{S_p G}$$
$$= \frac{\sqrt{2E(\bar{i} + i' + i_{dg})BG^2F + 2Ei_{ds}B + \frac{4KTB}{R}}}{\mu S_p G} \tag{5.27}$$

Total quantitative sensitivity for both the schlieren system and the photodetector device, is defined as the ratio between the measured voltage fluctuation from the detector and the density fluctuation gradient

$$S_q^{total} = \frac{V'}{\left(\frac{\partial \rho}{\partial x}\right)}, \tag{5.28}$$

which can be separated into two parts

$$S_q^{total} = S_q^{Sch} \cdot S_q^{ph} = \left[\frac{\Delta I}{\left(\frac{\partial \rho}{\partial x}\right)}\right]\left[\cdot \frac{V'}{\Delta I}\right] \tag{5.29}$$

Substituting Equations (5.11) and (5.25) for S_q^{Sch} and S_q^{ph}, respectively, the full expression of the total quantitative sensitivity of the optical deflectometer is expressed by

$$\begin{aligned} S_q^{total} &= S_q^{Sch} \cdot S_q^{ph} \\ &= \left[\frac{kf_2 W}{an_0} \cdot I_{screen.\max}\right]\left[S_p G A_{detector}\right] \\ &= \frac{kf_2 W}{an_0} \cdot V_{screen.\max} \end{aligned} \tag{5.30}$$

where $V_{screen.\max} = S_p G I_{screen.\max} A_{detector}$ is the maximum voltage the detector can measure during the experiment. Now, the minimum detectable signal (MDS) of the density fluctuation gradient can be calculated from Equation (5.28)

$$(V')_{\min} = S_q^{total} \cdot \left(\frac{\partial \rho}{\partial x}\right)_{\min} \tag{5.31}$$

Similar to the previous NEP operation, the power generated from the MDS of the detector has the same power level of the total noise generated by the detector itself. Thus, the MDS is obtained by substituting Equaiton (5.20) into Equation (5.31)

$$\begin{aligned} MDS &= \left(\frac{\partial \rho}{\partial x}\right)_{\min} \\ &= \frac{\sqrt{2E(\bar{i} + i' + i_{dg})BG^2F + 2Ei_{ds}B + \frac{4KTB}{R}}}{\mu S_q^{total}} \end{aligned} \tag{5.32}$$

The final MDS can be expressed by substituting Equation (5.30) into Equation (5.32)

$$MDS = \frac{(N/\mu)}{S_q^{total}}$$

$$= \frac{\sqrt{2E(\bar{i}+i'+i_{dg})BG^2F + 2Ei_{ds}B + \frac{4KTB}{R}}}{\left[\frac{kf_2W}{an_0}\cdot I_{screen.\max}\right]\left[\mu S_p G A_{detector}\right]} \tag{5.33}$$

$$= \underbrace{\frac{1}{\frac{kf_2W}{an_0}\cdot I_{screen.\max}}}_{Schlieren\ System} \cdot \underbrace{\frac{1}{\left[\mu S_p G A_{detector}\right]}}_{Photodetector} \cdot \underbrace{\sqrt{2E(\bar{i}+i'+i_{dg})BG^2F + 2Ei_{ds}B + \frac{4KTB}{R}}}_{Noise\ Level}$$

Equation (5.33) ean be further simplified by noting that i' is mueh less than i_{dg} and $\bar{i}$, and that $\bar{i}$ is normally mueh larger than i_{dg} and i_{ds}. For the present experiment, the shot noise due to the baekground light level dominates over the Johnson noise, resulting in

$$MDS \approx \frac{an_0\sqrt{2E\bar{i}BG^2F}}{kf_2W\,\mu V_{screen.\max}} \tag{5.34}$$

5.4 Application in Plane Wave Impedance Tube

Two experimental methods are employed simultaneously to investigate the density fluetuation gradient in the tube: the non-intrusive optieal defleetometer and the intrusive TMM to validate. The optieal defleetometer teehnique ean eapture one-dimensional aeoustie fields over a range of aeoustie intensities. Several eases of varied sound pressure level (SPL) are implemented with the range from 94 dB to 128 dB, as shown in Figure 52. The distanee, plotted on the x-axis, and the density fluetuation gradient, plotted on the y-axis, are normalized by the aeoustie wavelength and $P_{in}jk/c_0^2$, respeetively. For eaeh data point shown, a number of voltage readings are taken from the photodeteetor and averaged in the frequeney domain to reduee the random baekground noise of the deteetor. In the high sound pressure level eases (>100 dB), only 1000 bloeks of readings are taken, but as the SPL deereases below 100 dB, 5000 bloeks of data are taken to reduee the random error of the measurement.

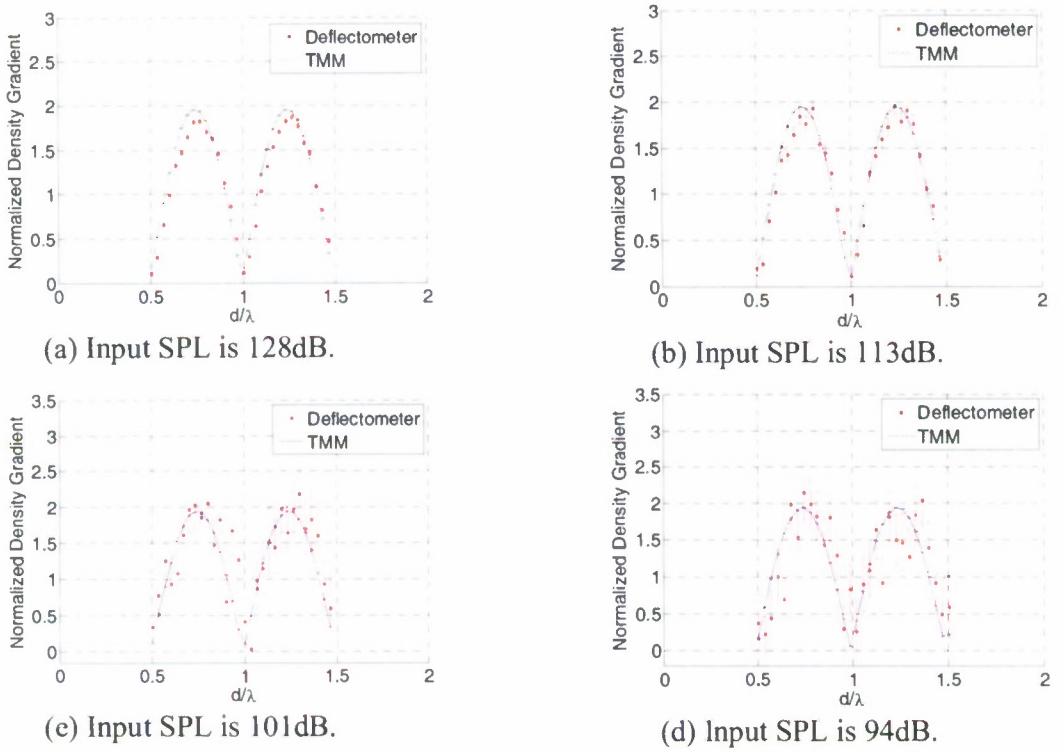

(a) Input SPL is 128dB.

(b) Input SPL is 113dB.

(c) Input SPL is 101dB.

(d) Input SPL is 94dB.

Figure 52: Normalized Density gradient of 1-D pressure wave vs. non-dimensional distance as found using optical deflectometer and TMM.

At 100dB SPL, the density fluctuation gradients from the two methods are very similar. In the case of the lower SPL ($\leq$100 dB), the results obtained with the optical deflectometer show a similar trend with the TMM. The random errors in the density gradient field are large due to the low coherence between the microphone and the photodiode. The error bars are mostly found to fall within each other's range. At 128dB SPL, the two methods achieved their lowest uncertainties. This case is selected as a testbed for density gradient comparison.

The result of the MDS in Equation (5.33) depends on the accuracy of the noise model, N, and the total sensitivity, S_q^{total}. The sensitivity is compared with the optical deflectometer and TMM results as shown in Figure 53. The three curves match well, indicating the total sensitivity model provides a good estimate of the density fluctuation gradient in the test section. The minimum detectable density fluctuation gradient of the APD in the d direction of the tube is estimated and shown in Figure 54 according to Equation (5.33). The maximum light input power is estimated as 6 μW at the fully open knife-edge position. Notice that the quantity $\bar{i}$ in Equation (5.33) is a constant anode current generated due to the input light power. In a lower range of input light power ($<10^{-8}W$), thermal noise dominates. Since the shot noise is directly proportional to the input light power, with increasing light levels, shot noise eventually becomes the dominant noise term.

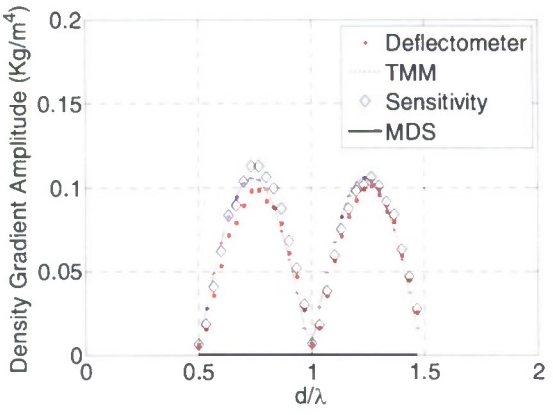

Figure 53: Density gradient calculated from different method for the SPL=128 dB case.

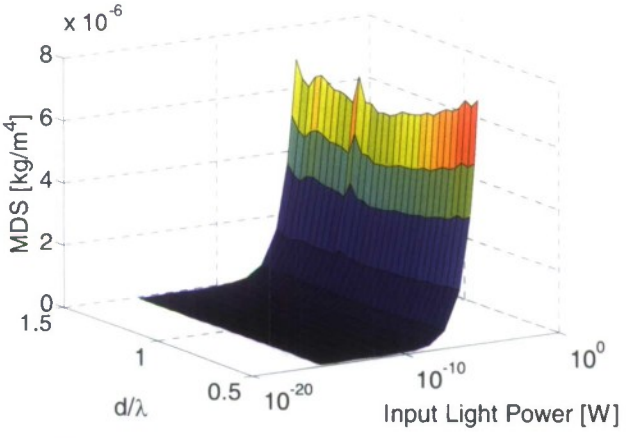

Figure 54: General minimum detectable signal.

The experimental power spectrum of the photodetector for the 128 dB case is shown in Figure 55. Two peaks are clearly seen in the d direction at 5 kHz due to the speaker's single tone excitation signal. Other than the peaks at 5 kHz and dc, the graph shows that the variation of the noise power in the d direction is very low, implying a relatively uniform light intensity along the image screen. It should be noted that the experiment used the half knife-edge cut-off location, but to obtain higher sensitivity, a different cut-off could be used (Settles, 2001)

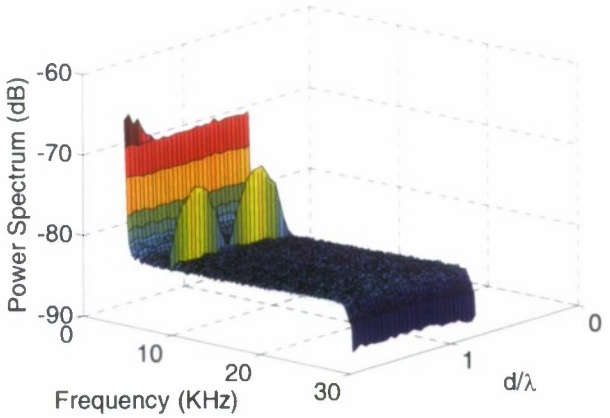

Figure 55: Power spectrum of the photodiode.

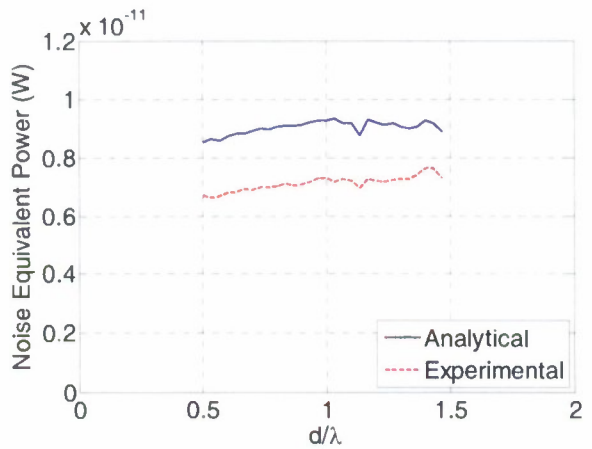

Figure 56: Noise equivalent power.

The analytical and estimated noise equivalent power are shown in Figure 56 The plot shows that the noise model gives a good estimate of the noise floor (within 25%).. The error between the two curves comes from the estimated errors of fluctuating current, i', the dark current subject to a gain, i_{dg}, and surface leakage current, i_{ds}.

The MDS is estimated using the noise model, Equation (5.20), and it is superimposed on the density fluctuation gradient plot (Figure 53). The signal to noise ratio, which is defined by the density fluctuation gradient measured by the TMM and the noise level, is shown in **Error! Reference source not found.**. It is clear that the SNR is very large for this case.

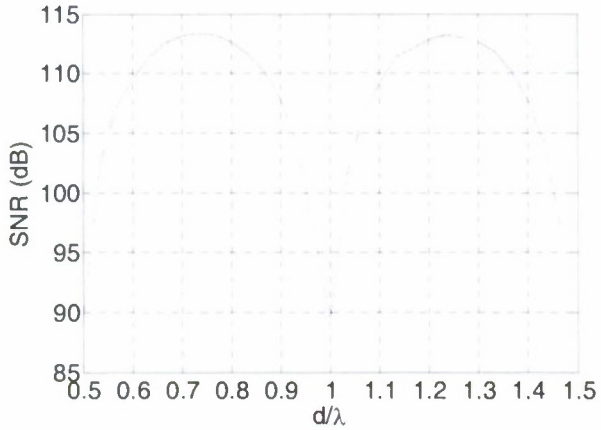

Figure 57: Signal to noise ratio of the TMM and the MDS.

6 Summary and Future Work

In this study we have put together many pieces that can be used for adaptive control of open cavities and understand its effects on the flow physics. These include; the development of a methodology to estimate the time dependent velocity field (mQSE), the application of Poisson's equation to investigate the sources of the fluctuating surface pressure, investigation of the effects of the turbulent flow structure of a successfully controlled flow, the development and application of an adaptive flow control methodology for the for reducing the fluctuating surface pressure and the development of a quantitative Schlieren technique. While at first glance this may seem like a disjoint list it will provide the tools and fundamental understanding so that in a future effort we will be able to successfully control supersonic flow over an open cavity with a detailed understanding of it effects on the flow physics. In what follows we will present a summary of the key findings from each of the aspects of this project.

The mQSE provides a method for estimating the temporal dynamics of a flow field using a low-dimensional model of the flow. For cavity flows, the mQSE allows the large scale dynamics of the flow to be predicted from surface pressure fluctuations in the cavity. This work has demonstrated the application of the mQSE as an analysis tool to study subsonic resonating cavity flow. Application of the mQSE to the velocity showed that the flow at Mach 0.19 and 0.29 was dominated by a circulation region occupying the cavity that oscillates back and forth in time. Any formation of or downstream propagation of vortex structures was intermittent. At Mach 0.39, 0.58 and 0.73, the formation and downstream propagation of vortices was clearly observed and was always accompanied by a negative pressure fluctuation on the cavity floor. The dominance of a particular Rossiter mode was also clear based on the number of vortex structures in the shear layer. The aft-wall pressure loads were shown to be at a minimum when a vortex structure was either passing over or impinging on the aft wall. The pressure would then increase to a maximum as the shear layer was pulled into the cavity by the circulation of the next approaching vortex. Although not presented above, the investigators have also demonstrated that the mQSE can be applied to Schlieren images allowing the temporal dynamics of the density gradients to be examined in relationship to the velocity field with respect to the wall-pressure loads. This lays the ground work for a follow on study where the investigators will use the quantitative Schlieren developed here to investigate both the velocity and density fields synchronously.

The pressure fluctuations on the floor of an L/D = 6.0 rectangular cavity were estimated by integrating Poisson's equation with flow data. The mQSE was utilized to estimate the temporal dependence of the velocity field so that a time-resolved estimate of the pressure loads could be calculated. By decomposing the velocity into mean and fluctuation components, Poisson's equation shows that the pressure depends on sources that are linear (mean-shear) and non-linear (turbulence-turbulence) with respect to the fluctuating velocity. This allowed an estimate of the surface pressure loads related to these two sources to be determined separately and compared in light of the experimentally measured pressure fluctuations. A comparison of the estimated pressure loads with the measured values revealed that the estimation provided a reasonable approximation to the actual pressure loads. It was suggested that the minor

discrepancies that were noticed could be the result of ignoring various acoustic effects like scattering and interference while assuming the flow was completely incompressible (a necessary assumption for Poisson's equation). Using the estimation procedure, the contributions of the mean-shear and non-linear sources were able to be examined separated. The non-linear contribution was found to be broadband in nature without any clear tonal features. However, the mean-shear contribution matched both the frequencies and magnitudes of the spectral peaks associated with the Rossiter modes that were observed in the measured pressure signals. Therefore, only the mean-shear contribution to the pressure loads was found to be associated with the resonant features of the cavity flow. The next step will be reformulate the pressure integration procedure to use a compressible form of Poisson's equation and the estimated velocity and density information from the mQSE procedure.

A novel piezoelectric-driven synthetic jet actuator array is designed for this research. The resulting actuator produces high velocities (above 70 m/s) at the center of the orifice as well as a large bandwidth (from 500 Hz to 1500 Hz) which is sufficient to control the Rossiter modes of interest at low subsonic Mach numbers. This actuator array produces normal zero-net mass-flux jets that seek to penetrate the boundary layer, resulting in streamwise vortical structures. These streamwise vortical disturbances destroy the spanwise coherence of the shear layer, and the corresponding Rossiter modes are disrupted. Alternatively, the introduced disturbances modify the stability characteristics of the mean flow, so that the main resonance peaks may not be amplified. Next, a MIMO system ID IIR-based algorithm is developed based on the structure inferred from the global model. This system ID algorithm combined with a GPC algorithm is applied to a validation vibration beam problem to demonstrate its capabilities. The control achieves ~20 dB reduction at the single resonance peak and ~9 dB reduction of the integrated vibration levels. Finally, this control methodology is extended and applied to subsonic cavity oscillations for on-line adaptive identification and control. Open-loop active control uses a sinusoidal signal with 200 Vpp and an excitation frequency of either 1.05 kHz or 1.5 kHz, which are detuned from the Rossiter frequencies, to drive the actuator array. Multiple Rossiter modes and the broadband level at the surface of the trailing edge floor are reduced. However, when the upstream Mach number increases (greater than Mach number 0.4), the effects of the synthetic jets from this actuator are gradually reduced. Adaptive closed-loop control is then applied for an upstream Mach number of 0.27; the estimated GPC order is 14 and the predictive horizon is 6. To avoid saturation in the control signal, the input weight penalty is chosen as 0.1. The GPC controller can generate a series of control signals to drive the actuator array resulting in dB reduction for the second, third, and fouth Rossiter modes by 2 dB, 4 dB, and 5 dB, respectively. In addition, the broadband background noise is also reduced by this closed-loop controller (i.e., the OASPL reduction is 3 dB). However, unlike previously reported closed-loop cavity results, a spillover phenomenon is not observed in the closed-loop control result. As discussed in Chapter 1, the spillover problem is generated by a linear controller because the disturbance source and control signal or the performance sensor output and the measurement sensor output (feedback signal) are collocated. The nonlinear nature of the adaptive system may be responsible for this effect.

An non-intrusive optical deflectometry technique was shown to be effective for visualizing and measuring the acoustic field in a plane wave tube. The density fluctuation gradient obtained with the optical deflectometer was compared to that obtained with the standard

two-microphone method. The comparison indieated that the instrument can successfully detect density fluctuation gradients above a eertain sound pressure level, sueeessfully eonstructing the aeoustie field for sound pressurc levels ranging from 101dB to 128dB, suggesting the devicc could be applied to study the acoustie field in jet engine naccllc liners. The sensitivities of thc sehlieren setup and the photodeteetor were derived separately. The total quantitative sensitivity was then obtained by combining thc schlieren and photodetector sensitivities. The total sensitivity model was uscd to eompare to the two-mierophone method, and the results show a good match. This sensitivity model ean be used as a eost funetion to optimize optieal systems for various applieations. The noise model, noise equivalent power, and minimum deteetable signal arc defined and derived. The simulation result of the NEP calculated by the analytical noise model is eompared to the experimental measurement. The two methods provided similar results of the photodetector noise floor. Finally, thc noise floor of the deviee was calculatcd, and the signal to noise ratio was estimated using the TMM. With the sensitivity of thc current system the next step will be apply this in a supersonic cavity flow field with thc eventual goal of sampling simultaneously with the surface pressure so that it can bc used in the mQSE to estimatc the timc dependent properties.

7 List of References

Adrian, R., "On the Role of Conditional Averages in Turbulenee Theory," In Proeeedings of the 4th Biennial Symposium on Turbulence in Liquids, 1975.

Akers, J. C., and Bernstein, D. S.,"ARMARKOV Least-Squares Identifieation," Proeeedings of the Ameriean Control Conference, Albuquerque, New Mexico, 1997.

Akers, J. C., and Bernstein, D. S., "Time-Domain Identification Using ARMARKOV/Toeplitz Models," Proceedings of the American Control Conferenee, Albuquerque, New Mexiel, B, 1997.

Al-Ammar, K., Agrawal,A. K., Gollahalli, S. and De Von Griffin, "Application of rainbow Schlieren deflectometry for eoneentration measurements in an axisymmetrie helium jet," Exp. Fluids, Vol. 25 (2), 89 -95, 1998.

Arunajatesan, S., Shipman, J. D., and Sinha, N. "Meehanisms in High Frequeney Control of Cavity Flows," AIAA 2003-0005, 2003.

Arunajatesan, S., Kannepalli, C., and Sinha, N., "Analysis of Control Coneepts for Cavity Flows," 12th AIAA/CEAS Aeroaeoustics Conference, AIAA Paper 2006-2427, 2006.

Arunajatesan, S., Kannepalli, C., Sinha, N., Shumway, G., Ukeiley, L., Shechan, M. and Alvi, F., "Suppression of Cavity Loads Using Leading Edge Blowing Concepts," To Appear AIAA Journal, 2009.

Ashcroft, G. and Zhang, X., "Vortieal structures over rectangular eavities at low speeds," Physics of Fluids, Vol. 17.

Banaszuk, A., Jacobson, C. A., Khibnik, A. I., and Mehta, P. G., "Lincar and Nonlinear Analysis of Controlled Combustion Proccsscs. Part I: Linear Analysis," Proceedings of thc 1999 IEEE International conference on Control Applications, 1999.

Bendat, J. S., and Piersol, A. G., Random Data: Analysis & Measurement Procedures, John Wiley & Sons, Inc., New York, NY, 2000.

Blackstock, D. T., Fundamentals of Physical Acoustics, John Wiley & Sons, Inc, New York, NY, 2000.

Bueno, P. C., Ünalmis, Ö., H., Clemens, N. T., and Dolling, D. S., "The Effeets of Upstream Mass Injection on a Maeh 2 Cavity Flow," AIAA 2002-0663, 2002.

Cabell, R. H., Kegerise, M. A., Cox, D. E., and Gibbs, G. P., "Experimental Feedbaek Control of Flow Induced Cavity Tones," AIAA 2002-2497, 2002.

Caraballo, E., Yuan, X., Little, J., Debiasi, M., Yan, P., Serrani, A., Myatt, J. H., and Samimy, M., "Feedback Control of Cavity Flow Using Experimental Based Reduced Order Model," AIAA-2005-5269, 2005.

Carroll, B. F, Boulos, E., Sytsma, M., Cattafesta, L. N., Hubner, J. P., and Sheplak, M., "Aero-optic Measurement Facility Charaeterization," AIAA-04-0936, 2004.

Cattafesta, L. N., III, Garg, S., Choudhari, M., and Li, F., "Active Control of Flow-Induced Cavity Resonance," AIAA 97-1804, 1997.

Cattafesta, L.N, et.al., "Prediction and Active Control of Flow-Induced Weapons Bay Acoustics," Final Report, High Technology Corporation, 1999.

Cattafesta, L. N. III, Shukla, D., Garg, S., and Ross, J. A., "Development of an Adaptive Weapons-Bay Suppression System," AIAA 99-1901, 1999.

Cattafesta, L., Song, Q., Williams, D., Rowley, C. and Alvi, F., "Active Control of flow-induced cavity oseillations," Progress in Aerospace Sciences, Vol. 44, pp. 479-502, 2008.

Chokani, N., and Kim, 1., "Suppression of Pressure Oscillations in an Open Cavity by Passive Pneumatic Control," AIAA 91-1729, 1991.

Chung, J. Y. and Blaser, D. A.,"Transfer function method of measuring in-duct acoustic properties, 1-Theory, 11-Experiment," J. Acous. Soc. Am. Vol. 68 (3), 907-921, 1980.

Davis, M. R., "Measurements in a subsonic turbulent jet using a quantitative Schlieren technique," J. Fluid Mech, Vol. 46, 631-656, 1971.

Debiasi, M., and Samimy, M., "An Experimental Study of the Cavity Flow for Closed-Loop Flow Control," AIAA-2003-4003, 2003.

Debiasi, M., and Samimy, M., "Logic-Based Active Control of Subsonic Cavity Flow Resonance," AIAA Journal, Vol. 42, No.9, pp. 1901-1909, 2004.

Debiasi, M., Yan, P., Little, J., Ozbay, H., Myatt, J., and Samimy, M., "An Experimental Study of Subsonic Cavity Flow – Physical Understanding and Control," AIAA-2004-2123, 2004.

Debiasi, P. Y., Yuan, X., Caraballo, E., Efe, M. O., Ozbay, H., Samimy, M., DeBonis, J., Camphouse, R. C., Myatt, J. H., Serrani, A., and Malone, J., "Controller Design for Active Closd-Loop Control of Cavity Flows," AIAA-2004-0573, 2004.

DiStefano, J. J., III, Stubberud, A. R., and Williams, 1. J., Feedback and Control Systems, Schaum's Outlines, 2nd ed., McGraw-Hill, 1990.

Dix, R. E., and Bauer, R. C., "Experimental and Predicted Acoustic Amplitudes in a Rectangular Cavity," AIAA Paper 2000-0472, 2000.

Doty, M. and McLaughlin, D. K., "Space-time correlation measurements of high-speed axisymmetric jets using optical deflectometry," Exp. Fluids, Vol. 38, 415-425, 2005.

Efe, M. O., Yan, P., Ozbay, H., and Samimy, M., "Control of Subsonic Cavity Flows by Neural Networks – Analytical Modes and Experimental Validation," AIAA-2005-0294, 2005.

Fabris, D., and Williams, D. R., "Experimental Measurements of Cavity and Shear Layer Response to Unsteady Bleed Forcing," AIAA 99-0606, 1999.

Gallas, Q., Holman, R., Nishida, T., Carroll, B., Sheplak, M., and Cattafesta, L., "Lumped Element Modeling of Piezoelectric-Driven Synthetic Jet Actuators," AIAA Journal, Vol. 41, No. 2, pp. 240-247, 2003.

Garg, S. and Settles, G. S.,"Measurements of a supersonic turbulent boundary layer by focusing Schlieren deflectometry," Exp Fluids, Vol. 25, 254–264, 1998.

Garg S., and Cattafesta III, L. N., "Quantitative Schlieren measurements of coherent structures in a cavity shear layer", Exp. Fluids, Vol. 30 (2), 123-134, 2001.

Gharib, M., "Response of the Cavity Shear Layer Oscillations to External Forcing," AIAA Journal, Vol. 25, No. 1, pp. 43-4, 1987.

Grace, S., Dewar, W. and Wroblewski, D., "Experimental investigation of the flow characteristics within a shallow wall cavity for both laminar and turbulent upstream boundary layers," Experiments in Fluids, Vol. 36, pp. 791–804, 2004.

Heller, H., and Bliss, D., "The Physical Mechanism of Flow-Induced Pressure Fluctuations in Cavities and Concepts for Their Suppression," AIAA Paper 75-491, 1975.

Heller, H., and Delfs, J., "Cavity Pressure Oscillations: The Generating Mechanisms Visualized," *Journal of Sound and Vibration*, Vol. 196, No. 2, 1996, pp. 248–252.

Holmes, P.; Lumley, J. L. and Berkooz, G., Turbulence, Coherent Structures, Dynamical Systems and Symmetry, Cambridge Monographs on Mechanics, Cambridge University Press, Cambridge, UK, 1996.

Hong, J., and Bernstein, D., "Bode Integral Constraints, collocation, and Spillover in Active Noise and Vibration control," IEEE Transactions on Control Systems Technology, vol. 6, No.1, 1998.

Hsu, J. S., and Ahuja, K. K., "Cavity Noise Control using Helmholtz Resonators," AIAA 96-1675, 1996.

Juang, J.N. and Phan, M.Q., "Deadbeat Predictive Controllers," NASA TM 112862, May, 1997.

Juang, J.N. and Phan, M.Q., "Identification and Control of Mechanical Systems," Cambridge University Press, 2001.

Kang, W., Lee, S. and Sung, H. "Self-sustained oscillations of turbulent flows over an open cavity," Experiments in Fluids, Vol. 45 pp. 693–702, 2008.

Kegerise, M.A., Cabell, R.H., and Cattafesta, L., "Real-time feedback control of flow-induced cavity tones — Part 1: Fixed-gain control," Journal of Sound and Vibration, Vol. 307, Issues 3-5, pp. 906-923, 2007a.

Kegerise, M.A., Cabell, R.H., and Cattafesta, L., "Real-time feedback control of flow-induced cavity tones — Part 2: Adaptive control," Journal of Sound and Vibration, Vol. 307, Issues 3-5, pp. 924-940, 2007b.

Kegerise, M.A, Cattafesta.L., and Ha, C., "Adaptive Identification and Control of Flow-Induced Cavity Oscillations," 1st AIAA Flow Control Conference, St. Louis, MO, 2002.

Kegerise, M., Cabell, R. H., and Cattafesta, L. N., "Real-Time Adaptive Control of Flow-Induced Cavity Tones," (Invited) AIAA-2004-0572, *2004.*

Kestens, T., and Nicoud, F., "Active Control of Unsteady Flow over a Rectangular Cavity," AIAA 98-2348, 1998.

Kook, H., Mongeau, L., and Franchek, M. A., "Active control of Pressure Fluctuations Due to Flow over Helmholtz Resonators," Journal of Sound and Vibration, Vol. 255, No. 1, pp. 61-76, 2002.

Kraichnan, R., "Pressure Fluctuations in Turbulent Flow over a Flat Plate," Journal of the Acoustical Society of America, Vol. 28, No. 3, 1956, pp. 378–390.

Krishnamurty, K., "Acoustic Radiation from Two Dimensional Rectangular Cutouts in Aerodynamic Surfaces," NACA Technical Note 3487, Aug. 1955.

Lamp, A. M., and Chokani, N., "Computation of Cavity Flows with Suppression Using Jet Blowing," Journal of Aircraft, Vol. 34, No. 4, pp. 545-551, July-Aug. 1997.

Lumley, J. L., "The Structure of Inhomogeneous Turbulent Flows" Atmospheric Turbulence and Radio Wave Propagation, (eds. Yaglom and Tatarsky), Nauka, Moscow, pp. 166-178, 1967.

McGrath, S. F., and Shaw, L. L., Jr., "Active Control of Shallow Cavity Acoustic Resonance," AIAA 96-1949, June 1996.

McIntyre, S. S., Stanewsky, E. and Settles, G. S., "An optical deflectometer for the quantitative analysis of turbulent structures," in ICIASF '91 Record, 34–42, 1991.

Mendoza, J. M., and Ahuja, K. K., "Cavity Noise Control through Upstream Mass Injection from a Coanda Surface," AIAA 96-1767, May 1996.

Micheau, P., Chatellier, L., Laumonier, J., and Gervais, Y., "Active Control of a Self-Sustained Pressure Fluctuation Due to Flow Over a Cavity," AIAA-2004-2851, 2004.

Mongeau, L., Kook, H., and Franchek, M. A., "Active Control of Flow-Induced Cavity Resonance," AIAA 98-2349, 1998.

Murray, N. and Ukeiley, L., "Modified quadratic stochastic estimation of resonating subsonic cavity flow," Journal of Turbulence, Vol. 8(53), 2007.

Murray, N. and Ukeiley, L., "Estimation of the flow field from surface pressure measurements in an open cavity," AIAA Journal, Vol. 41(5), pp. 969–972, 2003.

Qian, S., and Chen, D. Joint Time-Frequency Analysis – Methods and Applications. Prentie-Hall Inc., ISBN: 0132543842, 1996.

Raman, G., Raghu, S., and Bencic, T. J., "Cavity Resonance Suppression using Miniature Fluidic Oscillators," AIAA 99-1900, May 1999.

Raman, G., and Raghu, S., "Cavity Resonance Suppression Using Miniature Fluidic Oscillators," *AIAA Journal*, Vol. 42, No.12, pp. 2608-2612, 2004.

Rempfer, D., Kloker, M., Stoll, P., Bestek, H. and Wagner, S., "Evolution of coherent structures in flat-plate boundary layers with and without pressure gradient," In ECCOMAS94, pages 478–486, New York, Wiley, 1994.

Rockwell, D., and Knisely, C., "The organized nature of flow impingement on a corner," Journal of Fluid Mechanics, Vol. 93, 1979.

Rockwell, D., and Naudascher, E., "Review: Self-sustaining Oscillations of Flow Past Cavities," Trans. A.S.M.E., J. Fluids Eng., 100:152-165, 1978.

Roshko, A., "Some Measurements of Flow in a Rectangular Cutout, NACA Technical Note 3488, Aug. 1955.

Rossiter, J. E., "Wind-Tunnel Experiments on the Flow over Rectangular Cavities at Subsonic and Transonic Speeds," Aeronautical Research Council Reports and Memoranda, No. 3438, Oct. 1964.

Rowley, C.W., and Williams, D.R., "Control of Forced and Self-Sustained Oscillations in the Flow Past a Cavity," AIAA-2003-0008, 2003.

Rowley, C. W., Williams, D. R., Colonius, T., Murray, R. M., MacMartin, D., and Fabris, D., "Model-Based Control of Cavity Oscillations – Part II: System Identification and Analsis," AIAA 2002-0972, 2002.

Rowley, C. W., Colonius, T., and Murray, R. M., "Model Reduction for Compressible Flows Using POD and Galerkin Projection," Physica D, 2003.

Rowley, C. W., Williams, D. R., Colonius, T., Murray, R. M., and Macmynowski, D. G., "Linear Models for Control of Cavity Flow Oscillations," J. Fluid Mech., Vol. 547, pp. 317-330, 2006.

Rowley, C. and Williams, D., "Dynamics and Control of High-Reynolds-Number Flow over Open Cavities," Annual Review of Fluid Mechanics, Vol. 38, 2006, pp. 251–276.

Samimy, M., Debiasi, M., Caraballo, E., Ozbay, H., Efe, M. O., Yuan, X., DeBonis, J., and Myatt, J. H., "Development of Closed-Loop Control for Cavity Flows," AIAA-2003-4258, 2003.

Samimy, M., Debiasi, M., Caraballo, E., Malone, J., Little, J., Ozbay, H., Efe, M. O., Yan, P., Yuan, X., DeBonis, J., Myatt, J. H., and Camphouse, R. C., "Exploring Strategies for Closed-Loop Cavity Flow Control," AIAA-2004-0576,2004.

Sarno, R. L. and Franke, M. E., "Suppression of Flow-Induced Pressure Oscillations in Cavities," Journal of Aircraft, Vol. 31, No. 1, pp. 90-96, Jan. - Feb. 1994.

Sarohia, V., and Massier, P. F., "Control of Cavity Noise," Journal of Aircraft, Vol. 14, No. 9, pp. 833-837, 1977.

Schultz, T., Sheplak, M. and Cattafesta, L., "Uncertainty analysis of the two-microphone method," J. Sound Vibr., **304**, 91-109, 2007.

Settles, G. S., Schlieren and Shadowgraph Techniques: Visualizing Phenomena in Transparent Media, Springer-Verlag, New York, NY, 2001.

Seybert, A. F. and Ross, D. F., "Experimental determination of acoustic properties using a two-microphone random-excitation technique," J. Acoust. Soc. Am. Vol. 61(5), 1362-1370, 1977.
Shaw, L. L., "Suppression of Aerodynamically Induced Cavity Oscillations," AFFDL-TR-79-3119, 1979.
Shaw, L., "Active Control for Cavity Acoustics," AIAA 98-2347, 1998.
Shaw, L., and Northcraft, S., "Closed Loop Active Control for Cavity Resonance," AIAA 99-1902, 1999.
Sheehan, M. V., "Supersonic Flow and its Control over Highly Three Dimensional Cavities," M.S.. Dissertation, Florida State Univ., Tallahassee, FL, 2007.
Sirovich, L., "Turbulence and the Dynamics of Coherent Structures. Part 1: Coherent Structures," Quarterly of Applied Mathematics, Vol. 45, No. 3, 1987, pp. 561–571.
Stanek, M., Raman, G., Kibens, V., Ross, J., Odedra, J., and Peto, J., "Control of Cavity Resonance through Very High Frequency Forcing," AIAA 2000-1905, 2000.
Stanek, M. J., Raman, G., Ross, J. A., Odedra, J., Peto, J., Alvi, F., and Kibens, V., "High Frequency Acoustic Suppression – The Role of Mass Flow, the Notion of Superposition, and the Role of Inviscid Instability – A New Model (Part II)," AIAA 2002-2404, 2002.
Stanek, M. J., Raman, G., Ross, J. A., Odedra, J., Peto, J., Alvi, F. S., and Kibens, V., "High Frequency Acoustic Suppression – The Mystery of the Rod-in-Crossflow Revealed," AIAA 2003-0007, 2003.
Tracy, M. B., and Plentovich, E. B., "Cavity Unsteady-Pressure Measurements at Subsonic and Transonic Speeds," NASA TP 3669, 1997.
Ukeiley, L., Cordier, L., Delville, J., Glauser, M. and Bonnet, J.P. "Examination of Large Scale Structures in a Turbulent Plane Mixing Layer. Part 2: Dynamical Systems Model," Journal of Fluid Mechanics, Vol. 441, pp. 67-108, 2001.
Ukeiley, L. S., Ponton, M. K., Seiner, J. M., and Jansen, B., "Suppression of Pressure Loads in Resonating Cavities Through Blowing," AIAA 2003-0181, 2003.
Ukeiley, L. S., Ponton, M. K., Seiner, J. M., and Jansen, B., "Suppression of Pressure Loads in Cavity Flows," AIAA Journal, Vol. 42, No.1, pp. 70-79, 2004.
Ukeiley, L. and Murray, N., "Velocity and surface pressure measurements in an open cavity," Experiments in Fluids, Vol. 38, pp.656–671, 2005.
Ukeiley, L. S., Sheehan, M., Coiffet, F., Alvi, F. S., Arunajatesan, S., and Jansen, B., "Control of Pressure Loads in Geometrically Complex Cavities," Journal of Aircraft, Vol. 45, No. 3, pp. 1014–1024, 2008.
Unalmis, O., Clemens, N. and Dolling, D., "Experimental study of shear layer/acoustics coupling in mach 5 cavity flow," AIAA Journal, Vol. 39(2), pp. 242–252, 2001.
Vakili, A. D., and Gauthier, C., 1994, "Control of Cavity Flow by Upstream Mass-Injection," Journal of Aircraft, Vol. 31, No. 1, pp. 169-174, Jan. - Feb. 1994.
Venugopal, R., and Bernstein, D., "Adaptive Disturbance rejection Using ARMARKOV/Toeplitz Models," IEEE Transactions on Control Systems Technology, Vol. 8, No. 2, 2000.
Virgin, C. A., Carroll, B. F., Cattafesta, L. N., Schanze, K. S. and Kose, M. E., "Pressure-sensitive paint for acoustic pressure fluctuations," ASME Int. Mech. Eng. Cong. & Expo., Nov. 5-11, 2005.
Williams, D. R., Fabris, D., and Morrow, J., "Experiments on Controlling Multiple Acoustic Modes in Cavities," AIAA-2000-1903, 2003.

Williams, D., and Morrow, J., "Adaptive Control of Multiple Acoustic Modes in Cavities," AIAA 2001-2769, 2001.

Williams, D., Fabris, D., Iwanski, K., and Morrow, J., "Closed Loop Control in Cavities with Unsteady Bleed Forcing," AIAA 2000-0470, 2000.

Williams, D. R., Rowley, C., Colonius, T., Murray, R., MacMartin, D., Fabris, D., and Albertson, J., "Model-Based Control of Cavity Oscillations – Part 1: Experiments," AIAA 2002-0971, 2002.

Wilson, L. N. and Damkevela, R. J., "Statistical properties of turbulent density fluctuations," J. Fluid Mech. Vol. 43, pp. 291-303, 1970.

Wiltse, J. M., and Glezer, A., "Direct Excitation of Small-Scale Motions in Free Shear Flows, Phys. Fluids, Vol. 10, No. 8, pp. 2026-2036, 1998.

Yuan, X. , Caraballo, E., Yan, P., Özbay, H., Serrani, A., DeBonis, J., Myatt, J. H. and Samimy, M., "Reduced-Order Model-Based Feedback Controller Design for Subsonic Cavity Flows," AIAA 2005-0293, 2005.

Zhaung, N., Alvi, F., Alkilsar, M. and Shih, C., "Aeroacoustic properties of supersonic cavity flows and their control," AIAA Journal, Vol. 44(9), pp. 2118–2128, 2006.